COMPUTATIONAL STUDY OF ENDOCYTOSIS: MODELING THE BIOENERGETICS OF PROTEIN-MEDIATED MEMBRANE DEFORMATION

Neeraj Jagdish Agrawal

A DISSERTATION

in

CHEMICAL AND BIOMOLECULAR ENGINEERING

Presented to the Faculties of the University of Pennsylvania in Partial

Fulfillment of the Requirements for the Degree of Doctor of Philosophy

2009

Ravi Radhakrishnan, Assistant Professor of Bioengineering and Supervisor of Dissertation

---

Raymond J. Gorte, Professor of Chemical and Biomolecular Engineering and Graduate Group Chairperson

Dissertation Committee

Dennis E. Discher, Professor of Chemical and Biomolecular Engineering

Pual A. Janmey, Professor of Physiology

Prashant K. Purohit, Assistant Professor of Mechanical Engineering and Applied Mechanics

Talid R. Sinno, Associate Professor of Chemical and Biomolecular Engineering

Acknowledgements

ABSTRACT

COMPUTATIONAL STUDY OF ENDOCYTOSIS: MODELING THE BIOENERGETICS OF PROTEIN-MEDIATED MEMBRANE DEFORMATION

Neeraj J. Agrawal

Ravi Radhakrishnan

In eukaryotic cells, the internalization of extracellular cargo into the cytoplasm via the endocytosis machinery is an important regulatory process required for a large number of essential cellular functions, including nutrient uptake, cell-cell communication, and modulation of cell-membrane composition. Endocytosis is orchestrated by a variety of proteins implicated in membrane deformation, cargo recognition and vesicle scission. While the involvement and roles of these proteins in membrane deformation, cargo recognition, and vesicle scission have been identified, current conceptual understanding falls short of a mechanistic description of the cooperativity and the bioenergetics of the underlying vesicle nucleation event which we address here using theoretical models based on an elastic continuum representation for the membrane and coarse-grained representations for the proteins. We describe the energetics of deformations of membranes by solving the Helfrich Hamiltonian by two different formalisms: Monge formalism and surface of evolution formalism. The Monge approach is limited to small deformations of the membrane and thermal effects are included while the surface of evolution approach is versatile in describing membrane geometries in both small and large deformation limits but is limited to axis-symmetric profiles of membrane. To explicitly calculate the role of entropy change due to membrane bud formation, we employ thermodynamic integration method in conjugation with thermodynamic cycle. In our model, curvature inducing proteins and protein assembly like epsin and clathrin coat affect the membrane Hamiltonian by changing the preferred mean curvature of the membrane. This integrated multiscale approach results in a unified description of membrane behavior at the mesoscale, under the influence of curvature-inducing proteins at the nanoscale. Using this toolkit of the methods, we demonstrate the role of the endocytic protein assembly in driving membrane vesiculation and further quantify the energetics of the underlying process.

Contents

List of Tables

List of Figures

Chapter 1

Introduction

1.1 Quantitative biology

Several biological processes are governed by a complex interplay of phenomena occurring at multiple length and timescales. While a coherent and complete description of these processes is not always possible by experimental methods, modeling and simulation approaches can provide valuable insights at atomic, mesoscale, and macroscale resolutions. The quantitative description of mesoscopic manifestations of these nanoscale biological processes is inherently a multiscale problem. This dissertation achieves a multiscale description of three such biological processes - endocytosis, binding of nanocarriers to the endothelium and DNA looping. The intricate biology of these processes is very different from each other; however from a viewpoint of a computational scientist, the unifying theme is the calculation of free energies of these processes which dictate their behavior at equilibrium.

The calculation of free energy of complex systems is seldom straightforward. Moreover, for biological systems, macroscopic models do not exist thus compounding the problem. A reduced simplistic model is often sought for these processes to decrease the number of independent parameters. This dissertation develops coarse-grain biophysics based models and thus paves a way to calculate the free-energies of the above-mentioned biological systems.

1.2 Background - Endocytosis

Cellular membranes are made up of a dynamic mixture of lipids, proteins and carbohydrates and represent a unique and critical biological interface that has been the subject of investigations

through diverse approaches over the past few years; however many aspects of membrane organization, dynamics, and functions remain poorly understood. One of such dynamic phenomenon is endocytosis. Endocytosis is defined as the formation of an intracellular vesicle in a cell through membrane invagination. Through this process, the cell engulfs extracellular/membrane-bound components. This process and its reverse (exocytosis) are required for a large number of essential cellular functions, including nutrient uptake, cell-cell communication, and the modulation of membrane composition. The central role of these transport mechanisms is well appreciated in receptor regulation, neurotransmission, and (targeted) drug delivery. There is accumulating evidence that endocytosis is not merely a mundane transport process to assist in cargo trafficking; rather it is important in several regulatory mechanisms. As a prototypical example, consider the epidermal growth factor receptor (EGFR) which is one of the four members of the Erb family RTKs (EGFR, ErbB2, ErbB3 and ErbB4). Together they modulate a variety of cellular signaling pathways leading to cell proliferation, differentiation, migration and altered metabolism in response to external stimuli - EGF, TGF-α and several other related peptide growth factors. Impaired deactivation of RTKs [14] (including the EGFR) through attenuation of endocytosis is linked to hyper-proliferative conditions like cancer [135]. EGFR is a transmembrane glycoprotein, which upon binding of EGF to its extracellular domain, dimerizes. The dimerization of EGFR is followed by trans-autophosphorylation of tyrosine residues in the cytoplasmic domain of EGFR. A multitude of signaling proteins are then recruited. A few of these signaling proteins either actively deform the membrane or act as adaptor proteins in the endocytic interactome [153].

1.2.1 Receptor Mediated Endocytosis

A vast majority of receptor mediated endocytosis share a common theme: a protein machinery is involved in cargo recognition and in inducing membrane curvature. Cargo recognition can be either through a specific state of the receptor (phosphorylated/ubiquitinated) or via non-specific motifs on the receptor. Similarly, membrane curvature can be induced [111] either by scaffolding proteins (e.g. clathrin), helix insertion (e.g. ENTH domain), cytoskeleton remodeling, or by membrane protein oligomerization. Multitude of proteins involved in various combinations of above pathways make the process of endocytosis complex. Depending upon the physiological conditions, one or more of these pathways can be favored. For example, specific pathways of internalization of RTK, specifically of EGFR, are dependent upon the ambient conditions, like EGF concentration [7, 162](low dose = 1.5 ng/ml; high dose = 20 ng/ml, both within the range of physiological EGF levels). At low EGF concentration, EGFR is exclusively internalized by clathrin-dependent endocytosis (CDE) pathway, while at higher physiological EGF concentration, EGFR is internalized via both CDE

and clathrin-independent endocytosis (CIE) pathways (see Fig. 1.1).

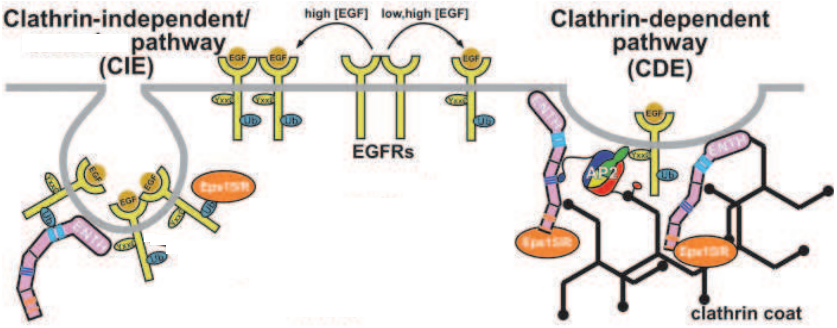

Figure 1.1: Clathrin independent and Clathrin dependent endocytosis of EGFR [7].

Clathrin-Dependent Endocytosis

Endocytosis via clathrin-coated pits is one of most studied internalization pathway. In this pathway, receptor activation through stimulation by extracellular growth factors leads, among other signaling events, to plasma membrane invagination, vesicle formation, and subsequent receptor internalization. This process is tightly orchestrated by several proteins, (see Fig. 1.2). Phosphorylation of specific tyrosine sites on the receptor is followed by the recruitment of clathrin. The next step is the formation of a clathrin coat via nucleation; this is thought to occur when the adaptor AP-2 binds to the phosphorylated receptor [136]. At the site of nucleation, the coat grows through the polymerization of clathrin triskelia or trimers to form a hexagonal lattice [154]. How exactly the endocytotic vesicle budding occurs is unknown. It is hypothesized that a sequence of molecular events in clathrin dependent endocytosis is responsible for the recruitment of adaptor protein 2 (AP-2), various accessory proteins (such as epsin, AP180/CALM, Eps15, Dynamin, Amphiphysin and Endophilin), and clathrin to the plasma membrane. The accessory proteins such as epsin are implicated both in the recognition of cargo to be internalized (through a ubiquitin interacting motif on epsin which potentially binds to a ubiquitinated site on the cargo [7]) and in membrane bending. Upon binding to the head group of PtdIns(4,5)P2 [31] present in the bilayer membrane, the insertion of helix 0 of ENTH domain of epsin into one of the leaflets of the lipid bilayers causes an unequal area expansion of the bilayer, thus inducing a localized intrinsic curvature at the site of the bound epsin [51]. Polymerization of clathrin triskelia into a hexagonal lattice results in a planar structure for the clathrin coat. A clathrin coat interspersed with pentagonal facets is believed to facilitate membrane-bending by forming a curvilinear cage-like scaffold around the membrane [111]. Clathrin per se does not interact with the bilayer. The adaptor proteins such as AP-2 binds to

the clathrin coat and simultaneously interacts with the bilayer, thus gluing the clathrin coat to the bilayer [136]. Additional accessory proteins are required for the release (pinch-off) of the clathrin-coated vesicle from the membrane. In particular, the proteins endophilin and CIN85 orchestrate the vesicle "neck" formation, and dynamin motor proteins are involved in the vesicle pinch-off. After release from the membrane, the vesicle sheds its coat via clathrin disassembly [48].

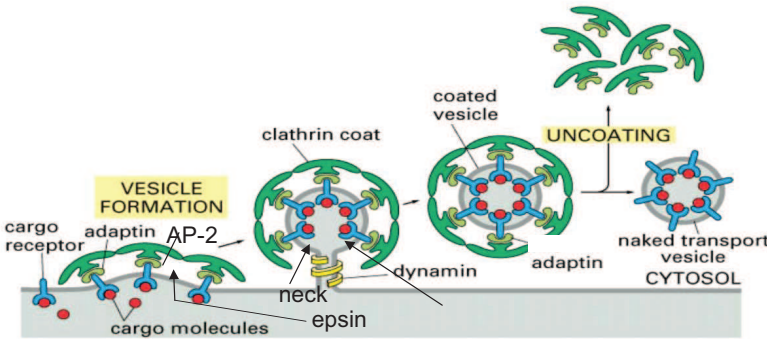

Figure 1.2: Cell-membrane invagination during endocytosis [8].

Clathrin Independent Endocytosis

A variety of possible clathrin independent endocytic pathways have been identified, which vary in the cargoes they transport and in the protein machinery that facilitates the endocytic process [110]. Two types of clathrin independent internalization of EGFR have been proposed [67]: (i) pinocytosis-like endocytosis associated with actin cytoskeleton dynamics and (ii) lipid raft/caveolae dependent endocytosis. Few experimental observations [29,182] showed that EGF treatment causes actin rearrangement leading to dramatic plasma membrane ruffling and formation of micro- and macropinocytic vesicles containing EGF. Endocytosis of EGFR involving cholesterol-rich lipid rafts and/or caveolae has also been demonstrated [162]. Cholesterol-dependent internalization of EGFR occurs under conditions of high EGFR occupancy and EGFR ubiquitination is considered to be important for this pathway. Ubquitination of the receptor serves as a docking site for proteins containing Ubiquitin interaction motifs (UIM) which are conserved features of the epsin and Eps15/R endocytic proteins. How exactly does these proteins lead to membrane vesiculation remains unclear however it can be speculated that high concentration of curvature inducing proteins like epsin can aid in membrane bud formations [143].

1.3 Outline of the thesis

This thesis reports findings on the three biological questions: (i) Modeling the bioenergetics of protein-mediated vesiculation in clathrin-dependent and clathrin-independent endocytosis (ii) Modeling the targeted drug delivery (ii) Modeling the protein-mediated DNA looping.

The contents of this work are divided into 8 chapters. Models for studying membrane deformation at the mesoscale are discussed in chapter 2. This chapter also discusses the two different approaches: Monge formalism and Surface of Evolution formalism, employed to solve the membrane Hamiltonian. In chapter 3, we apply the membrane models in the low-deformation limit using Monge formalism to study the phase behavior of the system when the membrane is curved due to diffusing curvature-inducing proteins (epsin) [6]. This scenario mimics the conditions observed during the initial stages of clathrin-Independent endocytosis. In chapter 4, we study the clathrin-dependent endocytosis using surface of evolution formalism and report the bioenergetics of the clathrin-coated membrane bud formation. Since surface of evolution formalism fails to capture the entropic contributions to the membrane free energy, in chapter 5, we apply the thermodynamic integration technique to quantify the change in membrane entropy as it deforms under the action of curvature-inducing assembly [4]. Equilibrium behavior of a targeted nanocarrier binding to an endothelial cell surface, computed using a coarse-grained model is presented in chapter 6 [3]. In chapter 7, we report our findings on the influence of mediator-protein on the loop formation probability of a DNA [5]. Finally in chapter 8, we summarize the key findings of this work and recommend possible future work to further the knowledge in the field of endocytosis.

Chapter 2

Models for Membrane Deformation

2.1 Introduction

Quantitative description of the thermodynamic and kinetic processes associated with membrane has been an important research component in the physics of amphiphilic systems. Several pioneering theoretical and modeling treatments have focused on different length and time-scales in order to probe the physical-chemical behavior of membrane processes. Atomistic and coarse-grained membrane simulations using classical molecular-dynamics have been applied to the nanoscale behavior of plasma membranes (see Fig. 2.1). These simulations have been successful in delineating the nature of specific interactions between membrane-bound proteins, molecules such as cholesterol and the membrane phase [20, 108, 143], in describing the pathways of micelles formation and vesicle fusion [64, 128], and in characterizing the elastic properties of membrane based on molecular interactions [109, 160]. To address the membrane physics at μm length scales, phenomenological theories based on generalized elasticity [26, 124] have also been used to describe membrane undulations, and curvature modulations [100, 141, 174]. Monte Carlo simulations derived from these phenomenological models have also been successful in describing phase transitions, phase behavior, budding phenomenon associated with multicomponent vesicles [166], and protein mobility on membranes [62, 100, 141].

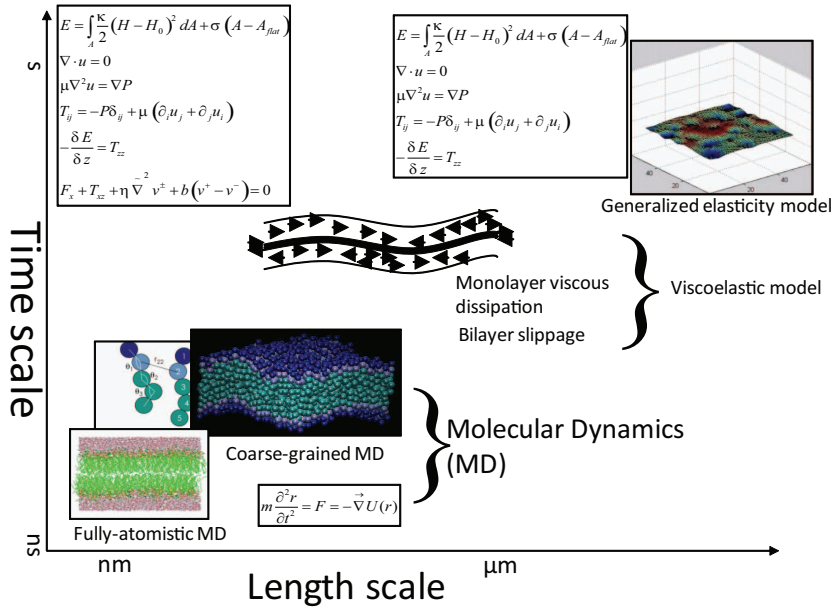

Figure 2.1: Multiscale models of membrane.

2.2 Helfrich Hamiltonian

In this thesis, the membrane is considered from a mesoscopic point of view. This is applicable when the lateral extension and the size of all deformations of interest are much larger than its width. The lipid bilayer can then be modeled as a two-dimensional surface embedded in three-dimensional Euclidean space $\mathbf{R}^3$. Proteins or other entities that can bind to the membrane are represented by solid particles that impose deformations (or curvatures) in the surface. To predict the behavior of the membrane under deformations such as these, one has to know how its energy changes. In a seminal paper, Helfrich [72] described the deformation energy of a thin fluid membrane as a sum of three contributions: the bending energy, the frame energy [174], and the energy contribution as a result of change in Gaussian curvature. The bending energy E_{bend} can be described as follows:

$$E_{bend} = \frac{\kappa A}{2}(C_1 + C_2 - H_0)^2. \tag{2.1}$$

The quantities C_1 and C_2 are the principal curvatures when the membrane is modeled as a surface embedded in 3-dimensional space and H_0 is the spontaneous curvature of the membrane, κ is the bending rigidity, A is the surface area of a piece of the membrane which is denoted as a domain. Using the definition of mean curvature as $H = C_1 + C_2$, the bending energy is rewritten as:

$$E_{bend} = \frac{\kappa A}{2}(H - H_0)^2. \tag{2.2}$$

We now introduce the frame energy which arises as a result of frame tension which suppresses membrane deviations from the flat state. Frame tension arises because it is assumed that the membrane is part of a larger system such as a vesicle or the cytoskeleton of the cell. The work done against the frame tension is the frame energy which is given by the following expression:

$$E_{frame} = \sigma(A - A_{flat}). \tag{2.3}$$

σ is the frame tension and A_{flat} is the projected area of the membrane domain area A onto the flat plane. The last contribution to the energy which is considered is that due to the inducement of Gaussian curvature in the membrane. It is given by:

$$E_{Gauss} = \overline{\kappa} K A, \tag{2.4}$$

where $\overline{\kappa}$ is the splay modulus and K is the Gaussian curvature over the membrane domain with area A.

The Eqns. 2.2, 2.3 and 2.4 comprise the Helfrich Hamiltonian. Considering the complexity of this Hamiltonian, we solve it in two different regimes. In section 2.3, a procedure is outlined to solve the Helfrich Hamiltonian in low deformation limit; also including the effect of thermal noise. In section 2.4, Helfrich Hamiltonian is solved in the extreme deformation limit for an axis-symmetric profile with neglection of thermal noise.

2.3 Monge Formalism

In this formalism, the membrane is modeled as a 2-dimensional surface S embedded in a 3-dimensional Euclidean space equipped with a choice of coordinates R^3. Without loss of generality, for small membrane deformations, one can model S as the graph of the function $z = z(x, y)$. Let R be the projection of the graph of $z = F(x, y)$ onto the $x - y$ plane. Using the idea of Riemann sums, we partition our domain R by subrectangles R_{ij} contained in the interior of R. As we take finer and finer partitions, the subrectangles will cover R with the possible exception of a set of measure zero. We assume that the length and width of the subrectangles are given respectively by Δx and Δy. We further observe that this partition of the region R introduces a partition on the graph in the form of $z(R_{ij})$. We now choose any subrectangle R_{ij} in the domain R. Its area is given as: $A_{flat,\ ij} = \Delta x \Delta y$. We denote the area of its image $z(R_{ij})$ by A_{ij}. We now choose a point $\left(x_i^*, y_j^*\right)$ in R_{ij} and consider the tangent space to $\left(x_i^*, y_j^*, z(x_i^*, y_j^*)\right)$. We approximate the membrane domain A_{ij} by its projection onto the tangent space which we denote by $\hat{A}_{ij}$. The finer the partition of R the better the approximation. From basic functional analysis, the area of the

projection of $z(R_{ij})$ onto the tangent space is:

$$\hat{A}_{ij} = \frac{A_{flat,\ ij}|\nabla z - \vec{k}|}{|(\nabla z - \vec{k}) \cdot \vec{k}|} \tag{2.5}$$

where $\vec{k}$ is the normal to the $x-y$ plane. Simplifying the expression for $\hat{A}_{ij}$, we obtain the following:

$$\hat{A}_{ij} = A_{flat,\ ij}[1 + (\nabla z)^2]^{\frac{1}{2}} \tag{2.6}$$

Hence the various contributions to the membrane Hamiltonian E_{ij} of a membrane patch $z(R_{ij})$ are given below as:

$$E_{bend,\ ij} = \frac{\kappa \Delta x \Delta y}{2}[1 + (\nabla z)^2]^{\frac{1}{2}}[H - H_0]^2 \tag{2.7}$$

$$E_{frame,\ ij} = \sigma \Delta x \Delta y[(1 + (\nabla z)^2)^{\frac{1}{2}} - 1] \tag{2.8}$$

$$E_{Gauss,\ ij} = \overline{\kappa} K[1 + (\nabla z)^2]^{\frac{1}{2}} \Delta x \Delta y \tag{2.9}$$

We now take the Riemann sum to obtain the Hamiltonian E of the membrane domain S:

$$E = \sum_{i,j} (E_{bending,\ ij} + E_{frame,\ ij} + E_{Gauss,\ ij}) \tag{2.10}$$

$$= \sum_{i,j} \Big(\frac{\kappa}{2}[1 + (\nabla z_{ij})^2]^{\frac{1}{2}}[H_{ij} - H_{0,\ ij}]^2 + \sigma[(1 + (\nabla z_{ij})^2)^{\frac{1}{2}} - 1] + \overline{\kappa} K_{ij}[1 + (\nabla z_{ij})^2]^{\frac{1}{2}} \Big) \Delta x \Delta y \tag{2.11}$$

where ∇z_{ij}, H_{ij}, $H_{0,\ ij}$ are evaluated at (x_i^*, y_j^*) in R. Taking finer and finer partitions, the Riemann sum becomes the integral:

$$E = \int\int_R \frac{\kappa}{2}[1 + (\nabla z)^2]^{\frac{1}{2}}[H - H_0]^2 + \sigma[(1 + (\nabla z)^2)^{\frac{1}{2}} - 1] + \overline{\kappa} K[1 + (\nabla z)^2]^{\frac{1}{2}} dxdy \tag{2.12}$$

The mean curvature H of the surface S expressed as the graph of $z = z(x, y)$ is given by:

$$H = \frac{(1 + z_x^2)z_{yy} + (1 + z_y^2)z_{xx} - 2z_x z_y z_{xy}}{(1 + z_x^2 + z_y^2)^{\frac{3}{2}}} \tag{2.13}$$

We linearize the denominator as follows:

$$\frac{1}{(1 + z_x^2 + z_y^2)^{\frac{3}{2}}} = \left(1 - \frac{3}{2}z_x^2 - \frac{3}{2}z_y^2\right) \tag{2.14}$$

We consider only the first and second degree terms in the linearized expression of the mean curvature. This yields,

$$H \approx z_{xx} + z_{yy} = \nabla^2 z \tag{2.15}$$

We repeat the same process with the Gaussian curvature which is expressed as

$$K = \frac{z_{xx} z_{yy} - z_{xy}^2}{(1 + z_x^2 + z_y^2)^2} \tag{2.16}$$

Again considering only the first and second degree terms, the Gaussian curvature K is approximated by

$$K \approx z_{xx}z_{yy} - z_{xy}^2 \tag{2.17}$$

For the area term, the binomial expansion of $[1 + (\nabla z)^2]^{\frac{1}{2}}$ is valid only if $|(\nabla z)|^2 < 1$. The area element is therefore approximated by the quadratic expression:

$$[1 + (\nabla z)^2]^{\frac{1}{2}} dxdy \approx [1 + \frac{1}{2}(\nabla z)^2]dxdy \tag{2.18}$$

Thus the membrane energy E becomes:

$$E = \int\int_R \frac{\kappa}{2}[\nabla^2 z - H_0]^2 + \frac{\kappa}{4}(\nabla z)^2[\nabla^2 z - H_0]^2 + \frac{\sigma}{2}(\nabla z)^2 + \overline{\kappa}(z_{xx}z_{yy} - z_{xy}^2)(1 + \frac{1}{2}(\nabla z)^2)dxdy \tag{2.19}$$

We again ignore all terms of degree greater than second. Then the energy E of the patch of membrane S represented as the graph of the function $z = z(x, y)$ takes the following form [63]:

$$E = \int\int_R \frac{\kappa}{2}[\nabla^2 z - H_0]^2 + \left(\frac{\kappa}{4}H_0^2 + \frac{\sigma}{2}\right)(\nabla z)^2 + \overline{\kappa}(z_{xx}z_{yy} - z_{xy}^2)dxdy. \tag{2.20}$$

2.3.1 Boltzmann sampling of membrane conformations

The equilibrium sampling of membrane conformations according to the Boltzmann distribution is performed using the Time-Dependent Ginzburg Landau (TDGL) simulations [26]. In this protocol, we generate new membrane configurations from existing ones by numerically integrating the equation:

$$\frac{\partial z(r,t)}{\partial t} = -M\frac{\delta E}{\delta z} + \xi(r,t) \tag{2.21}$$

In the above equation, M is a scalar mobility term and t represents a fictitious time (true membrane dynamics can be obtained by replacing M by Oseen tensor, see section 8.2 for details). ξ is the thermal noise term with following two properties [26]:

$$\langle \xi(\mathbf{r}, t) \rangle = 0 \tag{2.22}$$

$$\langle \xi(\mathbf{r}, t)\xi(\mathbf{r}', t') \rangle = k_B T M \delta(t - t')\delta(\mathbf{r} - \mathbf{r}') \tag{2.23}$$

Now we derive an expression for the force acting per unit area on the membrane in the z direction, $F_z = -\frac{\partial E}{\partial z}$. Since the integral E is a functional of z, we calculate the force, F_z using the variational calculus. The functional derivative of E with respect to z denoted by $\frac{\delta E}{\delta z}$ is a distribution such that for all test functions η,

$$\frac{\delta E}{\delta z} = \frac{d}{d\epsilon}E(z + \epsilon\eta)\Big|_{\epsilon=0} \tag{2.24}$$

where ϵ is a scalar. The test functions η and their gradients $\nabla\eta$ and higher order derivatives are assumed to be zero along the boundary curve of the region R. Hence,

$$\frac{\delta E}{\delta z} = \frac{1}{2}\frac{d}{d\epsilon}\int\int_R \kappa\left[\nabla^2(z+\epsilon\eta) - H_0\right]^2 + \left(\frac{\kappa}{2}H_0^2 + \sigma\right)\left(\nabla(z+\epsilon\eta)\right)^2 dxdy\,\Big|_{\epsilon=0} \quad (2.25)$$

$$= \int\int_R \kappa\left(\nabla^2 z - H_0\right)\left(\nabla^2\eta\right) + \left(\frac{\kappa}{2}H_0^2 + \sigma\right)(\nabla z)\cdot(\nabla\eta)dxdy \quad (2.26)$$

where we have neglected the contribution of Gaussian curvature to the membrane Hamiltonian. This assumption is justified for the membrane shape transformations which preserves the membrane topology. For such transformations, the contribution of Gaussian curvature to the Hamiltonian is a constant and hence this constant drops out while taking the variational derivative.

We now reexpress the integrand in a form such the divergence form of the Green's theorem will yield the Euler-Lagrange equation (i.e. the variational derivative). The first term of the integrand yields:

$$\kappa(\nabla^2 z - H_0)(\kappa\nabla^2\eta) = \kappa\nabla\cdot\left(\nabla\eta(\nabla^2 z - H_0) - \eta\nabla(\nabla^2 z - H_0)\right) + \eta\kappa\nabla^2(\nabla^2 z - H_0). \quad (2.27)$$

and the second term of the integrand yields:

$$\left(\frac{\kappa}{2}H_0^2 + \sigma\right)\nabla z\cdot\nabla\eta = \nabla\cdot\left(\left(\frac{\kappa}{2}H_0^2 + \sigma\right)\eta\nabla z\right) - \eta\left(\kappa H_0\nabla z\cdot\nabla H_0 + \left(\frac{\kappa}{2}H_0^2 + \sigma\right)\nabla^2 z\right) \quad (2.28)$$

We now apply the flux-divergence form of the Green's theorem which states that:

$$\oint_C \mathbf{X}\cdot\mathbf{n}\; ds = \int\int_R \nabla\cdot\mathbf{X}\; dxdy \quad (2.29)$$

where $\mathbf{X}$ is a vector field over the region R enclosed by the curve C and $\mathbf{n}$ is the normal to the curve E.

We now apply the Green's theorem to the divergence terms of each of the integrals. Recall that η, $\nabla\eta$ and its higher order derivatives vanish at the boundary of the region R. We obtain the following expression for the functional derivative,

$$\frac{\delta E}{\delta z} = \int\int_R \eta\kappa\nabla^2(\nabla^2 z - H_0) - \eta\left(\kappa H_0\nabla z\cdot\nabla H_0 + \left(\frac{\kappa}{2}H_0^2 + \sigma\right)\nabla^2 z\right)dxdy \quad (2.30)$$

Since η is arbitrary, the functional derivative becomes:

$$\frac{\delta E}{\delta z} = \kappa\nabla^2(\nabla^2 z - H_0 - \left(\kappa H_0\nabla z\cdot\nabla H_0 + \left(\frac{\kappa}{2}H_0^2 + \sigma\right)\nabla^2 z\right) \quad (2.31)$$

The TDGL equation then acquires the form:

$$\frac{\partial z}{\partial t} = M\left(\kappa H_0\nabla z\cdot\nabla H_0 + \left(\frac{\kappa}{2}H_0^2 + \sigma\right)\nabla^2 z - \kappa\nabla^4 z + \kappa\nabla^2 H_0\right) + \xi \quad (2.32)$$

Initial and Boundary Conditions

The initial membrane profile is set to a flat state. To overcome the problem of finite-size effect, periodic boundary conditions are implemented along the x and y direction. Furthermore, the center of the mass of the membrane is kept fixed to avoid the rigid-body motion of the membrane.

2.3.2 Numerical Solution

We solve the Eq. 2.32 numerically using the explicit Euler finite difference scheme. Within the Monge formalism, we construct a uniform mesh, with mesh size h, onto the membrane (i.e. x-y plane). All the derivatives on the right-hand side of Eq. 2.32 are approximated using a second-order centered-difference scheme while the time derivative on the left-hand side is approximated using first-order scheme.

In general, a n-th order derivative of a function $F(x)$ can be expressed as [41]:

$$\frac{h^n}{n!}F^n(x) = \sum_{i=i_{min}}^{i=i_{max}} C_i F(x+ih) + O(h^{n+p}) \tag{2.33}$$

where p is the order of the error term in the approximation and i_{min} and i_{max} are chosen accordingly depending on whether a forward or backward or central difference scheme is desired together with the appropriate corresponding coefficients C_i. To obtain the coefficients C_i, we write the general Taylor series for $F(x+ih)$ as:

$$F(x+ih) = \sum_{k=0}^{\infty} i^k \frac{h^k}{k!} F^k(x) \tag{2.34}$$

Substituting this equation into the Eq. 2.33, we get

$$F^n(x) = \frac{n!}{h^n} \sum_{k=0}^{n+p-1} \left(\sum_{i=i_{min}}^{i=i_{max}} C_i i^k \right) \frac{h^k}{k!} F^k(x) + O(h^{n+p}) \tag{2.35}$$

Eq. 2.35 is satisfied if and only if the following condition holds

$$\sum_{i=i_{min}}^{i=i_{max}} C_i i^k = \begin{cases} 0, & 0 \le k \le n+p-1, k \ne n \\ 1, & k = n \end{cases} \tag{2.36}$$

This results in $n+p$ equations in $i_{max} - i_{min} + 1$ unknowns. Constraining the number of variables C_i to $n+p$, we obtain a system of $n+p$ equations in $n+p$ unknowns. With this general approach, a forward difference approximation for F^n of order $O(h^p)$ is obtained by setting $i_{min} = 0$ and $i_{max} = n+p-1$. A backward difference by setting $i_{min} = -(n+p-1)$ and $i_{max} = 0$ and a central difference by setting $i_{min} = -\left(\frac{n+p-1}{2}\right)$ and $i_{max} = \left(\frac{n+p-1}{2}\right)$. With this generalization, for

a rectangular uniform mesh along i and j, we get

$$\begin{aligned}
z_{x,ij} =& \frac{(z^m_{i+1} - z^m_{i-1})_j}{2h} + O(h^2) \\
z_{y,ij} =& \frac{(z^m_{j+1} - z^m_{j-1})_i}{2h} + O(h^2) \\
z_{xx,ij} =& \frac{(z^m_{i-1} - 2z^m_i + Z^m_{i+1})_j}{h^2} + O(h^2) \\
z_{yy,ij} =& \frac{(z^m_{j-1} - 2z^m_i + z^m_{j+1})_i}{h^2} + O(h^2) \\
z_{xxxx,ij} =& \frac{(z^m_{i-2} - 4z^m_{i-1} + 6z^m_i - 4z^m_{i+1} + z^m_{i+2})_j}{h^4} + O(h^2) \\
z_{yyyy,ij} =& \frac{(z^m_{j-2} - 4z^m_{j-1} + 6z^m_j - 4z^m_{j+1} + z^m_{j+2})_i}{h^2} + O(h^2)
\end{aligned} \tag{2.37}$$

where the superscript m indicates the temporal grid point. The $H_{0,x}, H_{0,y}, H_{0,xx}, H_{0,yy}$ are discretized in the same way. The second order finite difference approximation of z_{xxyy} needs to be handled with some care. To obtain an approximation of z_{xxyy} of order 2, we take a fourth order finite difference approximation of z_{xx} and then apply a yy-derivative second order approximation to the fourth order approximation for z_{xx}. This leads to the following form for the discretized z_{xxyy}:

$$\begin{aligned}
z_{xxyy,ij} = \frac{1}{12h^4} \Big\{ & (-z^m_{i-2} + 16z^m_{i-1} - 30z^m_i + 16z^m_{i+1} - z^m_{i+2})_{j-1} \\
& - 2(-z^m_{i-2} + 16z^m_{i-1} - 30z^m_i + 16z^m_{i+1} - z^m_{i+2})_j \\
& + (-z^m_{i-2} + 16z^m_{i-1} - 30z^m_i + 16z^m_{i+1} - z^m_{i+2})_{j+1} \Big\} + O(h^2)
\end{aligned} \tag{2.38}$$

Hence, we integrate the TDGL equation 2.32 numerically with respect to time as:

$$\begin{aligned}
z_{ij}(t + \Delta t) = & \Big\{ M \left(\kappa H_{0,ij}(t) \nabla_{ij} z(t) \cdot \nabla_{ij} H_0(t) + \left(\frac{\kappa}{2} H_{0,ij}(t)^2 + \sigma \right) \nabla^2_{ij} z(t) - \kappa \nabla^4_{ij} z(t) + \kappa \nabla^2_{ij} H_0(t) \right) \\
& + \xi \Big\} \Delta t + z_{ij}(t)
\end{aligned} \tag{2.39}$$

where ∇_{ij} indicates the gradient evaluated at the grid point i, j. The random noise term, ξ is drawn randomly from a Gaussian distribution with zero mean and variance $k_B T M/(h\Delta t)$ and all the spatial derivatives are computed numerically as described in Eqns. 2.37 and 2.38.

2.3.3 The Mobility Term

For a membrane fluctuating in an infinite surrounding fluid, the membrane dynamics can be written as [100] (also see section 8.2):

$$\frac{\partial z}{\partial t} = - \int_{-\infty}^{\infty} d\mathbf{r}' \left(\Lambda(\mathbf{r} - \mathbf{r}') \frac{\delta E}{\delta z} \right) + \xi(\mathbf{r}, t), \tag{2.40}$$

where $\Lambda(\mathbf{r}-\mathbf{r}') = 1/8\pi\eta|\mathbf{r}-\mathbf{r}'|$ is the diagonal part of the Oseen tensor [38] and η is the viscosity of the surrounding fluid. Using the membrane Hamiltonian (with zero spontaneous curvature)

$$E = \int\int \left[\frac{\kappa}{2}\left(\nabla^2 z\right)^2 + \frac{\sigma}{2}\left(\nabla z\right)^2\right] dxdy \tag{2.41}$$

it can be shown [100] that the normalized membrane height autocorrelation obeys:

$$\frac{\langle z(t)z(0)\rangle}{\langle z^2\rangle} = \frac{\sum_{\mathbf{k}}\left(\kappa k^4 + \sigma k^2\right)^{-1} e^{-t/\tau_{\mathbf{k}}}}{\sum_{\mathbf{k}}\left(\kappa k^4 + \sigma k^2\right)^{-1}} \tag{2.42}$$

where $\mathbf{k} = (m,n)2\pi/L$ is the wave vector and $\tau_{\mathbf{k}}$ is the characteristic decay time of k^{th} mode and is given as:

$$\tau_{\mathbf{k}} = \frac{4\eta k}{\kappa k^4 + \sigma k^2}. \tag{2.43}$$

The values of wave-vector are restricted by $-N/2 < m,n \leq N/2$ where N is the number of grids along one direction. For the membrane dynamics given by

$$\frac{\partial z}{\partial t} = -M\frac{\delta E}{\delta z} + \xi(\mathbf{r},t), \tag{2.44}$$

where M is the scalar mobility term, it can be easily shown that normalized membrane height autocorrelation follows:

$$\frac{\langle z(t)z(0)\rangle}{\langle z^2\rangle} = \frac{\sum_{\mathbf{k}}\left(\kappa k^4 + \sigma k^2\right)^{-1} e^{-t/\Omega_{\mathbf{k}}}}{\sum_{\mathbf{k}}\left(\kappa k^4 + \sigma k^2\right)^{-1}}. \tag{2.45}$$

$\Omega_{\mathbf{k}}$ is the characteristic decay time of k^{th} mode and is given as:

$$\Omega_{\mathbf{k}} = \frac{1}{M\left(\kappa k^4 + \sigma k^2\right)}. \tag{2.46}$$

We fit M such that autocorrelation given by Eq. 2.45 matches with that of Eq. 2.42. In Eq. 2.42, we use $\eta = (0.006 + 0.00095)/2$ kg/m-s as the average viscosity [101] of water (extracellular medium) and the cytoplasm, $\kappa = 50k_BT$ and $\sigma = 0$. For numerical purposes, we discretize 250×250 nm^2 membrane patch with grids of 5×5 nm^2. Using this data, we find that $M = 2.5\times10^{-6}$ m^{2}s/kg gives a good agreement between the membrane height autocorrelation predicted by Eq. 2.45 and Eq. 2.42 as seen in the Fig. 2.2.

2.3.4 Linear Stability Analysis

We integrate the TDGL equation numerically using the explicit Euler scheme. The upper bound on the time integration step, δt is dictated by the problem and the spatial grid size so as to ensure numerical stability of the explicit scheme, i.e. boundedness of the numerical solution. When the spontaneous curvature of the membrane is zero, it follows from Eq. 2.46 that

$$\delta t < \frac{h^4}{M\left(4\pi^4\kappa + 2\pi^2\sigma h^2\right)}. \tag{2.47}$$

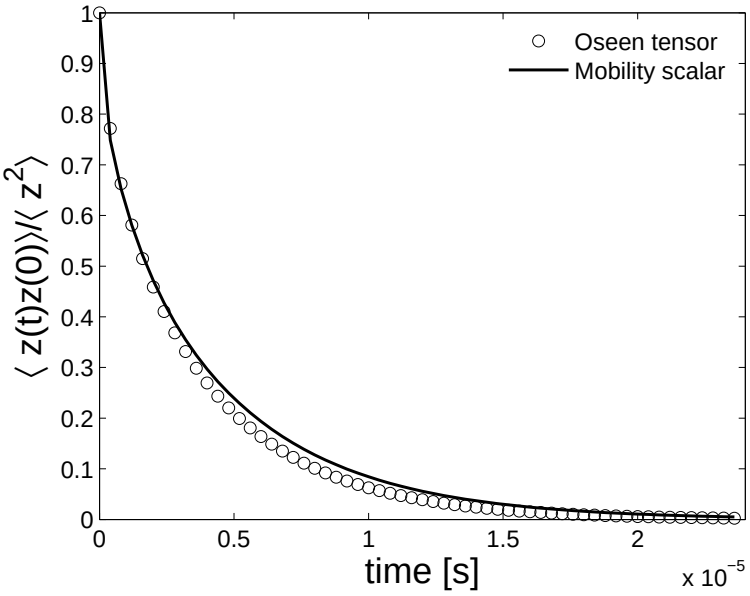

Figure 2.2: A comparison between the membrane height autocorrelation predicted by Eq. 2.45 and Eq. 2.42.

where we have substituted maximum value of wave-vector, k by $\sqrt{2}\pi/h$. Using $\kappa = 50k_BT$, $\sigma = 0$ and $h = 5$ nm, we get $\delta t < 3$ ps.

However, for non-zero value of H_0, we have to recourse to the matrix method [75] to find a δt which leads to bounded solution when membrane is discretized in spatial units of length h. We can write the discretized (using explicit scheme) TDGL (neglecting the thermal noise term) for each spatial grid point of a membrane (pinned at its boundaries) j as:

$$z_j^{n+1} = z_j^n + f(z_{j+i}^n)\delta t + g(H_j)\delta t, \tag{2.48}$$

where, the subscript refers to spatial grid and superscript refers to temporal step. $g(H_j)$ is the non-homogeneous part of TDGL which arises from $\nabla^2 H$. We can write this equation in the matrix form as:

$$\mathbf{z^{n+1}} = \mathbf{Iz^n} + \mathbf{Cz^n} + \mathbf{B}, \tag{2.49}$$

i.e.,

$$\mathbf{z^{n+1}} = \mathbf{Az^n} + \mathbf{B}. \tag{2.50}$$

The matrix $\mathbf{A}$ is dependent on $h, \delta t$, and the specific problem, and is referred to as the *amplification matrix*. The eigenvalues of this matrix $\mathbf{A}$ dictates the numerical stability of the scheme as outlined

in ref. [75]. We note that solution at $(n+1)^{th}$ step is

$$\mathbf{z}^{n+1} = \prod_{j=1}^{n+1} \mathbf{A}^j \mathbf{z}^0 + \sum_{i=1}^{n+1} \left(\prod_{j}^{i-1} \mathbf{A}^j \right) \mathbf{B} \tag{2.51}$$

Now, we can replace $\prod_{j=1}^{n+1} \mathbf{A}^j$ by the eigenvector $\mathbf{v}$ and eigenvalue (diagonal) matrix λ, i.e.,

$$\prod_{j=1}^{n+1} \mathbf{A}^j = \mathbf{v}^T \left(\prod_{j=1}^{n+1} \lambda \right) \mathbf{v}, \tag{2.52}$$

to get,

$$\mathbf{z}^{n+1} = \mathbf{v}^T \left(\prod_{j=1}^{n+1} \lambda^j \right) \mathbf{v}\mathbf{z}^0 + \sum_{i=1}^{n+1} \left(\prod_{j}^{i-1} \lambda^j \right) \mathbf{B}. \tag{2.53}$$

For numerical stability, each of the eigenvalue λ_i of the matrix $\mathbf{A}$ should be within domain $[-1, 1]$ or more specifically they should obey the conditions listed in Table 2.1.

Value of λ_i	Behavior of solution
$0 \leq \lambda_i \leq 1$	No oscillations, steady decay and bounded
$-1 \leq \lambda_i \leq 0$	Oscillations, oscillatory decay and bounded

Table 2.1: Effect of eigenvalues on stability

For all other values of λ_i, the solution diverges. Decreasing the step size h reduces the allowed value of δt. In the Fig. 2.3, we plot the eigenvalues when the integration time step is 1 ps. Since all the eigenvalues are less than one, we conclude that explicit Euler scheme is stable for this choice of time-step.

2.3.5 Code Development

The TDGL code is designed with the philosophy of object-oriented programming (OOP) and is implemented in C++. Further, the code was parallelized using OpenMP (Open Multi-Processing) application programming interface. This implementation of the TDGL code scales almost linearly with the number of processors on a shared memory platform. In Fig. 2.4, we plot the speed-up (defined as the ratio of the wall-time required on n processors to that of one processor) obtained on Steele cluster. This cluster has eight processors per node (i.e. memory is shared per 8 processors). Executing the code on 8 processors requires 1.6×10^{-4} s of real-time (i.e. 1.28×10^{-3} s of computing time) per TDGL step for 50×50 grid-points. The code was validated by comparing the mean energy of the membrane after it has equilibrated to that obtained by equipartition theorem. Equipartition theorem dictates that each degree of freedom appearing in the system Hamiltonian as a quadratic

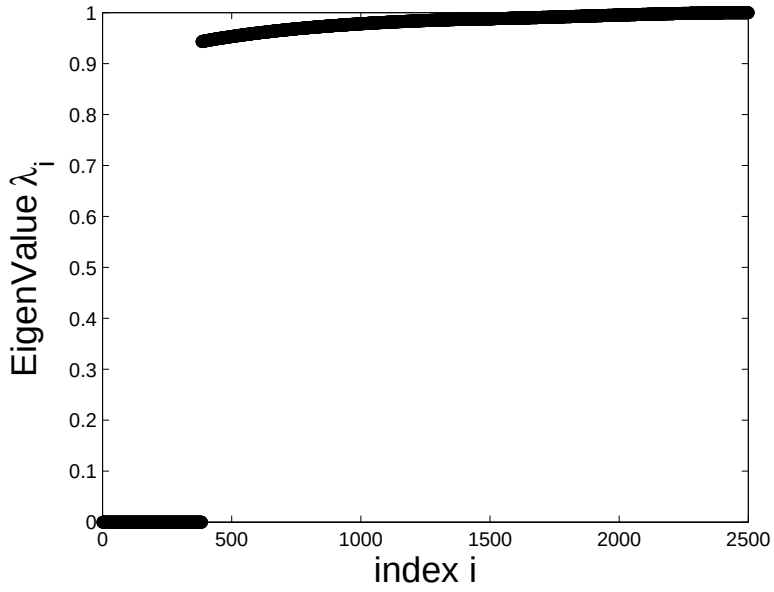

Figure 2.3: Eigenvalues, λ_i of the matrix for a 250×250 nm^2 membrane patch with $\kappa = 50k_BT$ and $\sigma = 0$. We have used $h = 5$nm and $\delta t = 1 \times 10^{-12}$ s.

term, contributes $1/2k_BT$ to the mean energy of the system. When $H_0 = 0$, in the Fourier space, the membrane Hamiltonian reduces to [100]:

$$E = \frac{1}{2L^2} \sum_{\mathbf{k}} (\kappa k^4 + \sigma k^2)|z_{\mathbf{k}}^2| \tag{2.54}$$

Thus each Fourier mode contributes quadratically to the membrane Hamiltonian, thus we expect the mean energy of the discretized membrane to be $((L/h-1)^2-1)k_BT/2$. A good agreement between expected and computed mean energies validates the implementation of the TDGL code.

2.4 Surface of evolution Formalism

Assuming axial symmetry, we introduce a surface of evolution approach to model the membrane at equilibrium. We consider a generating curve γ parameterized by arc length s lying in the $x-z$ plane. The curve γ is expressed as (see Fig. 2.5)

$$\gamma(0, s_1) \rightarrow \mathbf{R}^3\gamma(s) = (R(s), 0, z(s)) \tag{2.55}$$

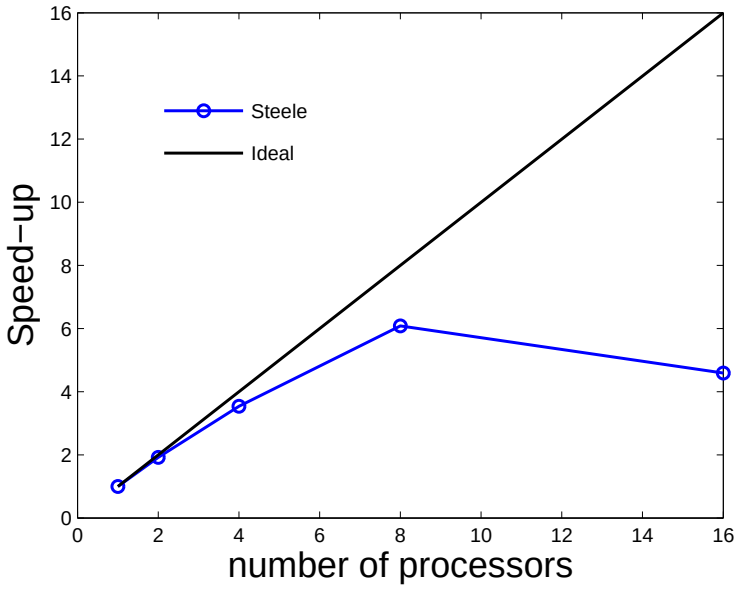

Figure 2.4: Scaling of TDGL code with the number of processors. Total number of grid-points is 2500 and the TDGL code runs for 0.5 μs.

where s_1 is the total arc-length, which is not known a priori. This generating curve leads to a global parametrization of the membrane expressed as

$$X : (0, s_1) \times (0, 2\pi) \rightarrow \mathbf{R}^3 \tag{2.56}$$

$$X(s, u) = (R(s)\cos(u), R(s)\sin(u), z(s)) \tag{2.57}$$

where u is the angle of rotation about z-axis. With this parametrization, the mean curvature H and the Gaussian curvature K are given as follows respectively

$$H = -\frac{z' + R(z'R'' - z''R')}{R} \tag{2.58}$$

$$K = -\frac{R''}{R} \tag{2.59}$$

where the prime indicates differential with respect to arc-length s. The expressions obtained above for the mean curvature and the Gaussian curvature are quite complicated. To simplify them, an extra variable ψ, where $\psi(s)$ is the angle between the tangent to the curve and the horizontal direction, is introduced. The declaration of this extra variable introduces following two geometric constraints:

$$R' = \cos(\psi(s)) \tag{2.60}$$

$$z' = -\sin(\psi(s)) \tag{2.61}$$

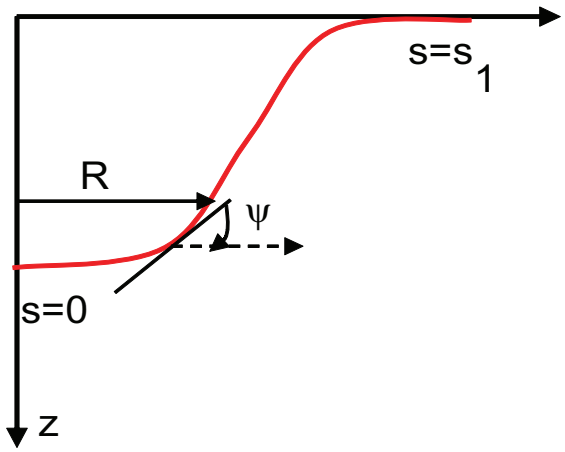

Figure 2.5: A schematic of membrane profile explaining various symbols in surface of evolution formalism.

These two constraints lead to the following simplified expressions for the mean curvature and the Gaussian curvature.

$$H = \psi' + \frac{\sin(\psi(s))}{R(s)} \tag{2.62}$$

$$K = \psi' \frac{\sin(\psi(s))}{R(s)} \tag{2.63}$$

The membrane energy E is then defined by:

$$E = \int_0^{2\pi} \int_0^{s_1} \left(\frac{\kappa}{2} [H - H_o]^2 + \overline{\kappa} K + \sigma \right) dA \tag{2.64}$$

where dA is the area element given by $Rdsdu$, κ is the bending rigidity, $\overline{\kappa}$ is the splay modulus, σ is the frame tension. Substituting for H, K, we obtain the following expression for the free energy:

$$E = \int_0^{2\pi} \int_0^{s_1} \left(\frac{\kappa}{2} \left[\psi' + \frac{\sin(\psi(s))}{R(s)} - H_o \right]^2 + \overline{\kappa} \psi' \frac{\sin(\psi(s))}{R(s)} + \sigma \right) Rdsdu \tag{2.65}$$

We now proceed to determine the minimum-energy shape of the membrane. The condition that specifies the minimum-energy profile is that, the first variation of the energy should be zero. That is:

$$\delta E = 0 \tag{2.66}$$

subject to the geometric constraints $R' = \cos(\psi(s)), z' = -\sin(\psi(s))$. These constraints can be reexpressed in an integral form as follows:

$$\int_0^{s_1} R' - \cos(\psi(s)) ds = 0 \tag{2.67}$$

$$\int_0^{s_1} z' + \sin(\psi(s)) ds = 0 \tag{2.68}$$

Introducing Lagrange multipliers, we solve our constrained optimization problem as follows. We introduce the Lagrange function ν, η and minimize the quantity F:

$$F = \int_0^{2\pi} \int_0^{s_1} \left(\frac{\kappa}{2} \left[\psi' + \frac{\sin(\psi(s))}{R(s)} - H_o \right]^2 + \overline{\kappa}\psi' \frac{\sin(\psi(s))}{R(s)} \sigma \right) R ds du$$
$$+ \nu \int_0^{s_1} R' - \cos(\psi(s)) ds + \eta \int_0^{s_1} z' + \sin(\psi(s)) ds \tag{2.69}$$

Since the integrand of the double integral is independent of u, F simplifies to:

$$F = 2\pi \int_0^{s_1} \left\{ \frac{\kappa R}{2} \left[\psi' + \frac{\sin(\psi(s))}{R(s)} - H_o \right]^2 + \overline{\kappa}\psi' \sin(\psi(s)) + \sigma R + \nu \left[R' - \cos(\psi(s)) \right] \right.$$
$$\left. + \eta \left[z' + \sin(\psi(s)) \right] \right\} ds \tag{2.70}$$

The minimization problem is then expressed as:

$$\delta F = 0. \tag{2.71}$$

We denote the integrand of functional in Eq. 2.70 as L.

$$L = \frac{\kappa R}{2} \left[\psi' + \frac{\sin(\psi(s))}{R(s)} - H_o \right]^2 + \overline{\kappa}\psi' \sin(\psi(s)) + \sigma R + \nu \left[R' - \cos(\psi(s)) \right] + \eta \left[z' + \sin(\psi(s)) \right]. \tag{2.72}$$

So, Eq. 2.70 becomes:

$$F = 2\pi \int_o^{s_1} L ds. \tag{2.73}$$

We interpret F as a functional of the variables $s_1, R, z, \psi, \eta, \nu$. We denote variables R, z, ψ, η, ν by p_i. Now the "generalized" or (non-simultaneous) variation ΔF is expressed as:

$$\Delta F = 2\pi\Delta \int_0^{s_1} L(s, p_i) ds. \tag{2.74}$$

For a detailed description of terminology used and the following method, readers are referred to [173]. Performing the generalized variation, we get

$$\Delta F = \int_0^{s_1} \left(\frac{\partial L}{\partial p_i} - \frac{d}{ds} \frac{\partial L}{\partial p_i'} \right) \delta p_i ds + \left[\frac{\partial L}{\partial p_i'} \Delta p_i \right]_0^{s_1} + \left[\left(L - \frac{\partial L}{\partial p_i'} p_i' \right) \Delta s \right]_0^{s_1} \tag{2.75}$$

At equilibrium, the integral in Eq. 2.75 should be zero, which leads to following Euler-Lagrange equations:

$$\frac{\partial L}{\partial p_i} - \frac{d}{ds} \frac{\partial L}{\partial p_i'} = 0 \tag{2.76}$$

Therefore, the boundary conditions at s_1 are specified by the relationship

$$\left[\frac{\partial L}{\partial p_i'} \Delta p_i \right]_0^{s_1} + \left[\left(L - \frac{\partial L}{\partial p_i'} p_i' \right) \Delta s \right]_0^{s_1} = 0 \tag{2.77}$$

To simplify the boundary conditions, we define a new function H (analogous to Hamiltonian) which is of the form

$$H = -L + p_i' \frac{\partial L}{\partial p_i'} \tag{2.78}$$

Now, the boundary term simplifies to

$$[-H\Delta s]_0^{s_1} + \left[\frac{\partial L}{\partial p_i'}\Delta p_i\right]_0^{s_1} = 0 \tag{2.79}$$

The Eqns. 2.76 and 2.79 result in the following series of equations that describe the membrane equilibrium profile.

$$\begin{aligned}
\frac{\partial L}{\partial \psi} - \frac{d}{ds}\frac{\partial L}{\partial \psi'} &= 0 && (2.80)\\
\frac{\partial L}{\partial R} - \frac{d}{ds}\frac{\partial L}{\partial R'} &= 0 && (2.81)\\
\frac{\partial L}{\partial z} - \frac{d}{ds}\frac{\partial L}{\partial z'} &= 0 && (2.82)\\
\frac{\partial L}{\partial \nu} &= 0 && (2.83)\\
\frac{\partial L}{\partial \eta} &= 0 && (2.84)\\
[-H\Delta s]_0^{s_1} &= 0 && (2.85)\\
\left[\frac{\partial L}{\partial \psi'}\Delta\psi\right]_0^{s_1} &= 0 && (2.86)\\
\left[\frac{\partial L}{\partial R'}\Delta R\right]_0^{s_1} &= 0 && (2.87)\\
\left[\frac{\partial L}{\partial z'}\Delta z\right]_0^{s_1} &= 0 && (2.88)\\
\left[\frac{\partial L}{\partial \nu'}\Delta\nu\right]_0^{s_1} &= 0 && (2.89)\\
\left[\frac{\partial L}{\partial \eta'}\Delta\eta\right]_0^{s_1} &= 0 && (2.90)
\end{aligned}$$

Recall that

$$L = \frac{\kappa R}{2}\left[\psi' + \frac{\sin(\psi(s))}{R(s)} - H_o\right]^2 + \overline{\kappa}\psi'\sin(\psi(s)) + \sigma R + \nu(R' - \cos(\psi(s)) + \eta(z' + \sin(\psi(s)) \tag{2.91}$$

We now take the spontaneous curvature $H_o = \phi(s)$ where $\phi(s)$ is an appropriately chosen function. The Lagrangian L becomes

$$L = \frac{\kappa R}{2}\left[\psi' + \frac{\sin(\psi(s))}{R(s)} - \phi(s)\right]^2 + \overline{\kappa}\psi'\sin(\psi(s)) + \sigma R + \nu(R' - \cos(\psi(s)) + \eta(z' + \sin(\psi(s)) \tag{2.92}$$

The Lagrangian, L depends on the arc-length s due to the (in general) spatially-varying spontaneous curvature, $\phi(s)$. Hence the Hamiltonian, H is not a conserved quantity along s. This is in contrast

to the conserved Hamiltonian in [35] and [157] since those authors assumed a constant spontaneous curvature along the membrane.

Since for a topologically-invariant transformation, the contribution to Gaussian curvature to functional F is constant, we do not expect to see any terms involving $\overline{\kappa}$ in following expressions. The Eq. 2.80 results in the following expression

$$\psi'' = \frac{\cos(\psi)\sin(\psi)}{R^2} - \frac{\psi'\cos(\psi)}{R} + \frac{\nu\sin(\psi)}{R\kappa} + \frac{\eta\cos(\psi)}{R\kappa} + \phi'(s) \tag{2.93}$$

Note that in the above expression, we retain the $\phi'(s)$ term since, in general, spontaneous curvature can be a function of arc-length, s. The Eq. 2.81 gives the following expression for ν'

$$\nu' = \frac{\kappa[\psi' - \phi(s)]^2}{2} - \frac{\kappa\sin^2(\psi)}{2R^2} + \sigma \tag{2.94}$$

The Eq. 2.82 gives the following expression for η

$$\eta' = 0 \tag{2.95}$$

The Eq. 2.83 gives the following expression

$$R' = \cos(\psi(s)) \tag{2.96}$$

The Eq. 2.84 gives the following expression

$$z' = -\sin(\psi(s)) \tag{2.97}$$

Since, s is fixed when $s = 0$, $\Delta s = 0$ when $s = 0$. Hence, Eq. 2.85 reduces to

$$\left[-H\Delta s\right]_{s_1} = 0 \tag{2.98}$$

Since, $\Delta s \neq 0$ when $s = s_1$, we conclude that at $s = s_1$, $H = 0$. Deriving H from L, we get at $s = s_1$:

$$H = \kappa\frac{R}{2}\left[\psi'^2 - \left(\frac{\sin\psi}{R} - \phi\right)^2\right] - \sigma R + \nu\cos\psi - \eta\sin\psi = 0 \tag{2.99}$$

A similar result was obtained by Seifert [157] where they showed that when the total arc-length s_1 is not known a priori (i.e. s_1 is free) the Hamiltonian, $H(s_1) = 0$. From Eq. 2.86, we get

$$\kappa\left[R\left(\psi' + \frac{\sin\psi}{R} - \phi\right)\Delta\psi\right]_0^{s_1} = 0 \tag{2.100}$$

From Eq. 2.87, we get

$$\left[\nu\Delta R\right]_0^{s_1} = 0 \tag{2.101}$$

From Eq. 2.88, we get

$$\left[\eta\Delta z\right]_0^{s_1} = 0 \tag{2.102}$$

There are no terms involving ν' and η' in definition of L in 2.92. Hence, Eq. 2.89 and 2.90 does not provide any information. Since we have second order ODE for ψ, first order ODE for R, z, ν, η and since s_1 is also unknown, in total we need 7 boundary conditions. Equation 2.99 provides us with 1 equation. We still need to provide 6 additional equations. For clarity, s is zero when the curve has zero radius.

We consider two possible boundary conditions:

2.4.1 Closure Equations

Case I

At $s = 0$, let's specify $\psi = 0$, $R = 0$ and $z = 0$. So, at $s = 0$, $\Delta\psi$, ΔR, Δz are all zero. Since, we have not specified ψ, R, z at $s = s_1$, we have $\Delta\psi$, ΔR, Δz are all non-zero at $s = s_1$. Use of Eq. 2.100, 2.101 and 2.102 tells us that at $s = s_1$:

$$R(s_1)\left(\psi'(s_1) + \frac{\sin\psi(s_1)}{R(s_1)} - \phi(s_1)\right) = 0 \tag{2.103}$$

$$\nu(s_1) = 0 \tag{2.104}$$

$$\eta(s_1) = 0 \tag{2.105}$$

If we assume in 2.103 that $R(s_1) \neq 0$, then we have

$$\left(\psi'(s_1) + \frac{\sin\psi(s_1)}{R(s_1)} - \phi(s_1)\right) = 0 \tag{2.106}$$

Substitution of this relation into Eq. 2.99 along with using Eq. 2.104 and 2.105 results into $R(s_1) = 0$ which invalidates our assumption. So, R has to be zero at s_1, i.e. the curve has both its ends at the z-axis. Hence, this boundary condition is not applicable for the pinned membrane.

Case II

At $s = 0$, let's specify $\psi = 0$, $R = 0$ and $z = 0$ and at $s = s_1$, we specify $\psi = 0$, $R = R_0$ and $z = z_0$. With these conditions, Eq. 2.99 reduces to

$$\nu(s_1) = \sigma R_0; \tag{2.107}$$

Hence, we employ this boundary condition to study the invagination in a pinned membrane.

2.4.2 Numerical Algorithm

Analytical Solution for initial guess

When $\sigma = 0$, we expect the solution to be $H = \phi$, $R' = \cos\psi$ and $\nu = 0$. In this section, we show that above three equations are indeed a solution to the Eq. 2.93, 2.94 and 2.96 when $\sigma = 0$.

Assuming $H = \phi$ gives

$$\psi' + \frac{\sin\psi}{R} = \phi \tag{2.108}$$

We differentiate 2.108 w.r.to s and use $R' = \cos\psi$ to get

$$\psi'' = -\frac{\psi'\cos(\psi)}{R} + \frac{\cos\psi\sin\psi}{R^2} + \phi' \tag{2.109}$$

Now, above equation along with $\nu = 0$ satisfies eq. 2.93. Substituting, $\nu = 0$ and $\psi' = -\frac{\sin\psi}{R} + \phi$ in 2.94, we get

$$0 = \frac{\kappa}{2}\left[\left(\frac{\sin\psi}{R}\right)^2 - \left(\frac{\sin\psi}{R}\right)^2\right] \tag{2.110}$$

This proves that when $\sigma = 0$, $H = \phi$, $R' = \cos\psi$ and $\nu = 0$ are the solutions. Note we assume $\nu = 0$ so that it also satisfies the boundary condition, i.e. $\nu(s_1) = 0$. This analytical solution might provides us with a very good initial guess when $\sigma \neq 0$. However, since $H = \phi$ is a first order differential equation, it satisfies only one boundary condition. Hence, in general, solution of $H = \phi$ will not satisfy both boundary conditions for ψ. Hence, in general, $H = \phi$ is not a solution for our system. $H = \phi$ satisfies both boundary conditions iff $\int_0^{s_1} \psi' ds = 0$, i.e. $\int_0^{s_1} \left(\frac{\sin\psi}{R} - \phi\right) ds = 0$.

So, we rather use a different approach to calculate the initial guess: We know that for ψ to satisfy both the boundary conditions, $\int_0^{s_1} \psi' ds$ has to be zero. When $\int_0^{s_1} \phi ds = 0$, we know that $\psi' = \phi$ provides us with a good initial guess consistent with the boundary conditions. When $\int_0^{s_1} \phi ds \neq 0$, we define $\epsilon = \int_0^{s_1} \phi ds$. Then we know that $\int_0^{s_1} (\phi - \epsilon/s_1)\, ds = 0$. Now, we define our initial guess to be $\psi' = \phi - \epsilon/s_1$. Integrating this expression, we get $\psi = \int_0^s \phi ds - \epsilon s/s_1$ as our initial guess.

Numerical Solution

We specify guess value for s_1 and then calculate the guess value for ψ using the method outlined in section 2.4.2. Once initial value of ψ is available, we also calculate initial value of R and ν using Eq. 2.96 and Eq. 2.94 respectively. Then we solve the Eq. 2.93, 2.94, 2.96 and 2.97 along with the boundary conditions specified in section 2.4.1 (case II) and Eq. 2.107 numerically. From the results of these calculations, we calculate $R(s_1)$. Convergence of $R(s_1)$ to R_0 within some tolerance by varying s_1 indicates the converged membrane profile.

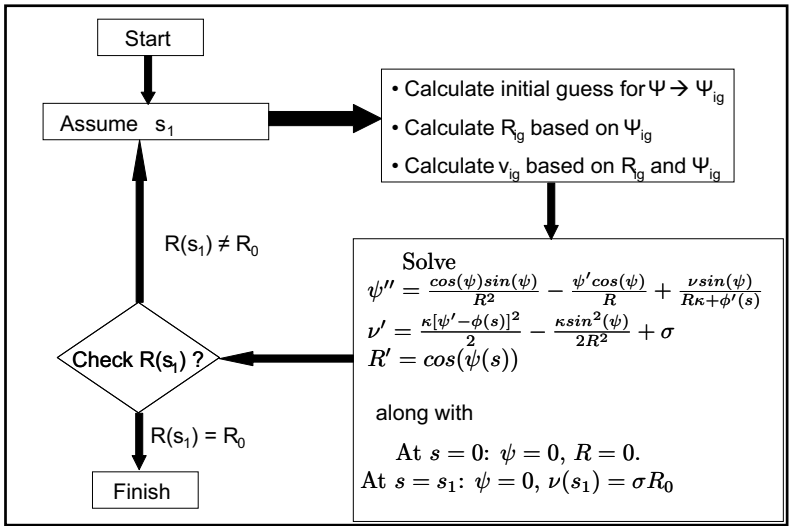

Figure 2.6: Flow chart depicting the solution procedure for surface of evolution formalism.

Chapter 3

Landscape of Finite-Temperature Equilibrium Behavior of Curvature Inducing Proteins on a Bilayer Membrane

3.1 Introduction

Understanding and quantifying the coupling between external signals and intracellular signal transduction is crucial in many biological applications such as receptor trafficking, internalization of targeted pharmacological nanocarriers, cell-cell communication, etc. There is growing appreciation that such processes are regulated and transduced by the interaction of proteins and membranes [164].

In the modeling of lipid-bilayer membranes, previous studies have followed either a particle-based simulation approach [143] or a field theoretic approach [124,148,174]. In the latter approach, the energetics of deformations in planar membranes as well as membranes with intrinsic curvature has been extensively described in previous works by using the Helfrich Hamiltonian. Based on the Helfrich description and through theoretical formalisms and simulation algorithms, the dynamics of elastic membrane sheet in the overdamped limit including hydrodynamic coupling to surrounding solvent and arbitrary external forces have been introduced in previous studies [24, 61, 94, 134, 161]. The infinitely thin elastic sheet assumption has also been relaxed and the inter-layer friction and

slippage between the lipid monolayers have been incorporated [34, 158, 161]. Mechanistic models for cell membrane deformation and vesicle budding in the cellular context based on the elastic free energy formulations have also been proposed [56, 103].

On the experimental front, direct measurements of bending-mediated force transduction and molecular organization in lipid membranes based on interferometry and fluorescence measurements have been reviewed [65]. Different modes by which proteins modulate the curvature of membranes have also been discussed by McMahon et al. [111]: membrane-curvature can be modulated by changes in lipid composition, the oligomerization of curvature scaffolding proteins and the reversible insertion of protein regions that act like wedges or amphipathic sub-domains in membranes. The molecular dynamics and mosaic organization of the plasma membrane and their implications in cellular physiology primarily focused on studies involving fluorescent labeling and imaging have recently been reviewed [105]. These timely reviews of the experimental progress have motivated the development of models for protein diffusion in ruffled surfaces [62] and the simultaneous diffusion of protein and membrane dynamics [13, 37, 121, 141]. In such models, there is one-way coupling between the membrane dynamics, i.e., the protein dynamics as the membrane topology impacts the diffusion of the proteins.

Recently, we extended these simultaneous protein diffusion and membrane motion models to treat the case of curvature inducing proteins diffusing on the membrane [179]. The new aspect introduced in our continuum membrane model is the two-way coupling between the protein and membrane motion. In this case, the membrane topology not only influences the protein diffusion by presenting a curvilinear manifold, but also presents an energy landscape for protein diffusion. The protein diffusion in-turn impacts membrane dynamics because the spatial location of the proteins determine the intrinsic curvature functions and hence the elastic energy of the membrane [179]. In this article, we apply this methodology and explore the equilibrium behavior of bilayer membranes under the influence of cooperative effects induced by the diffusion of curvature inducing proteins.

3.2 Methods

3.2.1 Model for Sampling Membrane Deformations in the Canonical Ensemble

We describe the relaxation of the membrane via a time-dependent Ginzburg-Landau (TDGL) model [26, 125]. The membrane is represented in the Monge gauge, i.e. as a function $z = z(x, y, t)$, where z is the height of the deformed membrane patch. The linearized Helfrich Hamiltonian E (in Monge or Cartesian gauge), obtained by linearizing the expression for mean curvature, associated with

membrane elasticity [125] is given by [174],

$$E = \int\int \left[\left(\frac{\sigma}{2} + \frac{\kappa}{4} H_0^2 \right) (\nabla z)^2 + \frac{\kappa}{2} \left(\nabla^2 z - H_0 \right)^2 \right] dxdy \tag{3.1}$$

The membrane Hamiltonian depends on the frame tension σ, the bending rigidity, κ, and the inhomogeneous intrinsic curvature field $H_0(x, y)$. The values of κ, σ for a cytoskeleton fortified phospholipid bilayer cell membrane are obtained from prior studies [96]: $\sigma = 3\mu\text{N/m}$, $\kappa = 400 k_B T$. The value of intrinsic curvature H_0 is taken to be zero unless curvature-inducing proteins are membrane-bound, see below. The fictitious dynamics of the membrane is described in terms of a scalar mobility factor M, thermal noise ξ, and the linearized membrane Hamiltonian E functional associated with membrane elasticity in Eq. 3.1, given by the time-dependent Ginzburg-Landau (TDGL) model [26],

$$\frac{\partial z}{\partial t} = -M \frac{\delta E}{\delta z} + \xi \tag{3.2}$$

Eq. 3.2 described in-terms of the scalar mobility factor ($M = 10^{-5} \mu m^4 s^{-1} (k_B T)^{-1}$ [138] in our simulations) represents fictitious dynamics because it ignores the important contribution from the hydrodynamic interaction with the surrounding fluid as well as the viscous dissipation within the membrane. However, for the linearized elastic energy functional E, and by making the choice that the noise term in Eq. 3.2 is generated by drawing a random number from a Gaussian distribution with zero mean and with variance depending on the temperature T and mobility factor, i.e., $\langle \xi \rangle = 0$, $\langle \xi(0) \xi(t) \rangle = 2 k_B T M \delta(t)$, the membrane configurations generated by Eq. 3.2 are consistent with the canonical ensemble with probability $\propto \exp(-E/k_B T)$. Moreover, we have ensured that changing the value of M by one order of magnitude does not change the equilibrium properties (such as radial distribution functions) we calculate. We stress that in the present study, we are only interested in the equilibrium sampling of the deformations in the linearized elastic free energy model; however, in the future, an extension to describe the model dynamics of the membrane by including the hydrodynamic interactions can be made by closely following the formalisms briefly discussed in the introduction [94, 148, 158].

We note that while reducing the variational problem to a partial-differential form, we assumed that $|\nabla z|^2 < 1$, which states that the solution of linearized TDGL (in Monge gauge) is valid only when difference in height of adjacent grid-points on the membrane is less than spatial grid size. Moreover the Monge gauge (i.e. representing z as a function x, y) does not support multi-valued topologies of z that are necessary to describe large membrane deformations such as membrane overhangs. Thus the model we are exploring is inherently limited in only being able to describe early nucleation events such as the formation of a vesicle-bud rather than tracking the evolution of the entire vesicle. Still, we consider it worthwhile to implement this linearized membrane elastic

model and combine it with diffusing curvature-inducing functions (see sections 3.2.2 and 3.2.3), with the outlook that it will enable us to widely explore tunable parameter space and to classify emergent membrane response in this approximate but tractable bench-mark model.

3.2.2 Model for Protein-Protein Interaction and Protein-Membrane Interaction

Protein molecules are approximated as structure-less hard spheres and nonspecific protein-protein interactions are considered only as size exclusions, (i.e., repulsive interactions on the scale of the size of the solvated protein). The three-dimensional space is discretized into a lattice using a rectilinear grid with grid-size corresponding to the size exclusion parameter, a_0=20 nm. Consistent with the evidence in the literature [27] specific interactions between the proteins (i.e., protein-protein binding) are not considered and the parameter for size exclusion is obtained from crystallographic data [51]. The lattice points are categorized as either belonging to the extracellular domain, intracellular domain, or the membrane. This division is time-dependent because the membrane can undulate, deform, and stretch as a function of time, in response to thermal fluctuations and protein-mediated interactions. The density of proteins bound to the membrane is given by the dimensionless number $\rho^* = N^{bound} a_0^2/A$. Here, A is the total projected area of the membrane, a_0 is the lattice spacing, ρ^* is the reduced surface density, N_i^{bound} is the number of membrane-bound proteins.

Proteins such as epsin and Ap180 interact with the membrane by inducing curvature in the membrane [51]. To capture this protein-mediated membrane deformation, in the vicinity of a membrane-bound protein, the membrane is assumed to have an intrinsic curvature $H_0(x, y)$. The form of this localized function is assumed to be Gaussian, with a range R and a magnitude C_0; i.e., for a protein located at (x_0, y_0) on membrane, $H_0(x, y) = C_0 \exp[-2\left((x - x_0)^2 + (y - y_0)^2\right)/R^2]$. A multitude of R and C_0 values are explored in our simulations. R is the range of the curvature induction (reported in units of nm or in scaled form $R^* = R/a_0$, where a_0 is the lattice length). C_0 is the maximum curvature (1/radius) reported in units of $1/\mu$m.

On first glance, the hardsphere nature of protein-protein interactions considered in our model appears too simplistic. However, there are several factors unique to the protein-membrane system, which justify the use of such a simplistic assumption. The equilibrium behavior of the system is dominated by the membrane-mediated protein-protein interaction dictated by R rather than by direct protein-protein interactions (which is constituted by van der Waals, electrostatic, hydrogen-bond terms) dictated by a_0. To support these claims, Fig. 3.1 shows that the membrane-mediated interaction is dominated by repulsion at range R, while Fig. 3.3 shows that owing to this repulsion,

the distance of closest approach between two protein molecules on the membrane is R and not a_0. Thus, the nature of the short-range potential is not expected to dictate the thermodynamic behavior, as long as there is no over-whelming short-range attraction through specific interactions between two proteins. The fact that curvature-inducing proteins such as epsins have no specific-interactions with each other, (i.e., no overwhelming attraction at short-range), is established by prior experiment, which establishes these proteins to act as monomers [51]. Together, these justify the use of hard-sphere potential, as they imply that the system behavior at the mesoscale is impervious to the nature of direct short-range protein-protein interactions at the nanoscale.

3.2.3 Model for Protein Diffusion

Our model for sampling different protein conformations is via the simulation of probabilistic hopping between discrete lattice sites. The hopping steps are generated via a kinetic Monte Carlo (KMC) scheme [60] on the discretized lattice in which each hop of each protein (or diffusion) to a neighboring lattice-site is treated as an elementary chemical reaction with an associate rate given by [176] (see Appendix 3.5.1):

$$\text{rate}, a_\mu = \frac{4D}{a_0^2\left(1+(\nabla z)^2\right)} \exp\left(-\frac{\Delta E}{k_B T}\right) \tag{3.3}$$

Here $4D/a_0^2$ is the bare hopping rate (due to free diffusion in a planar manifold in 2-dimensions), the term $1+(\nabla z)^2$ corrects for the curvilinear manifold due to membrane deformation to the first order approximation, and the exponential factor accounts for the protein diffusion in an energy landscape. The energy term in the exponent represents the work done as the protein drags the intrinsic curvature field to the neighboring lattice location for the fixed membrane configuration, where the term ΔE (for protein hop along x-direction) is given by:

$$\Delta E = \frac{\partial E}{\partial x_{0i}}\Delta x_{0i} = \frac{4\kappa C_0 \Delta x_{0i}}{R^2}\int\int_A e^{\left(2\frac{(x-x_{0i})^2+(y-y_{0i})^2}{R_i^2}\right)}\left[H_0\left(1+\frac{(\nabla z)^2}{2}\right)-\nabla^2 z\right](x-x_{0i})\,d^2r \tag{3.4}$$

$$H_0(x,y) = \sum_i C_0 \exp[-2\left((x-x_{0i})^2+(y-y_{0i})^2\right)/R^2] \tag{3.5}$$

The term ΔE in Eq. 3.4 prescribes the energy landscape for the diffusion of curvature-inducing proteins in the linearized elastic model and summarizes the two-way coupling present in this model, which is not present in the related continuum elastic membrane models in the literature. Through the ΔE and the $1+(\nabla z)^2$ terms, the membrane deformation influences protein diffusion. Through the H_0 function (which depends on the positions of all membrane-bound curvature-inducing proteins i, namely x_{0i}, y_{0i}), the proteins influence membrane relaxation in Eq. 3.2. Together, these effects summarize the two-way coupling between protein motion and membrane motion on the equilibrium behavior.

The bulk and lateral membrane-bound diffusion coefficients (D) for translation are taken from experimental data [78, 96] (bulk diffusion coefficient D=10 μm^2/s, membrane-bound bare diffusion coefficient D=1 μm^2/s). The initial distribution of proteins on the membrane surface is random consistent with size exclusion. We carry-out KMC simulations for N$\approx \Delta t/(a_0^2/D)$ steps (such that the total time elapsed in the KMC simulations is equal to t, the time-step of TDGL integration using implicit scheme, we choose $t = 10^{-3}$ s) and we determine the steady state profiles $\langle H_0 \rangle_N$ (by time-averaging over the course of the N steps of the KMC simulations) at every time-step of integration involving the membrane dynamics (TDGL) equations. Thus, the TDGL equations are propagated in time, based on time-averaged interactions dictated by $\langle H_0 \rangle_N$ resulting from the KMC simulations. The temperature T in the TDGL and KMC schemes are made equal to ensure thermal equilibrium. Details of the complete model, numerical simulation, implementation, and stability analysis associated with our KMC-TDGL simulations are available in a recent publication [179]. The simulation results in the propagation of protein as well as membrane degrees of freedom in the canonical ensemble.

3.2.4 Spatial and Temporal Correlation Functions

To capture and quantify the emergent response of the membrane dynamics under the influence of the proteins, we compute several correlation functions.

1. Radial distribution function (see Fig. 3.3, top row): the spatial organization of the proteins bound to the membrane is recorded by calculating the radial distribution function $g(r) = \rho^*(r)/\langle \rho^* \rangle$, where the quantity in the numerator is the surface density of membrane-bound proteins at a particular location and that in the denominator is its spatial average.

2. Orientational correlation function [139] (see Fig. 3.3, middle row) is defined as $\langle \psi_6^*(0)\psi_6^*(r) \rangle$, where $\psi_6^*(r)$ is given by $\sum_j \exp(i6\theta_j(r))$. Here $i = \sqrt{-1}$, the index j runs from 1 to the number of nearest neighbors to any given membrane-bound protein at location r, and $\theta_j(r)$ is the angle formed by the projection of the line joining the nearest neighbors (termed as nearest neighbor bond) on the xy plane with the x-axis. Nearest neighbor pairs are identified as those pairs of molecules separated by a distance that falls in the range of the first peak of the $g(r)$ function. The quantity $\langle \psi_6^*(0)\psi_6^*(r) \rangle$, therefore, measures the persistence of bond-orientational correlations (or hexagonal ordering) among the membrane-bound proteins.

3. Dynamical correlation functions (see Fig. 3.3, bottom row) yield membrane relaxation times and reflect the dynamical state of the system. Membrane height autocorrelation function (see Fig. 3.3, bottom row) is defined as $\langle \sigma_z(0)\sigma_z(t) \rangle$, where $\sigma_z(t)$, see Fig. 3.2, is the

standard deviation of the height profile $z(x, y)$ of the membrane at each spatial location. In our definition, the average of the height is always 0, i.e. the global translation is removed from the trajectories at time t. The membrane height autocorrelation function is sensitive to any global rearrangement in membrane geometry and yields the relaxation time associated with such reorganization. Again we note that time t is fictitious as we ignore hydrodynamic interactions and the calculation of correlation functions is merely a numerical tool to assess convergence.

Even though it is more traditional to perform a Fourier analysis and compute the spectral intensity function $\langle |z(q)|^2 \rangle$ - here $z(q)$ is the Fourier transform of the membrane surface $z(x, y)$ - such a scaling function is only available when the curvature inducing proteins act independent of one another and not coupled to membrane dynamics [9] and is not available from theory for the case we are considering, namely, when the curvature inducing functions are themselves diffusing and coupled to membrane motion through Eq. 3.4. In the absence of curvature inducing functions, $\langle |z(q)|^2 \rangle$ scales as [100] $k_B T/[\kappa q^4 + \sigma q^2]$, and we have indeed verified this scaling by performing the TDGL of the free membrane and subsequently the Fourier analysis (data not shown); in fact the successful reproduction of this scaling was taken as an indication of the correctness of the implementation of our numerical TDGL code. We also note that the KMC code was validated by ensuring that the mean-squared displacement of the bound proteins on the flat membrane under zero intrinsic curvature followed the Einstein relationship.

3.3 Results and Discussion

3.3.1 Potential of Mean Force between Two Membrane-Bound Proteins

Most of the previous analyses have shown that membrane-deformation mediated energies tend to be repulsive and should prevent, rather than promote, the formation of protein dimers or clusters. Aranda-Espinoza et al. have previously calculated the membrane-mediated interaction between curvature inducing proteins [11]. The authors used a combination of integral equation theory to describe the spatial distribution of the membrane-bound proteins and the linearized elastic free energy model (considered in this work) and reported that the interaction between two membrane-bound curvature inducing proteins is dominated by a repulsive interaction. Consistent with these published reports, the calculated binding energy between two membrane-bound proteins (see Fig. 3.1) from our model is also dominated by repulsive interactions governed by the range of the curvature inducing function R. The profile for the interaction energy in Fig. 3.1 closely matches

the calculations of Aranda-Espinoza et al. [11]; this agreement serves as a validation of our model and calculations. Recently Kozlov has discussed how the effect of fluctuations can change the

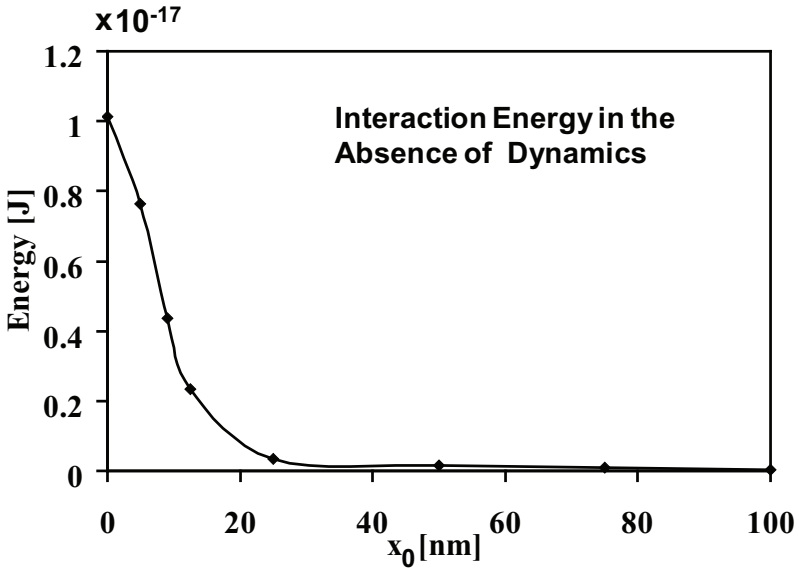

Figure 3.1: Interaction energy (total energy when 2 membrane-bound proteins are separated by a distance r minus twice the energy of membrane with one protein bound) between two membrane-bound stationary proteins at different distances of relative separation, r. Each protein induces curvature according to the H_0 function in Eq. 3.4; here each $C_0 = 40\ 1/\mu$m and R=100 nm.

repulsive nature of the interactions [90]. The author's discussion is based on the premise that any membrane protein locally restrains thermal undulations of the lipid bilayer. Such undulations are favored entropically, and so this increases the overall free energy of the bilayer. Neighboring proteins collaborate in restricting the membrane undulations and reduce the total free energy costs, yielding an effective (membrane-mediated) protein-protein attraction. Indeed, for the linearized free energy model, we can compute the second variation of energy, (note that at equilibrium, the first variation is zero, while the second variation governs the stiffness of the system against fluctuations) to explicitly show that the presence of a protein (or equivalently a curvature inducing function) leads to a localized suppression of membrane fluctuations. Namely,

$$\delta^2 E(z,\eta) = \frac{d^2}{d\epsilon^2} \int\int \frac{\kappa}{2} \left[\nabla^2(z+\epsilon\eta) - H_0\right]^2 + \left(\frac{\kappa}{4}H_0^2 + \frac{\sigma}{2}\right)\left(\nabla(z+\epsilon\eta)\right)^2 dxdy \tag{3.6}$$

which reduces to,

$$\delta^2 E(z,\eta) = \int\int \kappa(\nabla^2\eta)^2 + \left(\frac{\kappa}{2}H_0^2 + \sigma\right)(\nabla\eta)^2 dxdy \tag{3.7}$$

For any real valued function η, the integrand is always positive and hence, the second variation of energy is positive, which implies that at equilibrium the energy is indeed minimized. Eq. 3.5 also

suggests that the second variation of energy increases with increasing H_0, thus, larger spontaneous curvature leads to higher stiffness of the membrane and would result in smaller height fluctuations. This provides for the possibility that our linearized free energy model can support an entropically-mediated protein-protein attraction. The outcome of the interplay between the attractive entropic forces and the repulsive energetic forces is context specific as both have the same dependence on the protein-protein distance, and their absolute values differ only by coefficients with similar values. Thus, based on equations (3.1 and 3.7), we expect that the potential of mean-force between membrane-bound proteins (which is governed by this balance) will be strongly dependent on the magnitude and range of the curvature-inducing function (i.e. C_0 and R) as well as on the density ρ^*; in particular, for a certain regime spanned by these parameters (for which entropic effects dominate over the energetics) we can expect a net attractive force favoring protein clustering, see section 3.3.3. We emphasize that these results are not new to our work and have been discussed before [2, 34, 35] in other contexts and we have taken the agreement in trends between our calculations and these prior works as a validation of our model and simulations. It is also worth mentioning for completeness that Chou et al. [30] have extended the energetic analysis to membrane-bound proteins that have a noncircular cross-sectional shape and to local membrane deformation with saddle shaped (negative Gaussian curvature) and have shown that in such cases the interactions can be attractive even without considering fluctuations.

3.3.2 Emergent Membrane Response to Curvature-Inducing Proteins

Exploring a range of values of ρ^*, R, and C_0 in a series of KMC-TDGL simulations (other parameters, namely σ, κ, M, and T are fixed at values corresponding to a cytoskeleton-fortified phospholipid bilayer membrane at T=300 K), we find varying system behavior with respect to the membrane-height fluctuations, see Fig. 3.2(a-e). The parameter regime $[0.0 \leq \rho^* \leq 0.03, 20 \leq R/nm \leq 80, 10 \leq C_0 \times \mu m \leq 40]$ represents conditions under which regular thermal undulations of the membrane are captured and no nucleation of a vesicle-bud is observed. The evolution of the standard deviation in membrane height, i.e. $\sigma_z(t)$ typical of the emergent membrane height fluctuations in this regime, is provided in Fig. 3.2a. The insets depict the membrane height profile as a contour plot (points along a contour have the same height z and adjacent contours differ by 0.05 nm in z) at a single snapshot of the simulation time indicated by the corresponding arrows. In particular, the insets show regular undulations and no systematic patterns in the membrane height profile. In contrast, the membrane height profiles in the parameter regime $[0.008 \leq \rho^* \leq 0.016, 40 \leq R/nm \leq 100, 40 \leq C_0 \times \mu m \leq 60]$ show patterns of systematic vesicle-bud formation even under a low density of membrane-bound proteins; a profile of the emergent

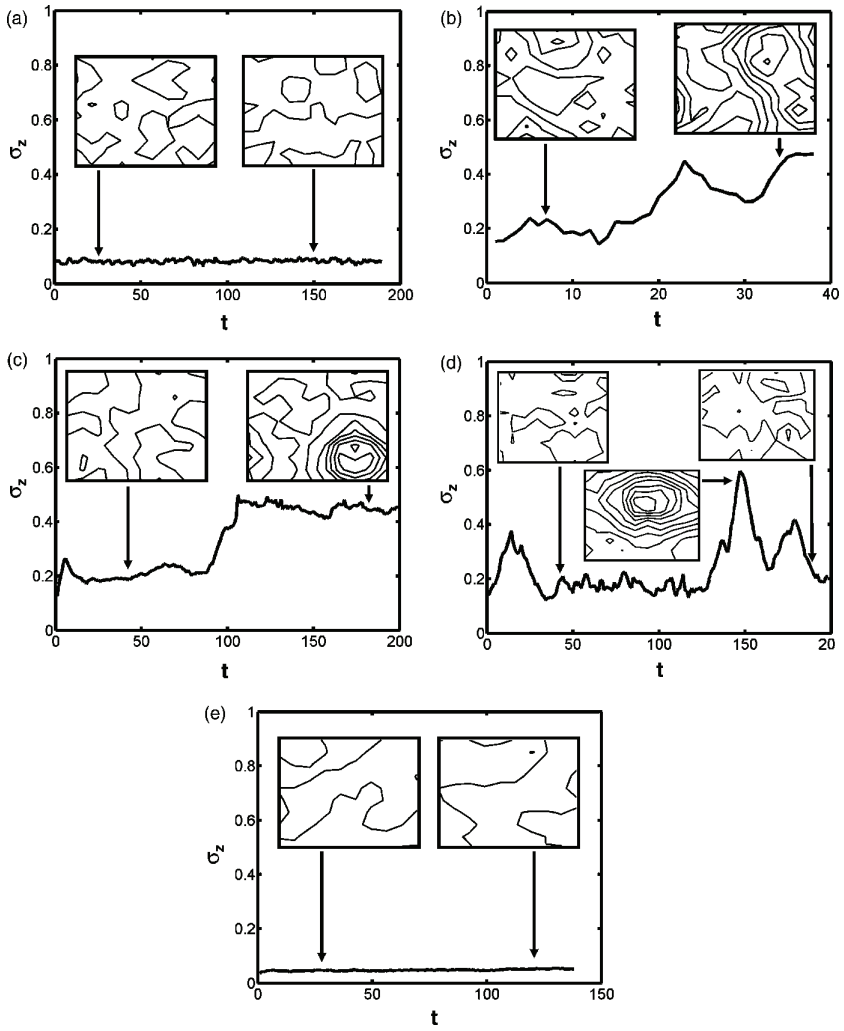

Figure 3.2: Standard deviation of the height profile as a function of simulation time, t: (a) ρ^*=0.03, R/nm=40, $C_0 \times \mu m$=15; (b) ρ^*=0.008, R/nm=60, $C_0 \times \mu m$=60; (c) ρ^*=0.016, R/nm=100, $C_0 \times \mu m$=20; (d) ρ^*=0.012, R/nm=80, $C_0 \times \mu m$=30; (e) ρ^*=0.03, R/nm=80, $C_0 \times \mu m$=5. Insets in each panel depict the contours of the membrane height profile (as well as a snapshot of the membrane profile) at the indicated simulation time. Adjacent contour lines have a height difference of 0.05 nm.

membrane response typical of this regime is depicted in Fig. 3.2b; in particular, the system evolves from a state of low σ_z in which no vesicle-bud is formed (left inset) to one of high σ_z in which a vesicle-bud appears (right inset). Thus tracking the transition of the σ_z value appears to be a reasonable indicator (order parameter) in identifying regimes that support vesicle-bud formation. The parameter regime $[0.012 \leq \rho^* \leq 0.024, 80 \leq R/nm \leq 100, 10 \leq C_0 \times \mu m \leq 30]$ also supports

vesicle-bud formation (see a typical scenario in Fig. 3.2c) but at lower values of C_0 and higher values of R, ρ^* relative to the previous case discussed. However, in contrast to the previous case (namely, Fig. 3.2b), the relatively higher density of membrane-bound proteins needed to elicit the transition is suggestive of a cooperative process leading to the vesicle-bud formation, see section 3.3.3. We note that the simulations in the regime $[0.008 \leq \rho^* \leq 0.012, R/nm = 80, 20 \leq C_0 \times \mu m \leq 30]$ also supported vesicle-bud formation, but unlike the previous two cases discussed (in which the vesicle-bud once formed was stable for the rest of the simulation), the bud was only metastable suggestive of a metastable state. The typical profile of this behavior is depicted in Fig. 3.2d. Finally, in the parameter regime $[0.024 \leq \rho^* \leq 0.03, 60 \leq R/nm \leq 80, 0 \leq C_0 \times \mu m \leq 10]$, see typical profile in Fig. 3.2e, the evolution of the membrane height profile suggested a state of repressed membrane undulations at a high density of membrane-bound proteins.

3.3.3 Cooperativity in Protein-Protein Interaction

In order to relate the context-dependent nature of the membrane-mediated protein-protein interaction (discussed in section 3.3.1) on the emergent membrane height-profile evolution (section 3.3.2), we further investigate the form of the potential of mean force (i.e., effective free energy of membrane-mediated interaction) between two membrane-bound curvature-inducing proteins by calculating the two-dimensional radial distribution functions, see Fig. 3.3 (top row), for the range of parameters ρ^*, R, C_0 explored in section 3.3.2. The radial distribution functions are characterized by repulsion between membrane-bound proteins at distances of R at which the range of the intrinsic curvature functions overlap. This parameter sets the dominant scale for the spatial localization and packing of the proteins on the membrane, and in a density dependent fashion we observe liquid like structuring. We note that at very short distances (equal to the protein exclusion diameter a_0) there is repulsion due to protein-protein overlap, however, due to the repulsion at R, which is greater than a_0, this regime is seldom explored in the protein conformations, see cases (a,b) in Fig. 3.3. However at moderate-to-high densities and moderate values of C_0 (Fig. 3.2c-e), the $g(r)$ is non-zero for $r < R$ and the repulsive energetic barrier is overcome to localize the protein-molecules at these short distances: for these cases, we observe correlations between proteins at two length scales, namely, that of the exclusion diameter, a_0 and that of the range of interaction R. It is notable that under the conditions of Fig. 3.3b, which support stable vesicle-bud formation, the localization of proteins at distances less than R is not a necessity. Moreover, the vesicle-bud formation is sustained even without any significant clustering of proteins as evidenced by the lack of structure in the $g(r)$ function. These characteristics suggest that the vesicle-bud formation under these conditions do not require any significant degree of cooperativity in protein-protein interaction and that in fact

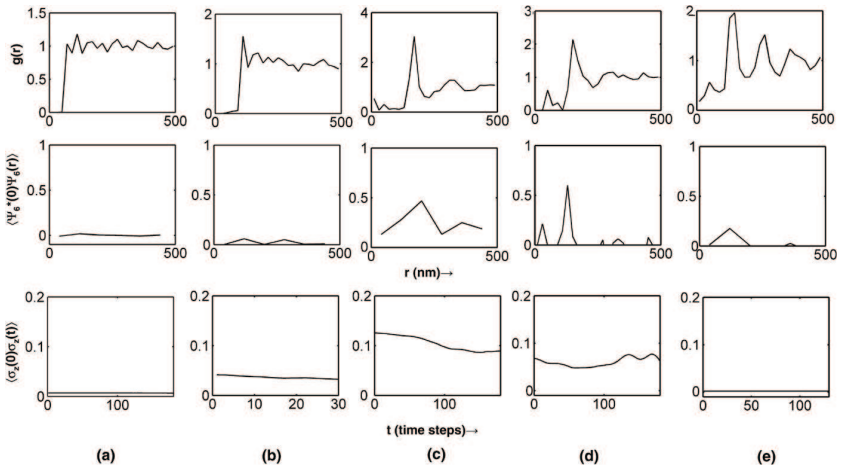

Figure 3.3: (Top Row): Radial distribution functions showing liquid-like order with the packing determined by the range R. (Middle Row): Orientational correlation functions up to $4R$. (Bottom Row): Height correlation functions showing the relaxation time associated with the dominant membrane undulation mode. The columns (a)-(e) correspond to cases (a)-(e) in Figure 2.

the large curvature (C_0) induced by each individual protein is the primary driver of the vesicle-bud formation. Hence we term this mode of nucleation as "NWC" or nucleation without cooperativity.

In contrast to the NWC regime, it is clear that the nucleation of the vesicle-bud in Fig. 3.3(c,d) are accompanied by significant spatial correlations as evidenced by the peaked $g(r)$ functions, suggesting protein-protein cooperativity as the orchestrator of the nucleation events. In order to determine, if the induction of spatial ordering leads to spatial patterning of the membrane-bound protein molecules, we calculate the orientational correlation functions, see middle row of Fig. 3.3. Intriguingly the orientational correlations are pronounced and significant only for the cases (c,d) and are practically absent in cases (a, b, and e) in Fig. 3.3. It is clear that the presence of orientational correlations under the regime of moderate C_0 and ρ^* correlates with the induction of vesicle-bud nucleation. Moreover, the nucleation event leads to the formation of a stable bud only if the orientational correlation persists beyond r_0, the location of the first peak in $g(r)$, (Fig. 3.3c), but the nucleated bud is only metastable and the system returns to the undulating membrane phase when this persistence is absent (Fig. 3.3d). We therefore conclude that in addition to protein co-localization, spatial patterning that sustains short-range orientational order beyond the first coordination shell is a necessary condition for the stabilization of the nucleated vesicle-bud. We term this regime of vesicle-bud nucleation as nucleation via orientational ordering or "NVOO". The requirement of sustained spatial and orientational correlations, which necessitates the involvement of multiple membrane-bound proteins, is indeed suggestive of a cooperative phenomena associated

with the NVOO nucleation event. We note that this notion of cooperativity emerging from our simulations is consistent with the analysis of Kim et al. [85], who have shown using an energetic analysis that in the zero temperature limit, clusters of larger than five membrane-bound curvature-inducing proteins can be arranged in energetically stable configurations. Among the regimes exhibiting no orientational correlations (namely cases a, b, and e in Fig. 3.3), the regime associated with case e is unique because the orientational correlations are absent despite the strongest manifestation of spatial correlations. Moreover, at the high density of membrane-bound proteins in this regime, the membrane-height fluctuations are repressed (see Fig. 3.2e), the membrane autocorrelation function is flat suggesting a suppressive behavior in membrane undulations, see Fig. 3.3: bottom row. We term this state of membrane fluctuations as "RU" for repressed undulation.

3.4 Conclusion

The trace of short-range positional and orientational order in response to parameter variation is plotted in Fig. 3.4a: the plot depicts the values of $g(r = r_0)$ and $\psi_6(r = r_0)$, where r_0 is the location of the first peak of $g(r)$. The different symbols represent different manifestations of membrane dynamics; the unfilled circles $[0.012 \leq \rho^* \leq 0.024, 80 \leq R/nm \leq 100, 10 \leq C_0 \times \mu m \leq 30]$ correspond to NVOO, squares $[0.008 \leq \rho^* \leq 0.012, R/nm = 80, 20 \leq C_0 \times \mu m \leq 30]$ to NVOO with only a metastable bud, and the filled hexagons $[0.008 \leq \rho^* \leq 0.016, 40 \leq R/nm \leq 100, 40 \leq C_0 \times \mu m \leq 60]$ correspond to NWC. The diamonds $[0.0 \leq \rho^* \leq 0.03, 20 \leq R/nm \leq 80, 10 \leq C_0 \times \mu m \leq 40]$ represent conditions under which no nucleation (or "NoN") is observed, and the triangles $[0.024 \leq \rho^* \leq 0.03, 60 \leq R/nm \leq 80, 0 \leq C_0 \times \mu m \leq 10]$ correspond to RU. The traces in Fig. 3.4a further support the previously stated trend that the induction of spatial correlation at larger densities of membrane-bound proteins $[0.012 \leq \rho^* \leq 0.024]$ leads to the induction of short-range orientational ordering only under certain conditions, see unfilled circles and squares and that for large values of the curvature induction (i.e., $C_0 \times \mu m \geq 40$), vesicle budding occurs even in the absence of positional and orientational order, (filled hexagons in Fig. 3.4a). Subject to the well appreciated approximations of the linear elastic model (described in section 3.2), the analysis of the collective behavior of protein-mediated membrane height-profile fluctuations leads to the development of a global state diagram when classified and plotted in-terms of the tunable parameters, namely, C_0, R, and ρ^*, see Fig. 3.4b. The state boundaries (dotted lines) are drawn approximately to separate symbols (regions) of distinct emergent dynamic behavior. The different symbols in Fig. 3.4b have a one-to-one correspondence with those in Fig. 3.4a and the dotted lines are a guide to the eye rather than representing co-existence lines; free energy estimates or

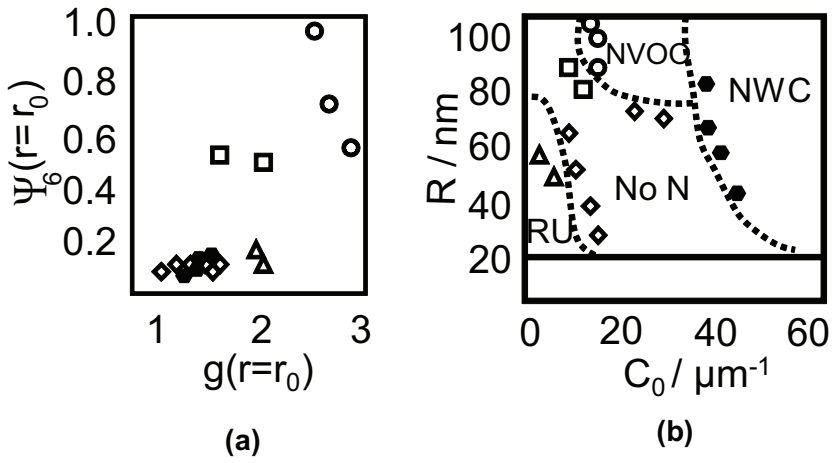

Figure 3.4: Trace of spatial and orientational correlations in response to changes in tunable system parameters ρ^*, R, and C_0. (b) Global state diagram for classifying membrane state behavior based on the observations recorded in (a). Parameter values used for each symbol is explained in Table 3.1.

	ρ^*	R [nm]	$C_0[1/\mu m]$	Symbol
a	(0,0.03]	[20,80]	[10,40]	Diamond
b	[0.008, 0.016]	[40,100]	[40,60]	Filled hexagon
c	[0.012,0.024]	[80,100]	[10,30]	Unfilled circle
d	[0.008,0.012]	[80]	[20,30]	Squares
e	[0.024,0.03]	[60,80]	(0,10]	Triangle

Table 3.1: Parameter Range Explored In Our Simulations

the challenging task of equating chemical potentials have not been carried-out. The state diagram depicts two regimes showing nucleation of vesicle-buds via distinct mechanisms (NVOO and NWC), the regime showing repressed undulations of the membrane at high protein density (RU), and an intervening regime showing no nucleation (NoN) with only regular thermal undulations in the membrane.

Several measures for experimental validation of the reported palette of membrane behavior and the predicted state diagram are possible. In particular, the surface density ρ^* can be tuned by varying protein concentrations, and C_0, R by studying different protein variants (wildtype vs. mutants) of epsin, AP180. The physical characteristics of protein-membrane interaction (i.e. C_0 and R values) may be characterized by a combination of microscopy and diffraction experiments [15,16]. In addition to the C_0 and R values, the frequency response of the system can be obtained from

dielectric relaxation spectroscopy [122,123]. Direct observation of membrane undulation and vesicle budding can also be obtained via defocussing microscopy [1, 2]. Collectively, these measures can yield an experimental phase diagram analogous to Fig. 3.4b.

In future work we plan to address the case of extreme curvatures by relaxing the linearization assumption in the elastic free energy and also extend our methodology to simulate the dynamics by including hydrodynamic interactions. These extensions will facilitate the application of our methodology to study the bioenergetics of cellular-biochemical processes such as receptor internalization via clathrin-mediated endocytosis [36], where it is well established that the curvature-inducing proteins associate with a hexagonal-lattice forming protein clathrin to orchestrate vesicle formation, however the precise sequence of events and mechanism remain unknown.

3.5 Appendix

3.5.1 Derivation of Diffusion Rates in Energy Landscape

While treating diffusion on a lattice via the MKC algorithm, we need to prescribe a rate associated with each event. For simplifying the derivation, we assume that diffusion process consists of elementary reactions where each reaction hops the particle (epsin in our case) to its nearest neighbor. In general, the following derivation holds true even if we relax the above simplification and allow jumps to non-neighboring lattice points as well.

We start with the master equation for a discrete set of states [170]:

$$\frac{dp_i(t)}{dt} = \sum_{j \neq i} \left(W_{ji} p_j(t) - W_{ij} p_i(t) \right) \tag{3.8}$$

where W_{ji} is the transition probability per unit time from state j to state i and $W_{ji} \geq 0$. $p_i(t)$ is the probability of being in state i at time t and hence $p_i(t) \geq 0$.

For simplification, we restrict our analysis to a one-dimensional lattice. The following form of W_{ij} has been used [6, 102, 176] when jumps to only nearest neighbors is allowed:

$$W_{ji} = \begin{cases} \frac{2D}{a_0^2} \exp\left(-\beta(E_i - E_j)\right) & : i - j = \pm 1 \\ 0 & : \text{otherwise} \end{cases} \tag{3.9}$$

With this form of W_{ji}, the master equation Eq. 3.8 reduces to:

$$\frac{dp_i(t)}{dt} = W_{i-1,i} p_{i-1}(t) + W_{i+1,i} p_{i+1}(t) - W_{i,i-1} p_i(t) - W_{i,i+1} p_i(t) \tag{3.10}$$

Assuming that $p_i(t)$ varies slowly with i, we can write p_{i-1} and p_{i+1} in terms of Taylor series expansion about p_i:

$$p_{i \pm 1} = p_i \pm a_0 \frac{dp_i}{dx} + \frac{a_0^2}{2} \frac{d^2 p_i}{dx^2} \tag{3.11}$$

For simplification, we also consider a simple linear energy landscape $E = \epsilon x$. Then Eq. 3.9 simplifies to:

$$\begin{aligned} W_{i-1,i} =& \frac{2D}{a_0^2} \exp\left(-\beta\epsilon a_0\right) \\ W_{i+1,i} =& \frac{2D}{a_0^2} \exp\left(\beta\epsilon a_0\right) \\ W_{i,i-1} =& \frac{2D}{a_0^2} \exp\left(\beta\epsilon a_0\right) \\ W_{i,i+1} =& \frac{2D}{a_0^2} \exp\left(-\beta\epsilon a_0\right) \end{aligned} \tag{3.12}$$

Substituting above equation and Eq. 3.11 in Eq. 3.10, we get

$$\frac{dp_i(t)}{dt} = D\left(e^{\beta\epsilon a_0} + e^{-\beta\epsilon a_0}\right)\frac{d^2p_i}{dx^2} + \frac{2D}{a_0}\left(e^{\beta\epsilon a_0} - e^{-\beta\epsilon a_0}\right)\frac{dp_i}{dx} \tag{3.13}$$

For small value of $\beta\epsilon a_0$, we can expand exp in terms of Taylor series as:

$$e^{\pm\beta\epsilon a_0} = 1 \pm \beta\epsilon a_0 \tag{3.14}$$

Substituting this linearized form of exp in Eq. 3.13, we get:

$$\frac{dp_i(t)}{dt} = D\left(1 + \beta\epsilon + 1 - \beta\epsilon\right)\frac{d^2p_i}{dx^2} + \frac{2D}{a_0}\left(1 + \beta\epsilon - 1 + \beta\epsilon\right)\frac{dp_i}{dx} \tag{3.15}$$

which reduces to

$$\frac{dp_i(t)}{dt} = 2D\frac{d^2p_i}{dx^2} + \frac{4D}{a_0}\left(\beta\epsilon\right)\frac{dp_i}{dx} \tag{3.16}$$

For the above simplified system, it is trivial to show that Smoluchowski equation takes the form [170]:

$$\frac{\partial p}{\partial t} = D\frac{\partial^2 p}{\partial x^2} + D\beta\epsilon\frac{\partial p}{\partial x} \tag{3.17}$$

Comparing Eq. 3.16 with the corresponding Smoluchowski equation 3.17 indicates that the form of transition probability, W_{ij} used in Eq. 3.9 does not give the correct form of Smoluchowski equation. We can show that the following form of W_{ij} (see Eq. 3.18) [106] reduces master equation 3.8 to the correct form of Smoluchowski equation 3.17.

$$W_{ji} = \begin{cases} \frac{D}{a_0^2}\exp\left(-\beta/2(E_i - E_j)\right) & : i - j = \pm 1 \\ 0 & : \text{otherwise} \end{cases} \tag{3.18}$$

Furthermore, we can also demonstrate that the above form of transition probability satisfies detailed balance at steady state:

$$W_{i,i-1}p_i = W_{i-1,1}p_{i-1}. \tag{3.19}$$

At steady state,

$$p \propto \exp(-\beta\epsilon x) \tag{3.20}$$

Hence, we get

$$\frac{D}{a_0^2}\exp(\beta\epsilon a_0/2)\exp(-\beta\epsilon x) = \frac{D}{a_0^2}\exp(-\beta\epsilon a_0/2)\exp(-\beta\epsilon(x-a_0)). \tag{3.21}$$

which simplifies to

$$\exp(\beta\epsilon a_0/2) = \exp(-\beta\epsilon a_0/2)\exp(\beta\epsilon a_0). \tag{3.22}$$

thus satisfying the detailed balance.

Chapter 4

Modeling the Bioenergetics of Protein-Mediated Vesiculation in Clathrin-Dependent Endocytosis

4.1 Introduction

In eukaryotic cells, the internalization of extracellular cargo via the endocytic machinery is an important regulatory process required for many essential cellular functions, including nutrient uptake and cell-cell communication. Several experimental [87] as well as theoretical [6, 103, 143] treatments have addressed mechanisms in endocytosis, yet the role of cooperative protein-membrane interactions in the ubiquitous endocytic pathway in mammalian cells, namely clathrin-dependent endocytosis (CDE), remains unresolved. A sequence of molecular events in CDE is responsible for the recruitment of adaptor protein 2 (AP-2), accessory proteins such as epsin, AP180, Eps15, Dynamin, etc., and the scaffolding protein clathrin to the plasma membrane [87]. The accessory proteins such as epsin are implicated in membrane bending [51]. Polymerization of clathrin triskelia results in the clathrin coat, and adaptor proteins such as AP-2, curvature-inducing proteins such as epsin interact with both the clathrin coat as well as the bilayer [136] to stabilize a clathrin-coated budding vesicle. The involvement of dynamin is believed to be in the vesicle scission step [87]. Even though actin is believed to play an important role in the endocytosis process in *S. cerevisiae* (yeast), in mammalian cells, actin repression, at best, has a small effect on endocytosis [81].

In this chapter, we focus on the energetic stabilization of a budding vesicle induced by the

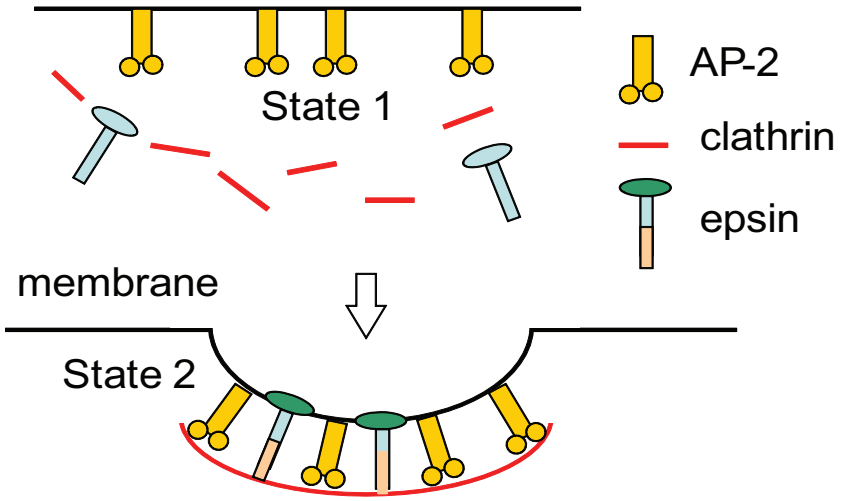

Figure 4.1: Reaction scheme for the clathrin coated vesicle formation. The free energy of state 2 relative to state 1 is described by $E_t(s_0)$.

clathrin-coat assembly. Recent work [74] demonstrates that the membrane invagination only begins in the presence of a growing clathrin coat [114]. Experiments performed by down-regulating AP-2 expression [73,115] as well as those involving the inhibition of epsin [79] either significantly decrease the number of clathrin-coated pits or alter the distribution of coated-intermediates involved in the vesicle-bud formation. Although the CDE in mammalian cells remains a complex regulatory process, we believe that a critical and self-consistent set of experiments is now emerging which warrants the formulation of physically-based models to quantitatively describe the bioenergetics of protein-induced vesicle formation in CDE. We formulate a minimal model, by restricting our focus to three proteins in the clathrin-coat assembly (Fig. 4.1): clathrin, epsin and AP-2, and their role in the stabilization of a budding vesicle on the cell membrane. Mammalian cells have a diverse set of proteins which often serve as surrogates and participate in compensatory mechanisms. In this regard, our choice for the ingredients for the minimal model represents the roles for the scaffolding proteins (clathrin), curvature inducing proteins (epsin) and the adaptor proteins (AP-2). We solve the membrane equations in a curvilinear manifold by assuming an underlying axis-symmetry using the surface of evolution formalism outlined by Seifert et al. [157]. We derive the equations governing membrane shapes of minimum energy under imposed curvature fields assuming that curvature fields are additive and that protein insertion does not cause spatial heterogeneities in physical properties of membrane such as bending rigidity and interfacial frame tension. Parameterizing the membrane shape by the angle $\psi(s)$, where s is the arc-length along the contour, we obtain $R' = \cos\psi$ and $z' = -\sin\psi$, where prime indicates the derivative with respect to arc-length s, (see inset, Fig. 4.2),

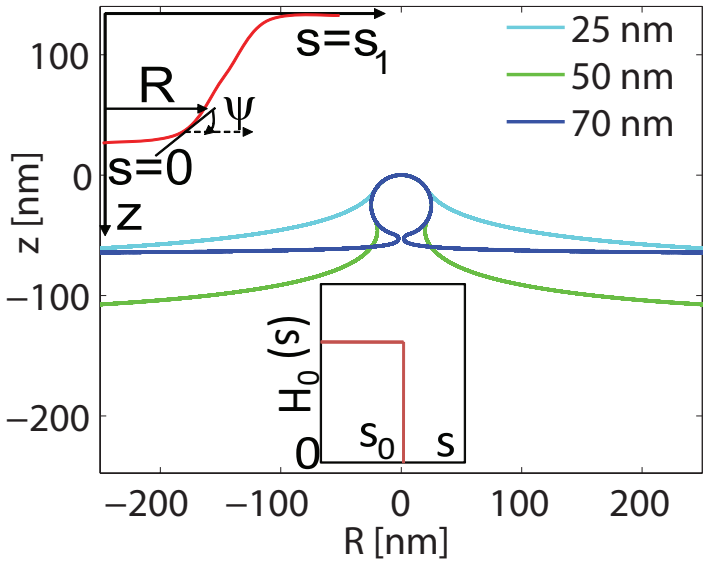

Figure 4.2: Three different membrane deformation profiles under the influence of clathrin imposed curvature for s_0=25, 50 and 70 nm. For s_0=70 nm, membrane shape is reminiscent of a clathrin-coated vesicle. Inset (top): A schematic of the membrane profile explaining various symbols in the surface evolution methodology. The full membrane profile is obtained by rotating the curve by 2π about the z-axis. Inset (bottom) shows spontaneous curvature function experienced by the membrane due to the clathrin coat assembly.

for topologically invariant membrane shape transformations, we neglect the Gaussian curvature terms and describe the membrane energy, E using the Helfrich formulation [72]. i.e.:

$$E = \int_A \frac{\kappa}{2}\left(H - H_0\right)^2 + \sigma dA \tag{4.1}$$

Here, H is the mean curvature of the membrane, H_0 is the imposed (or intrinsic) curvature of the membrane due to curvature-inducing proteins and is a function of arc-length s, σ is the membrane interfacial frame tension and A is the total membrane area. We express curvature H and the area element dA in terms of (s, R, ψ). Minimization of this energy functional leads to (see section 2.4):

$$\psi'' = \frac{cos(\psi)sin(\psi)}{R^2} - \frac{\psi' cos(\psi)}{R} + \frac{\nu sin(\psi)}{R\kappa} + \frac{\eta cos(\psi)}{R\kappa} + H_0'(s) \tag{4.2}$$

$$\nu' = \frac{\kappa[\psi' - H_0(s)]^2}{2} - \frac{\kappa sin^2(\psi)}{2R^2} + \sigma \tag{4.3}$$

$$R' = \cos\psi \tag{4.4}$$

Here, ν is a Lagrange multiplier introduced to satisfy the constraint $R' = \cos\psi$ (which defines R). We also impose the boundary condition $\psi = 0$ at $R = R_0$ (or at $s = s_1$) corresponding to

the pinning of the membrane by the cytoskeleton at the boundary of the membrane patch. In addition, due to the axis-symmetry, at $R = 0$, $\psi = 0$. Since the total arc-length s_1 is not known a priori, one additional closure equation is specified, (see section 2.4): $\nu(s_1) = \sigma R_0$. We solve the above system of boundary valued differential equations numerically by the shooting and marching technique [75], (see section 2.4.2), yielding membrane profiles for a specified spontaneous curvature function, and pinned at $R = R_0$; in this work, we employ $R_0 = 500$ nm. We also compute the curvature deformation energy of the membrane defined by:

$$E_c/\kappa = 2\pi \int_0^{s_1} 1/2 \left(H(s)\right)^2 R(s) ds. \tag{4.5}$$

We present our results for the case when interfacial frame tension σ is zero. Results obtained for non-zero σ (not shown) are found to be similar to the σ=0 case. We note that for σ=0, the Helfrich energy is directly proportional to κ making the membrane deformation profiles independent of κ in the absence of thermal fluctuations. (We also note that the entropic correction term $|T\Delta S|$ at T=300K is small, i.e. $\approx 5\%$ of the membrane bending energy for $\kappa = 20 k_B T$, see chapter 5). For a given membrane profile, the area of the coat $A_a(s_0)$ is computed using the relationship,

$$A_a(s_0) = 2\pi \int_0^{s_0} R(s) ds \tag{4.6}$$

where, $R(s_0)$ is the radius at the coat boundary.

Clathrin triskelia and AP-2 (in a ratio of 1:1) polymerize to form a coat [83] onto which epsins are recruited (see Fig. 4.1). Inclusion of epsin in the clathrin-coat accounts for epsin=-23 $k_B T$ per bound epsin; i.e., the ENTH domain of epsin binds to the PtdIns(4,5)P_2 lipid head groups on the membrane with a binding energy of -14 $k_B T$ per bound epsin [51] and the CLAP domain of epsin interacts with the α-appendage of AP-2 with an energy of -9 $k_B T$ [42]. Moreover, due to the periodicity of clathrin lattice (from cryo-EM studies [163], the average distance between adjacent vertices of the hexagons in the clathrin cage is 18.5 nm), the epsins are decorated on a hexatic bond-orientational-ordered template (Indeed in our previous work [6], we reported a study involving diffusion of curvature inducing proteins (epsins) on a membrane (curvature induction was modeled as described in section 4.2.1) in which we observed that at high concentrations, the epsins can effect the nucleation of a stable membrane bud formation; under these conditions, we found that epsin displays sustained (i.e. persistent over at least 3 nearest neighbor shells) hexatic bond-orientational ordering.). The interactions involving the ENTH domain allows us to estimate the intrinsic curvature contributions per epsin and the spatial/orientational templating of epsins allows us to estimate the number of epsins ($\approx$22) involved in a mature budded vesicle, see section 4.2.1 and Figures 4.5, 4.6. These interactions, collectively, constitute the effect of the clathrin-coat assembly on the membrane. In order to account for the effect of coat size on membrane deformation, we

further simplify our model and assume - (the assumption is validated below) - that the clathrin-coat assembly acts as a capsid imposing a constant and radially symmetric mean radius of curvature field on the membrane with $H_0 = 0.08$ 1/nm [79]. This value is consistent with the typical clathrin-coated spherical vesicles imaged in neuronal cells [79]; thus, we set $H_0(s) = 0.08$ 1/nm if $s < s_0$ and $H_0(s) = 0$ if $s \geq s0$, s_0 is the length of the clathrin coat assembly. We note that our "capsid model" is built on one more assumption - (partial experimental support to this notion is described in Ref. [43], see also section 4.2.2) - that we can study one nucleation event in isolation and that the interactions from other nucleation events in spatial proximity are not considered.

In Fig. 4.2, we depict membrane deformation profiles for different values of s_0; we find that above a critical value of s_0 (i.e. a critical size of the coat), the membrane profile develops overhangs (also evident from the behavior of the neck-radius in Fig. 4.3 inset), which when s_0 approaches 25π nm, transforms into a fully-mature spherical bud with a narrow neck. The validity of the simplified capsid model is bolstered by the close agreement in membrane profiles of the mature bud between Fig. 4.2 and Fig. 4.5. For each profile, the computed energy (E_c) required for the membrane deformation (Fig. 4.3) increases linearly with increasing coat area, $A_a(s_0)$. We also find that the computed energy E_c for a mature spherical bud is independent of the vesicle diameter for diameters ranging from 50 to 200 nm, (results not shown). For a cell membrane patch not fortified by cytoskeleton, which is typical for membrane patches smaller than 100 nm, $\kappa = 20 k_B T$ [21,184], and the energy $E_c(s_0)$ required to form a mature spherical bud of diameter 50 nm (or s_0=70 nm) is estimated to be 25κ=500 $k_B T$, see Fig. 4.3. The energy E_c required to deform the membrane (Fig. 4.3) can be offset by stabilizing interactions between the proteins in the clathrin coat assembly and between the coat proteins and the membrane. The free energy of the clathrin-coat assembly, $E_a(s_0)$ which includes the free energy of clathrin polymerization and the interaction of clathrin coat with adaptor proteins such as AP-2. Based on in vitro equilibrium data of clathrin cage formation, Nossal [127] estimated the energetics of a fully-closed clathrin/AP-2 basket (i.e., $R(s_0) = 0$) relative to a dissolved coat to be $E_a(s_0) \approx$ -20 $k_B T$, i.e., $|E_c| >> |E_a|$. This implies that the curvature induction in the presence of a clathrin-coat is energetically unfavorable in the absence of additional stabilizing interactions. Indeed, as reported in cell-experiments [43] (see also sections 4.2.1, 4.2.2), not all growing clathrin coats result in vesiculation events and a commitment step possibly accounting for additional stabilizing interactions (E_r which includes those interactions that preferentially stabilize state 2 over state 1 in Fig. 4.1) is necessary. Within our model, $E_r(s_0) = N_{epsins}(s_0) \times \epsilon_{epsin}$, where N_{epsins} represents the number of epsins incorporated in the clathrin-coat assembly; as described before, our model also estimates $N_{epsins}(s_0 = 25\pi$ nm) $\approx$22. Thus, for a given extent of the coat characterized by the length s_0, the total free energy change of

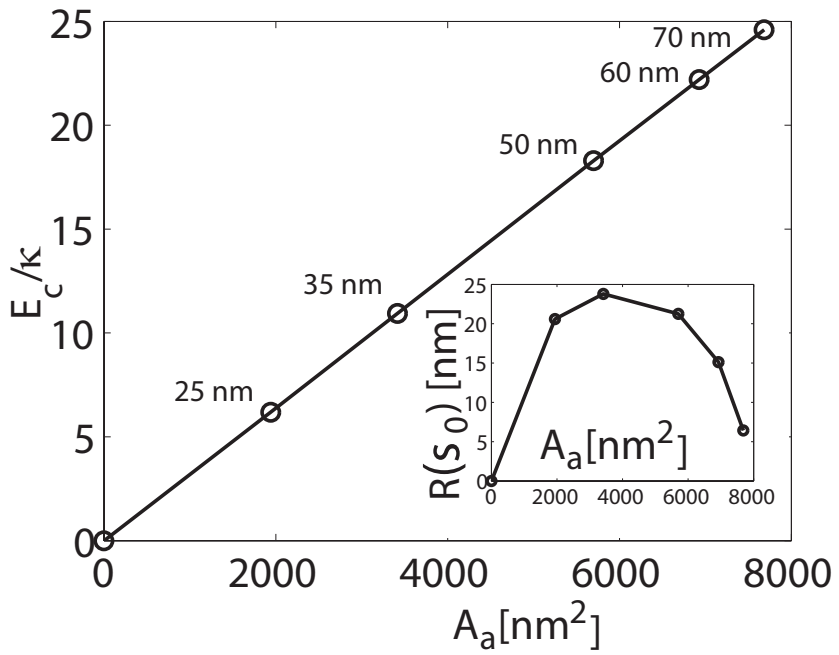

Figure 4.3: Curvature deformation energy of the membrane versus the area of the clathrin coat, $A_a(s_0)$ for different values of s_0: 25nm-70nm. Inset: vesicle neck-radius $R(s_0)$ plotted against coat area $A(s_0)$ for different values of s_0: 25nm-70 nm.

the membrane and clathrin-coat assembly in the curved state (state 2, see Fig 4.1) relative to the planar state (state 1, see Fig. 4.1) is given by: $E_t(s_0) = E_c(s_0) + E_a(s_0) + E_r(s_0)$.

Recently, Jakobsson et al. [79] have studied the role of epsin in synaptic vesicle endocytosis by inhibiting the interactions of epsin with clathrin using a CLAP antibody and those of epsin with membrane using an ENTH antibody. Microinjecting the CLAP antibody into neuronal cells, they observed while the total extent of clathrin coated regions in the periactive zone on the plasma membrane remained the same, the observed fractions of the coated regions in different stages of coated-vesicle budding prior to scission were altered in a dramatic fashion, (see Fig. S3): in the control (WT) cells, coated structures resembling a mature vesicular bud are more probable in comparison to planar structures and early intermediates; however, upon addition of CLAP, the early intermediates are stabilized and become more probable at the expense of the number of mature vesicular buds [79].

By employing ϵ_{epsin}=-23 k_BT and N_{epsins}=21 (which is very close to 22), the computed probability of observing different coated-intermediates of vesicular structures $P \propto \exp(-E_t(s_0)/k_BT)$ matches the experimental values of Jakobsson et al. [79] very closely, (compare Fig. 4.4 and Fig. 4.5). For modeling the clathrin-coated vesiculation in CLAP IgG injected cells, we compute the

number of epsins as N_{epsins}(CLAP cells)=N_{epsins}(WT cells)×Area of coated CLAP vesicles/Area of coated WT vesicles=33. The ratio of the respective areas (=1.6) is determined based on the experimental observations of increase in the size of the coated intermediates in CLAP injected cells relative to WT cells [79]. Remarkably, with N_{epsins}=33 and $\epsilon_{epsin} = -14\ k_BT$ (reduced from -23 k_BT due to the abrogation of the CLAP-clathrin/AP-2 interaction), we find not only that $E_t(s_0)$ increases monotonically with s_0 (a reversal in trend) but also the probability $P \propto \exp(-E_t(s_0)/k_BT)$ quantitatively matches the experimentally observed distribution in CLAP IgG injected cells, (compare Figs. 4.4 and 4.5). We note that even though N_{epsins} increase in the CLAP IgG injected cells relative to wildtype, the size of the bud increases due to a lack of hexatic bond-orientational order (i.e., the CLAP domains of epsin can no-longer bind the periodic clathrin lattice causing a heterogeneous distribution of epsins preferentially in areas of high curvature, e.g., the neck). Corroborating this view, many extended coated structures (cisternae) also appear in the experiments with CLAP IgG injected cells [79]. Furthermore, according to the predictions of our model, disrupting the epsin-membrane interaction (i.e., by targeting the ENTH domain of epsin) completely abrogates E_r and should make the coated vesicular bud highly unfavorable. Indeed, in cells microinjected with ENTH antibodies the extent of clathrin-coated structures decreased by >90%. [79]. In conclusion, we have presented a bioenergetic model which we believe imposes the correct thermodynamic constraints, as well as quantitatively explains several experimental observations on the process of vesicle nucleation induced by the clathrin-coated assembly prior to vesicle scission in CDE. While our model does not include the nucleation of the clathrin coat or the scission of a mature coated vesicular-bud, our results identify a unique dual role for the curvature inducing protein, epsin, namely its central role as a curvature inducer, and its role as an adapter in binding the clathrin coat to the membrane. Our results also suggest an important role for the clathrin lattice, namely in the hexatic-templating of the epsins for providing the appropriate curvature field for vesicle budding. These model predictions can further be quantified by engineering mutations in epsin, clathrin, and AP-2 all of which are predicted to influence the distribution of coated structures. The framework of our approach is generalizable to vesicle nucleation in clathrin-independent endocytosis. Indeed, based on our results we can speculate that alternative mechanisms (such as receptor clustering) which can provide a hexatic bond-orientational templating of epsins on the membrane can facilitate vesicle-bud formation independent of CDE [6].

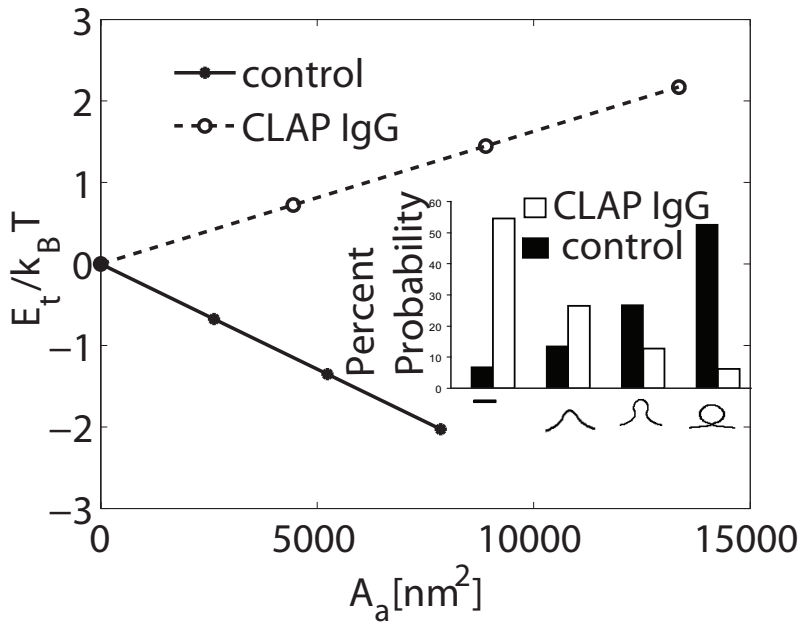

Figure 4.4: Energetics of the clathrin coated vesicular bud $E_t(s_0)$ versus coat area, $A(s_0)$. Number of epsins in WT (control) cell = 21 and in the CLAP IgG cell = 33.2. Inset: calculated probability of observing a clathrin-coated vesicular bud of given size in WT cells (filled) and CLAP IgG injected cells (unfilled).

4.2 Appendix

4.2.1 Epsin Induced Spontaneous Curvature

The dominant factor contributing to the intrinsic curvature H_0 in the region where the membrane binds to the clathrin coat is the presence of epsins, i.e., the vertices of the triskelia are also binding sites for epsins. In a recent study, [6], we modeled the spontaneous curvature induced by one epsin as a Gaussian function:

$$H_0 = C_0 e^{-s^2/b^2} \tag{4.7}$$

In vitro, Ford et. al. [51] observed that epsin tubulates the vesicles and the tubules have outer diameter of 20 nm. From this we estimate $C_0 = 0.1\text{nm}^{-1}$. Using the surface-evolution approach, we calculate the curvature deformation energy of the membrane, E_c when a single epsin is inserted into the bilayer. We argue that energy E_c is stabilized by the negative interaction energy of the ENTH domain of epsin with the bilayer, E_r. Hence, we choose the range b of the epsin induced curvature such that $E_c \approx |E_r|$. Using $E_r = -14k_BT$ [51], we obtain $b = 8.3$ nm. The role of the clathrin-coat is to template the epsins in a hexatic bond-orientational pattern. Hence, within our

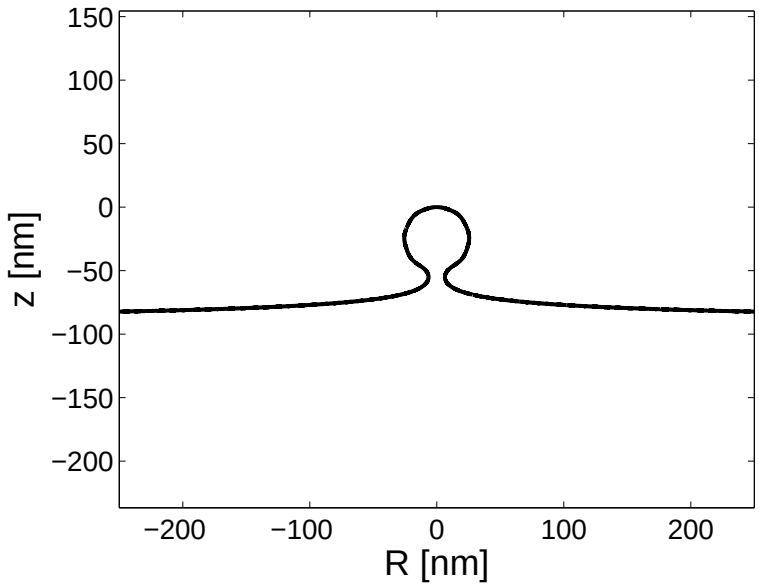

Figure 4.5: Membrane deformation profile under the influence of epsin imposed curvature. The full membrane profile is obtained by rotating the curve by 2π about the z-axis. The dimensions of this bud closely matches the dimensions of the clathrin-coated bud shown in Fig. 2.

axis symmetric model, this translates to multiple epsins are bound onto the membrane in concentric rings. In this case, the intrinsic curvature H_0 has the form:

$$H_0 = \sum_i C_0 e^{-(s-s_{0,i})^2/b^2} \tag{4.8}$$

where, the index i runs over the number of concentric rings. A cryoelectron microscope image of the clathrin cage indicates that the distance between vertices of the hexagons in the clathrin cage is about 18.5 nm [163]. Since the epsin binding sites are located at the vertices, the distance between epsin concentric rings would be multiples of 18.5 nm. We assume that one epsin is adsorbed at R=0, i.e. $s_{0,1} = 0$. Rest of the epsins are adsorbed in rings, with $s_{0,2} = 18.5$ nm, $s_{0,3} = 37$ nm and $s_{0,4} = 55.5$ nm. The minimum energy membrane shape with these choices of curvature function and parameters is shown in Fig. 4.5. For the 50nm diameter vesicle we obtain in Fig. 4.5, we estimate the number of epsins, $N_{epsins,i}$ in each shell as:

$$N_{epsins,i} = \frac{2\pi R(s_{0,i})}{18.5} \tag{4.9}$$

where, $R(s)$ is calculated based on the $R(s)$ versus s shown in Fig. 4.6. For the choice of the above-mentioned curvature function, we get total number of epsins to be 22.5. The close agreement between Fig. 4.5 and Figure 2 not only provides a mechanistic basis for employing a constant

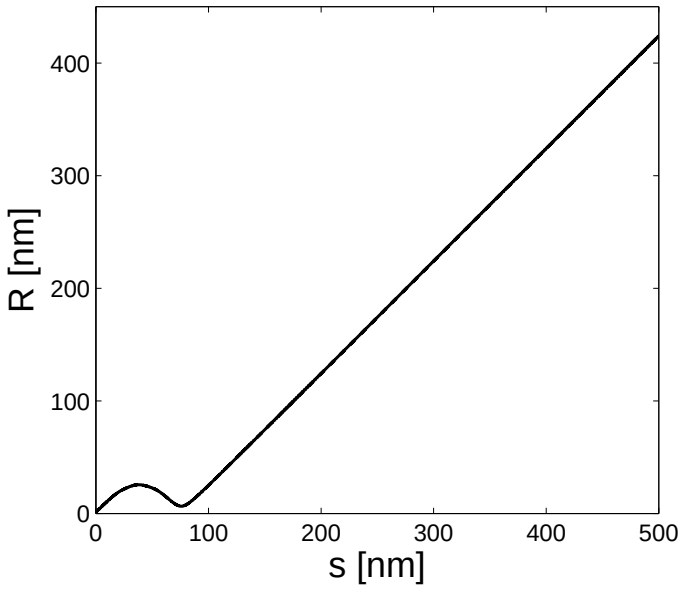

Figure 4.6: The radius of membrane profile shown in Fig. 4.5 as a function of membrane arc-length, s.

H_0 over the extent s_0, but also allows us to estimate the number of epsins (≈ 22) involved in the formation of a coated vesicle of diameter 50 nm. Thus, due to the stated self-consistency constraint, we have estimated the number of epsins involved without any fitting. Our results also makes clear that it is the embedded epsins on the clathrin coat that have a major contribution to H_0.

4.2.2 Nucleation and Growth of Clathrin Coat

The experiments that have reported the characteristics of nucleation of the clathrin coat are described in Refs. [43, 73]. While nucleation and growth of the clathrin coat are not directly included, they impact our model through the extent of the coat s_0. A few connections are described below.

Nucleation Site:

The clathrin coat nucleates by recruitment of (currently unidentified) components at some random positions on the inner leaflet of the plasma membrane. Due to compartmentalization of the plasma membrane into domains (due to presence of the cytoskeletal anchors), the initiation occurs randomly only within the subdomains devoid of cytoskeletal elements: in BSC1 cells, such domains appear to be 400 nm in diameter surrounded by a rim of a 200 nm "dead zone". The nucleation of clathrin coats was observed only in the 400 nm region and cytoskeletal constituents were only imaged

beyond the dead zone (i.e. outside of the 600 nm) region. These observations validate the basis (cytoskeletal anchoring) of the pinned boundary condition at the patch boundary.

Nucleation and Growth:

Based on their observations, Ehrlich et al. [43] reported that once nucleated, the clathrin coat continues to grow with recruitment of additional triskelia and accessory proteins to the nucleated coat. While concrete experimental evidence does not exist, the authors surmise that the size of the critical nucleus may be as small as involving 1-3 triskelia. However, the authors were able to deduce some important timescales:

1. In the growth phase, the addition of clathrin proceeds at a steady rate of about one triskelion every 2 s.
2. The 6-second-old coats have 10-20 clathrins.
3. At this point, two fates are possible: either the coats transform into a vesicle, or they abort.
4. The majority of the coats that abort contain about 10-40 triskelions. The dissolution of such abortive coats (in monkey kidney epithelial cells stably expressing LCa-YFP) is rapid. Whether the mechanism associated with this step is active (e.g., catalyzed, for example, by Hsc70) or otherwise is an important open question. This observation suggests that the coat sizes are bounded, i.e., we do not expect to see clathrin domains grow to large sizes.
5. Of the coats that do not abort, 20-second-old coats have about 40 clathrins and in 32 s the structure resembles a coated vesicle, i.e. a soccer ball structure (50-100 nm diameter depending on cell type). 100 nm diameter vesicles are coated completely by about 60 triskelia.

We note that, our model applies to just one of the maturing vesicles. While there may be other coats nearby, the effect of such coats is not included (the background H_0 is neglected) in our model. Our model also does not account for the clathrin coat nucleation step (or the vesicle scission after the mature bud has formed).

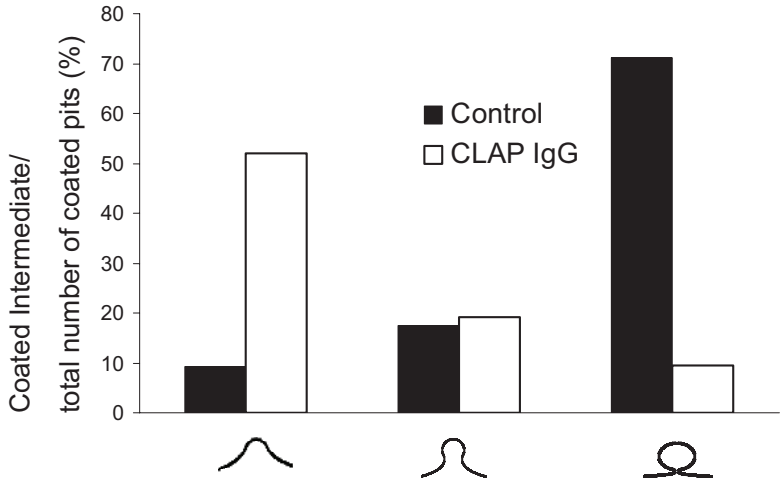

Figure 4.7: Experimental probability of observing a clathrin-coated vesicular bud of given size in WT or control cells (filled) and CLAP injected cells (unfilled) [79]

.

Chapter 5

Calculation of Free Energies in Fluid Membranes Subject to Heterogeneous Curvature Fields

5.1 Introduction

Cell-membrane deformations are often orchestrated by protein-membrane interactions [111, 186] which mediate several intracellular trafficking events [87, 129, 155]. Accordingly, theoretical modeling and experimental study of membranes and protein-membrane interactions at multiple resolutions is a central objective in biophysics [20, 30, 65, 96, 108, 126, 143, 157]. In this article, we employ phenomenological theories based on generalized elasticity (see below) [125, 147] in order to describe mesoscopic (at the $\sim \mu$m resolution) behavior of membranes, membrane undulations, and curvature modulations [33, 100, 141, 174, 177]. These models have been extensively employed, and specific choices of the governing equations (e.g., the form for membrane free energy) have been validated based on experimental studies. Hence, at the mesoscopic scales such models are considered reliable; however, a major challenge has been in tailoring them for quantification of free energies.

In a classic article, Helfrich [72] described the elastic energy of a fluid membrane by the Hamiltonian:

$$E = \int\int \left[\frac{\kappa}{2}\left(H - H_0\right)^2 + \overline{\kappa} K\right] dA + \sigma\left(|A - A_{flat}|\right), \tag{5.1}$$

where A is the total area of the membrane, dA is the differential area element, A_{flat} is the projected area of the membrane patch on a plane, H and K are the mean curvature and the Gaussian

curvature of the membrane, respectively. The membrane Hamiltonian depends on the frame tension σ, the bending rigidity κ, the splay modulus $\overline{\kappa}$ and the intrinsic curvature field H_0. Considering only those membrane shapes for which the overall membrane topology does not change, the contribution of Gaussian curvature to the Helfrich Hamiltonian is a constant. Within the Helfrich Hamiltonian, the effect of protein-induced curvature is treated through the H_0 term [6] which, in general, is a spatially varying function. To make the analytical and numerical calculations tractable, we only consider small deformations of the membrane, in which case, the membrane shape can be represented in a Monge or a Cartesian gauge as z=z(x,y). The resulting Helfrich Hamiltonian obtained by simplifying the expressions for the mean curvature and the differential area element in Eq. 5.1 is given by [6]:

$$E = \int\int \left[\frac{\kappa}{2}\left(\nabla^2 z - H_0\right)^2 + \left(\frac{\kappa}{4}H_0^2 + \frac{\sigma}{2}\right)(\nabla z)^2\right] dxdy \tag{5.2}$$

In previous studies, the Hamiltonian described in Eq. 5.2 with $H_0 = 0$ has been employed to describe various membrane-related phenomena. Lin et. al. [100] performed dynamics simulations accounting for implicit hydrodynamic coupling between the membrane and the surrounding solvent in the presence of cytoskeletal interactions. Reister-Gottfried [141] extended this methodology to account for the Brownian dynamics of the proteins on the fluctuating membrane. Veksler [171] analyzed the problem of membrane protrusions and protein phase separation by including additional terms in Eq. 5.2 to account for the protein concentration field. Seifert [157] has minimized Helfrich Hamiltonian given by Eq. 5.1 for non-zero values of H_0 at zero temperature to calculate the phase diagram for vesicle shape transformations. Although these works have highlighted the applicability of Helfrich Hamiltonian in a variety of membrane-related processes, calculating the free energy change associated with these processes has remained a challenge.

The calculation of the free energy of a freely fluctuating membrane with zero-spontaneous curvature within the Helfrich Hamiltonian can be accomplished analytically using a quasi-harmonic analysis of the Fourier modes [23, 37, 100, 174]. However, using the same approach, calculating the free-energy when the membrane is subject to non-zero and spatially varying H_0 becomes analytically intractable [37]. In such a case, a robust numerical method is desirable because the ability to compute free energy changes enables the prediction of relative stabilities of different states using which several critical questions can be addressed: these include, the quantification of the free energy change when a planar membrane deforms under the influence of curvature inducing proteins at a finite temperature, the role of membrane entropy in mediating interactions between curvature-inducing proteins [90], etc. It is our goal in this article to present a simulation methodology capable of addressing these questions. Calculation of free energy changes associated with reversible thermodynamic processes have been described extensively for molecular systems [9,54]. We employ

the rigorous and popular method of thermodynamic integration (TI) [54] to calculate the free energy change along a coupling parameter characterizing the Hamiltonian. Such a method has recently been applied within classical field-based simulations of polymer solutions [98].

We demonstrate the applicability in a model system of membrane deformations caused by a static (i.e. non-diffusing) heterogeneous curvature field. The model is characterized by a radially symmetric mean curvature field on the membrane over a localized region characterized by a linear extent r_0 (Figure 1). The value of H_0 is taken to be zero in membrane regions falling outside the localized region. Thus, the induced curvature field is described by:

$$H_0 = C_0\Gamma(r_0), \tag{5.3}$$

where $\Gamma(r_0)$ is a function that it is unity within a circular domain (centered at zero) of radius r_0 and zero otherwise, and r_0 is the linear extent (radius) of the curvature-field projected on the x-y plane. For the sake of illustration, we choose $C_0 = 0.04$ 1/nm. We calculate the free energy change of the membrane as a function of the extent of the curvature field (r_0) as well as the magnitude of the curvature field (C_0). We also present a quasi-harmonic analysis of a simplified (1-dimensional analog) membrane system with non-zero intrinsic curvature to validate the trends uncovered by our free energy calculations.

5.2 Methods

5.2.1 Thermodynamic Integration (TI) along C_0

For a system whose energy depends on a coupling parameter, λ, the partition function can be written as [54, 98]:

$$Q(\lambda) = c \int exp\left[-\beta E(\lambda)\right] dr^N, \tag{5.4}$$

where, c is a constant. Since the Helmholtz free energy $F = -k_B T \ln Q$, the derivative of the free energy with respect to λ can be written as:

$$\left(\frac{\partial F}{\partial \lambda}\right)_{N,V,T} = -\frac{1}{\beta}\frac{\partial}{\partial \lambda}\ln Q, \tag{5.5}$$

yielding,

$$\left(\frac{\partial F}{\partial \lambda}\right)_{N,V,T} = \left\langle \frac{\partial E}{\partial \lambda} \right\rangle_{\lambda}. \tag{5.6}$$

In Eq. 5.2 and Eq. 5.3, when C_0 is set to zero, we recover a planar membrane while for non-zero values of C_0, we obtain the desired state of the curvilinear membrane. We also note that the energy functional (Eq. 5.2) is differentiable with respect to C_0 but not differentiable with respect

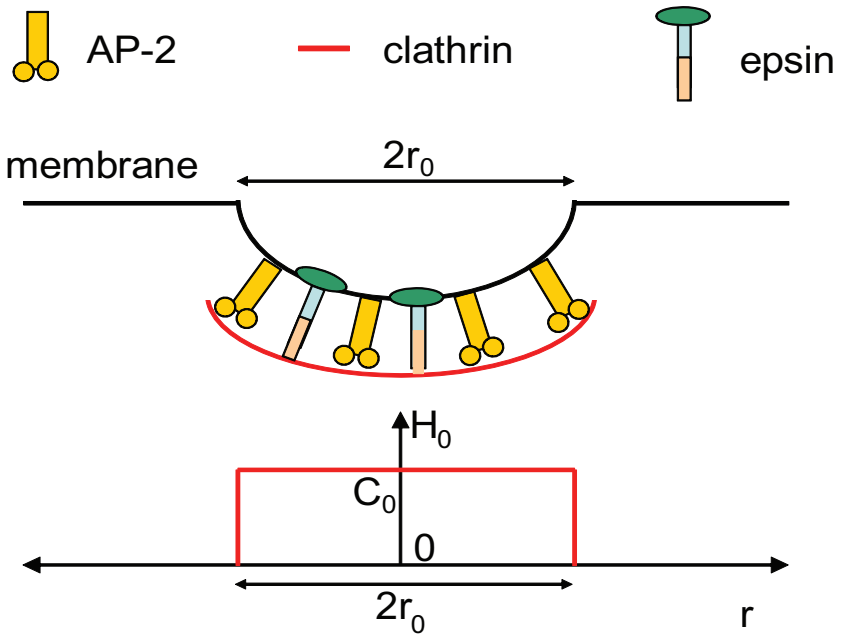

Figure 5.1: A depiction of membrane vesiculation in the presence of the clathrin-coat assembly. The lower panel depicts the form of spontaneous curvature function H_0, corresponding to a region of induced curvature of linear extent r_0.

to r_0. Hence, to compute the free energy changes, we choose C_0 as the thermodynamic integration variable (i.e. as the coupling parameter λ in Eq. 5.6) to obtain:

$$\frac{\partial F}{\partial C_0} = \left\langle \frac{\partial E}{\partial C_0} \right\rangle_{C_0}. \tag{5.7}$$

Using the expression for E from Eq. 5.2, we obtain:

$$\frac{\partial F}{\partial C_0} = \left\langle \Gamma(r_0)\kappa \int\int \left[-\left(\nabla^2 z - C_0\Gamma(r_0)\right) + \left(\frac{C_0}{2}\right)(\nabla z)^2 \right] dxdy \right\rangle_{C_0}, \tag{5.8}$$

Upon integration along C_0, this yields:

$$F(C_0, r_0) - F(0, r_0) = \int_0^{C_0} \left\langle \Gamma(r_0)\kappa \int\int \left[-\left(\nabla^2 z - C_0\Gamma(r_0)\right) + \left(\frac{C_0}{2}\right)(\nabla z)^2 \right] dxdy \right\rangle_{C_0} dC_0. \tag{5.9}$$

Here, $F(C_0, r_0) - F(0, r_0)$ is the free energy change as derived from the partition function in Eq. 5.4, where the energy is defined in Eq. 5.2. However, we are interested in deformation free energy, F_0, with reference to a state where $H_0 = 0$ which can be calculated from the relationship, (see Appendix 5.4.1):

$$F_0 = F + \langle E_0 \rangle - \langle E \rangle, \tag{5.10}$$

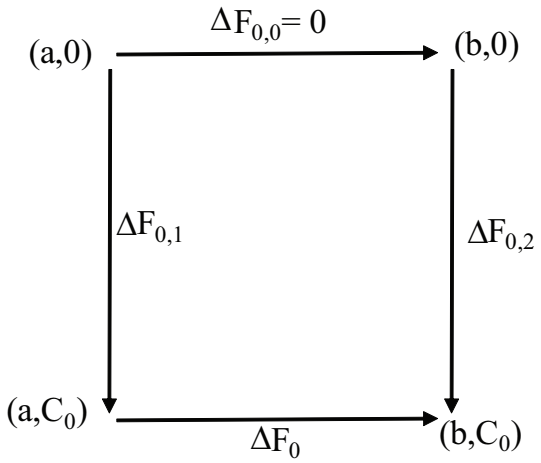

Figure 5.2: Thermodynamic cycle to calculate ΔF_0: $\Delta F_0 = -\Delta F_{0,1} + \Delta F_{0,0} + \Delta F_{0,2}$. a and b are the extent of the curvature-induced regions (r_0 values) while C_0 is the magnitude of the curvature. $\Delta F_{0,1}$ and $\Delta F_{0,2}$ are computed using Eq. 5.9.

where, E_0 is defined as:

$$E_0 = \int\int \left[\frac{\kappa}{2}\left(\nabla^2 z\right)^2 + \frac{\sigma}{2}\left(\nabla z\right)^2\right] dxdy. \tag{5.11}$$

Thus, $\Delta F_0 = F_0(C_0, r_0) - F_0(0, r_0)$ gives the deformation free energy change for a given extent of the localized region r_0 (such as size of the clathrin coat, see Fig. 5.1), when C_0 is varied. To calculate the free energy as a function of r_0 for a fixed C_0, we employ a thermodynamic cycle defined in Fig. 5.2. In this cycle, $\Delta F_{0,1}$ and $\Delta F_{0,2}$ required to deform a planar membrane to $H_0 = C_0\Gamma(r_0 = a)$ and $H_0 = C_0\Gamma(r_0 = b)$, respectively, are calculated through Eq. 5.9 and Eq. 5.10.

5.2.2 Simulation Protocol

The equilibrium sampling of membrane conformations according to the Boltzmann distribution for a given value of C_0 is performed using the Time-Dependent Ginzburg Landau (TDGL) simulations, using a protocol employed in our previous work [6,96]. In this protocol, we generate new membrane configurations from existing ones by numerically integrating the equation:

$$\frac{\partial z(\mathbf{r}, t)}{\partial t} = -M\frac{\delta E}{\delta z} + \xi(\mathbf{r}, t), \tag{5.12}$$

where,

$$\frac{\delta E}{\delta z} = \kappa H_0\left(\nabla z \cdot \nabla H_0\right) + \left(\frac{\kappa}{2}H_o^2 + \sigma\right)\nabla^2 z - \kappa\nabla^4 z + \kappa\nabla^2 H_0. \tag{5.13}$$

In Eq. 5.12, t represents a fictitious time, M is a scalar mobility term and ξ is the thermal noise term, which is drawn randomly from a Gaussian distribution with zero mean and with variance

System	Length [nm]	κ [k_BT]	σ [μ N/m]
I	250	20	0
II	250	50	0
III	250	50	3.0
IV	500	50	3.0

Table 5.1: Parameters employed in different systems. Length L of the membrane is discretized into 50 grid points and temperature of 300 K is set for all systems

depending on the temperature T, i.e. $\langle \xi(\mathbf{r},t) \rangle = 0$ and $\langle \xi(\mathbf{r},t)\xi(\mathbf{r}',t') \rangle = 2k_BTM\delta(t-t')\delta(\mathbf{r}-\mathbf{r}')$. This ensures that membrane configurations generated by Eq. 5.12 are consistent with the canonical ensemble with probability $\propto \exp(-E/k_BT)$.

Our simulations are performed for a system size of $L \times L$ in x, y dimensions, respectively, with periodic boundary conditions implemented in the xy plane. The length parameters (L values) for the different systems we have considered are summarized in Table 5.1. For each system, the membrane is discretized using a 50×50 set of spatial grid points in the xy plane, each with a fixed grid length of $h = L/50$ nm. All the derivatives on the right-hand side of Eq. 5.13 are approximated using a second-order centered-difference scheme. TDGL equations are then integrated in time using an explicit Euler scheme [75]. The time-step of integration Δt is set to be 1 ps based on linear stability analysis (see section 2.3.4). We choose a value of M ($= 2.5 \times 10^{-6}$ m^{2}s/kg) such that the normalized membrane height autocorrelation $\langle z(t)z(0) \rangle / \langle z^2 \rangle$ obtained in our simulations (when $C_0 = 0$, i.e. for system II in Table 5.1) matches closely, (see section 2.3.3 and Fig. 2.2), with that obtained using the Oseen tensor formalism [38] (in which M is a spatially varying tensorial quantity). The latter incorporates hydrodynamic interactions and represents membrane dynamics in an infinite surrounding fluid in the Stokes regime [100]. Additionally, we note that our results for the equilibrium properties are independent of the value of mobility term, M [6]. TDGL integration is performed for 200 million steps (i.e. 0.2 ms). The first 50 million steps are regarded as equilibration steps and are not included in computing the thermodynamic properties.

By carrying out TDGL simulations with the parameters listed in Table 5.1, the values of the integrand on the right-hand side of Eq. 5.9 for different values of C_0 are computed (C_0 is varied from 0 to 0.04 in increments of 0.005 1/nm). Hence, for each value of r_0, in total, 9 independent TDGL simulations are performed with different values of C_0. The integral on the right-hand side of Eq. 5.9 is then computed from these 9 values using the Trapezoidal rule [75]. The process is repeated for $r_0 = 10$, 20, and 30 nm. For each value of r_0, mean energy of the membrane $\langle E_0 \rangle$

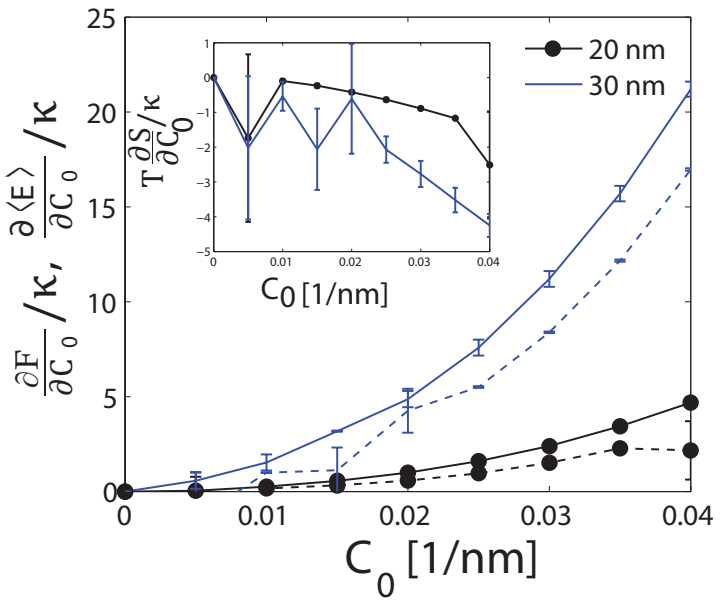

Figure 5.3: $\frac{\partial F}{\partial C_0}$ (solid lines) and $\frac{\partial \langle E \rangle}{\partial C_0}$ (dotted lines) plotted for two values of r_0 = 20nm and 30 nm for system II. The inset shows $T\frac{\partial S}{\partial C_0}$ as a function of C_0.

(defined in Eq. 5.11) for $C_0 = 0.04$ 1/nm is also computed from the TDGL sampling. Standard deviation (for the estimation of error bars) is computed by processing four separate blocks from two independent simulations, each block corresponding to 75 million steps of integration [9, 95].

5.3 Results

5.3.1 Calculation of Membrane Free Energy

We report our numerical results for the free energy changes obtained using thermodynamic integration: as evident from Fig. 5.3, $\frac{\partial F}{\partial C_0}$ increases with increasing value of C_0 implying that the free energy of the membrane, F, increases with increasing magnitude of C_0. Furthermore, for a larger extent r_0, the increase in free energy is larger for a same change in C_0. In Fig. 5.3, we also depict the calculated values of $\left(\frac{\partial \langle E \rangle}{\partial C_0}\right)_{r_0}$ for different values of C_0, r_0. The quantity $\frac{\partial \langle E \rangle}{\partial C_0} - \frac{\partial F}{\partial C_0}$ derived from these two plots yields the entropic contributions $T\frac{\partial S}{\partial C_0}$, which are plotted in the inset of Fig. 5.3. As evident from these figures, the entropy of the membrane decreases as C_0 increases, with the decrease more prominent for larger values of r_0. Using the thermodynamic cycle shown in Fig. 5.2, we also calculate the membrane deformation free energy change as a function of the extent of r_0. Since we are interested in computing the deformation free energy change (Appendix 5.4.1) with

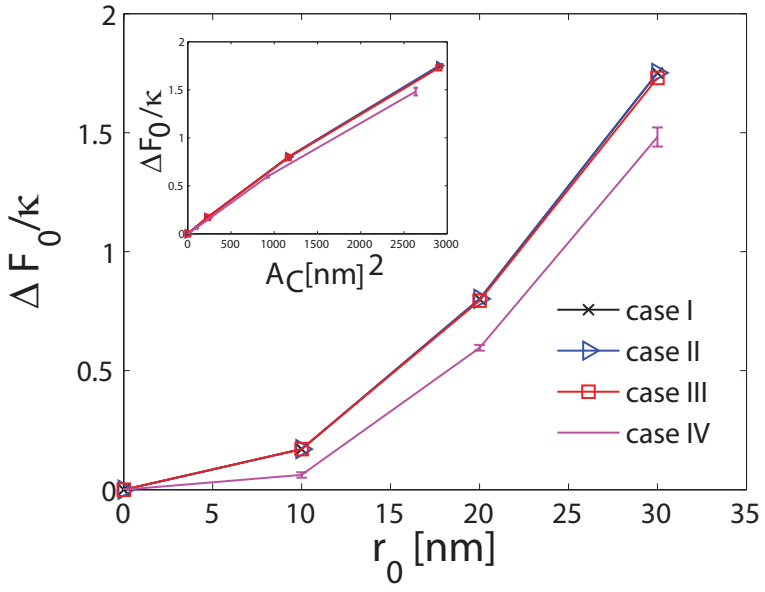

Figure 5.4: Membrane free energy change as a function of r_0.

respect to a planar membrane (i.e. $H_0 = 0$), we compute the mean energy, $\langle E_0 \rangle$ with respect to planar membrane, where E_0 is defined in Eq. 5.11. The change in the deformation free energy (F_0), the mean deformation energy (E_0), and the entropy (TS) with respect to a planar membrane are plotted in Fig. 5.4, 5.5, and 5.6, respectively, for the four different systems listed in Table 5.1.

The deformation free energy of the membrane increases as the extent of the curvature field r_0 increases. Furthermore, changes in the non-dimensional deformation free energy, F_0/κ, and mean deformation energy, E_0/κ are similar for the first three systems in Table 5.1. Thus, for the parameter values considered in this work, $\Delta F_0/\kappa$ and $\Delta E_0/\kappa$ depend only weakly on membrane bending rigidity κ and membrane frame tension σ. Insets in the Figs. 5.4 and 5.5 depict the variation of $\Delta F_0/\kappa$ and $\Delta E_0/\kappa$ with area of the localized region subject to the curvature field, A_c, defined as:

$$A_C = \int\int \Gamma(r_0) \left(1 + \frac{1}{2}(\nabla z)^2\right) dxdy. \tag{5.14}$$

This trend is almost linear demonstrating that membrane free-energy is a linear function of A_C, for small deformations considered here. Interestingly, the increase in $\Delta F_0/\kappa$ is smaller for the larger membrane size. Noting that the difference in the entropy change for different sizes of membrane is small, the changes in $\Delta F_0/\kappa$ values are a reflection of the changes in $\Delta E_0/\kappa$.

To further dissect the calculated dependence of E_0/κ on L, we note that the Eq. 5.11 can be

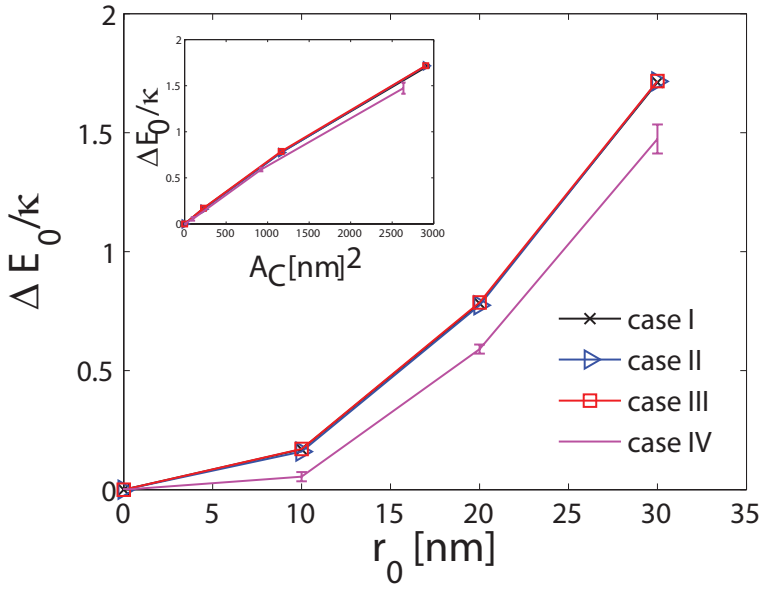

Figure 5.5: Membrane energy change as a function of r_0.

written in discrete form as:

$$E_0 = \sum_{i=1}^{N^2} \left[\frac{\kappa}{2} \left(\nabla_i^2 z \right)^2 + \frac{\sigma}{2} \left(\nabla_i z \right)^2 \right] h^2. \tag{5.15}$$

where ∇_i^2 and ∇_i are the Laplace and the Gradient operator evaluated at grid point i. Between systems III and IV, the number of grid points remains the same, while the grid length, h increases by a factor of 2. Since, the total number of degrees of freedom remains the same, the total energy from equipartition is also the same. This implies that the terms $\left(\nabla^2 z\right)^2$ and $\left(\nabla z\right)^2$ are smaller in system IV relative to system III in order to compensate for increasing h. For $\Delta E_0 = E_0(C_0 = 0.04, r_0 = 30) - E_0(0,0)$, the region of the membrane subject to the curvature contributes the most to the ΔE_0 term. Hence, ΔE_0 can be approximated in discrete form as:

$$\Delta E_0 = \sum_{i=1}^{M} \left[\frac{\kappa}{2} \left(\nabla_i^2 z \right)^2 + \frac{\sigma}{2} \left(\nabla_i z \right)^2 \right] h^2, \tag{5.16}$$

where, the summation now is only over the grid-points subject to the curvature field, which is smaller for the larger system size (i.e. system IV) resulting in a smaller value of ΔE_0. The same conclusion can be reached if the step-size, h remains same, while the total number of grid-points, N change. Hence, we expect that, a larger membrane would have a smaller increase in the free energy when subject to a fixed curvature region of size r_0, rationalizing the trend in Fig. 5.4.

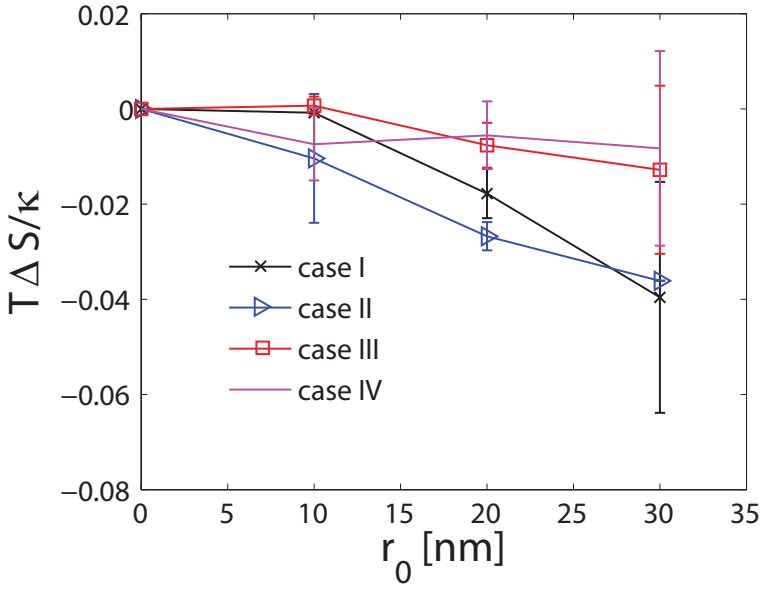

Figure 5.6: Membrane entropy change as a function of r_0.

5.3.2 Quasiharmonic Analysis for a Model Membrane With Non-Zero Curvature

Fourier series has traditionally been the preferred basis set representing the modes of the thermally undulating membrane. In the absence of the H_0 term, the Fourier modes decouple [100] and the Helfrich energy is simply the addition of harmonic contributions from the Fourier coefficients. However, the Fourier coefficients are not the natural basis when the membrane is subject to an intrinsic curvature field, as shown by several researchers [37, 174]. In particular, Wallace [174] and Divet [37] have solved the Helfrich Hamiltonian when the intrinsic curvature is proportional to the membrane concentration of curvature inducing species. In such scenarios, the membrane Hamiltonian involves coupling between the membrane height and membrane composition. In the presence of a heterogeneous curvature field, it is also evident that the Hamiltonian in Eq. 5.2 with non-zero H_0 is not diagonalized in Fourier space (Appendix 5.4.2) due to cross-terms (mode-mixing). This feature is easily appreciated in a 1-dimensional analog to the Helfrich model (choosing $H_0 = C_0\Gamma(x_0/2)$), by expressing the membrane undulation of the form (Appendix 5.4.2):

$$z(x) = \frac{a_0}{2} + \sum_{q=1} a_q \cos(qx) + \sum_{q=1} b_q \sin(qx), \tag{5.17}$$

where, $q = 2\pi m/L$, m is an integer such that $0 < m \leq L/h$, and a_q, b_q are the Fourier coefficients. Differentiating E twice with respect to a_q, we obtain the stiffness (rigidity) associated with the q^{th}

sine mode (Appendix 5.4.2):

$$\frac{\partial^2 E}{\partial a_q^2} = \left[\frac{\kappa L q^4}{2} + \frac{\sigma L q^2}{2}\right] + \frac{\kappa C_0^2 q^2 x_0}{4} - \frac{\kappa C_0^2 q}{4}\sin(q x_0). \tag{5.18}$$

In order to determine whether the dependence of the effective stiffness with x_0, we evaluate

$$\frac{\partial}{\partial x_0}\left(\frac{\partial^2 E}{\partial a_q^2}\right) = \frac{\kappa C_0^2 q^2}{4}\left(1 - \cos(q x_0)\right). \tag{5.19}$$

Since the right-hand side is always positive, the effective stiffness ($\kappa_{\mathrm{renorm},q}$) of every sine mode q increases (or remains constant) with increasing x_0. Differentiating Eq. 5.18 with respect to C_0, we obtain,

$$\frac{\partial}{\partial C_0}\left(\frac{\partial^2 E}{\partial a_q^2}\right) = \frac{\kappa C_0 q}{2}\left(q x_0 - \sin(q x_0)\right). \tag{5.20}$$

Since the function $y - \sin(y)$ is always positive for $y > 0$, the right-hand side is always positive, which indicates that the effective stiffness of the sine mode q increases with increasing C_0. These trends are illustrated in Fig. 5.7: our results show that the membrane stiffness increases (and hence the fluctuations of the membrane and thereby the quasiharmonic entropy decreases) with increasing intrinsic membrane curvature, H_0. This provides the rationale for the similar trend quantifying the loss of entropy with increasing membrane deformation we have computed using the numerical TI calculations in Fig. 5.6. As discussed by Kozlov [90], many previous analyses accounting only for the membrane energy have showed that, in the biologically relevant cases, deformation related forces are repulsive and should in fact prevent, rather than promote, the formation of protein domains. Moreover, Kozlov postulates that the restriction of undulation (i.e. the reduction in quasiharmonic entropy) by curvature inducing proteins could lead to attractive forces favoring the formation of protein domains. We note that for the systems we have explored, we have, for the first time quantified the free energy changes (and the entropic effects) and conclude that even though the contribution of the entropic effects $|T\Delta S|$ to the overall change in the bending free energy is small ($\sim 5\%$), the entropic effects are comparable in magnitude to a few $k_B T$. Hence, as postulated by Kozlov [90] such forces can indeed provide the basis for the formation of protein domains which are ubiquitous in intracellular signaling and trafficking mechanisms.

5.4 Appendix

5.4.1 Change of Reference State

F is the free energy as defined by the partition function :

$$Q = c\int exp\left[-\beta E\right] dr^N, \tag{5.21}$$

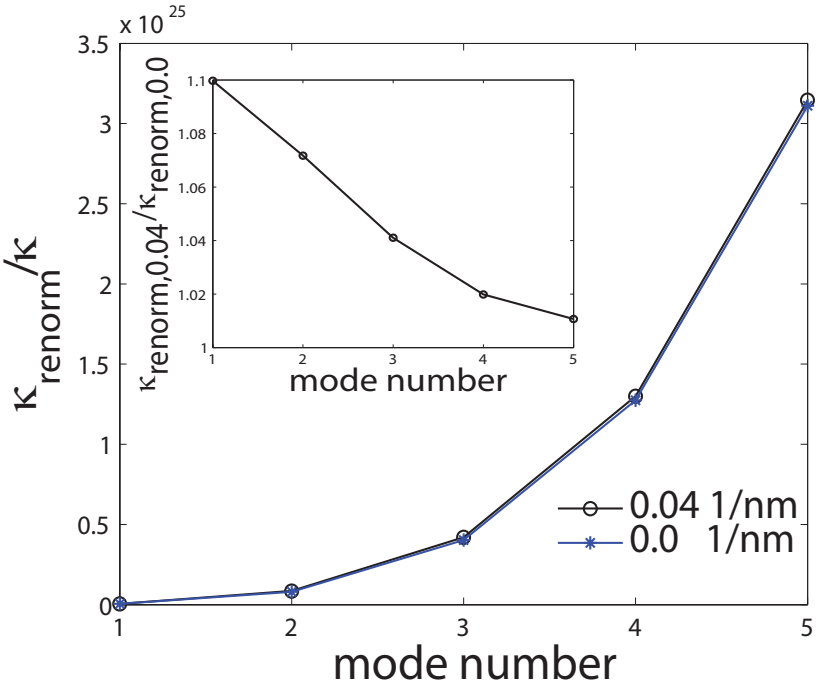

Figure 5.7: Renormalized stiffness associated with the eigenmodes of a one-dimensional model membrane for $C_0 = 0.0$ 1/nm (blue curve) and $C_0 = 0.04$ 1/nm (black curve). We construct a stiffness matrix, K associated with the cosine modes with wave-number, q ranging from $2\pi/L$ to $10\pi/L$; i.e., we have restricted our analysis to first five cosine modes (Appendix 5.4.2. Eigenvalues of this matrix denotes the renormalized stiffness, κ_{renorm} of the system. We plot the κ_{renorm} as a function of mode-number for $C_0 = 0$ and $C_0(x_0/2) = 0.04$ 1/nm where $x_0 = 60$ nm. The inset of depicts the ratio of κ_{renorm} when C_0 =0.04 to κ_{renorm} when C_0 =0.0. In generating these plots, we have employed $L = 250$ nm, $x_0 = 60$ nm and $\sigma = 0$ N/m.

where, the energy is defined in Eq. 5.2. Hence the system entropy can be written as:

$$S = \frac{\langle E \rangle - F}{T}. \tag{5.22}$$

Since we are interested in the deformation free energy with reference to $H_0 = 0$, we define the membrane deformation energy with this reference state as

$$E_0 = \int\int \left[\frac{\kappa}{2}\left(\nabla^2 z\right)^2 + \frac{\sigma}{2}\left(\nabla z\right)^2\right] dxdy. \tag{5.23}$$

Hence, the ensemble average of the deformation energy is given by:

$$\langle E_0 \rangle = \int E_0 e^{-\beta E}\, dr^N. \tag{5.24}$$

$\langle E_0 \rangle$ accounts for the energy required to deform the membrane from a planar state to a curved state and the energy contribution due to thermal fluctuations around a reference state of non-zero H_0. Adding the entropic contributions to $\langle E_0 \rangle$ gives the deformation free energy with respect to non-zero H_0:

$$F_0 = \langle E_0 \rangle - TS. \tag{5.25}$$

Using Eq. 5.22, we get:

$$F_0 = F + \langle E_0 \rangle - \langle E \rangle. \tag{5.26}$$

5.4.2 Fourier Transform of a One Dimensional Analog of the Helfrich Hamiltonian

For the case when $H_0 = 0$, Lin et. al. [100] have shown that the Helfrich Hamiltonian in the Monge gauge (see Eq. 2) can be written as a sum of harmonic terms involving the coefficients of a Fourier series:

$$E = \sum_{\mathbf{q}} \left[\frac{\kappa L q^4}{4} + \frac{\sigma L q^2}{4} \right] (a_q^2 + b_q^2). \tag{5.27}$$

Here, $q = 2\pi m/L$, m is an integer such that $0 < m \leq L/h$, and the coefficients a_q and b_q are defined by the transform (assuming a spatial domain periodic in L) [12],

$$z(x) = \frac{a_0}{2} + \sum_{q=1} a_q \cos(qx) + \sum_{q=1} b_q \sin(qx). \tag{5.28}$$

For $H_0 = 0$, based on Eq. 5.27, the Fourier modes are indeed the independent (eigen) modes, each contributing to a Harmonic term in the total energy. We seek to find a similar Harmonic representation when $H_0 \neq 0$. To analytically represent the stiffness along undulating modes of the of Helfrich Hamiltonian (Eq. 2) within the Monge gauge when $H_0 \neq 0$, we consider a one-dimensional analogue, i.e. $z(x, y) = z(x)$. Since we employ periodic boundary conditions, $z(x)$ is periodic over length L, and hence we expand $z(x)$ in Fourier series [12] as:

$$z(x, y) = z(x) = \frac{a_0}{2} + \sum_{q=1} a_q \cos(qx) + \sum_{q=1} b_q \sin(qx) \tag{5.29}$$

where $q = 2\pi m/L$ and m is an integer greater than zero. The upper limit on the wave-number m is dictated by the number of grid-points, L/h. We also use the orthogonality conditions that for

$m \neq 0$:

$$\int_0^L \sin(2\pi mx/L)\sin(2\pi nx/L)dx = (L/2)\delta_{m,n}, \tag{5.30}$$

$$\int_0^L \cos(2\pi mx/L)\cos(2\pi nx/L)dx = (L/2)\delta_{m,n}. \tag{5.31}$$

$$\int_0^L \sin(2\pi mx/L)\cos(2\pi nx/L)dx = 0. \tag{5.32}$$

The terms $\nabla^2 z$ and ∇z are given by:

$$\nabla^2 z = -\sum a_q q^2 \cos(qx) - \sum b_q q^2 \sin(qx), \tag{5.33}$$

$$\nabla z = -\sum a_q q \sin(qx) + \sum b_q q \cos(qx). \tag{5.34}$$

We substitute the Fourier expansion of $z(x)$ in the following Helfrich Hamiltonian:

$$E = \int_0^L \left[\frac{\kappa}{2}\left(\left(\nabla^2 z\right)^2 - 2\nabla^2 z C_0 \Gamma(x_0/2) + C_0^2\Gamma(x_0/2)\right) + \left(\frac{\kappa C_0^2 \Gamma(x_0/2)}{4} + \frac{\sigma}{2}\right)(\nabla z)^2\right] dx. \tag{5.35}$$

Considering term by term, we get:

$$\begin{aligned}
\int_0^L \frac{\kappa}{2}\left(\nabla^2 z\right)^2 dx &= \frac{\kappa}{2}\int_0^L \left(\sum a_q q^2 \cos(qx) + \sum b_q q^2 \sin(qx)\right)^2 dx \\
&= \frac{\kappa}{2}\int_0^L \left(\sum_q \sum_r a_q a_r q^2 r^2 \cos(qx)\cos(rx)\right) + \left(\sum_q \sum_r a_q b_r q^2 r^2 \cos(qx)\sin(rx)\right) \\
&+ \left(\sum_q \sum b_q b_r q^2 r^2 \sin(qx)\sin(rx)\right) dx,
\end{aligned} \tag{5.36}$$

which using the orthogonlity conditions reduces to:

$$\int_0^L \frac{\kappa}{2}\left(\nabla^2 z\right)^2 dx = \sum_q \frac{\kappa L q^4}{4}\left(a_q^2 + b_q^2\right). \tag{5.37}$$

The next term can be written as:

$$\begin{aligned}
-\kappa C_0 \int_0^L \Gamma(x_0/2)\nabla^2 z dx &= -\kappa C_0 \int_{L/2-x_0/2}^{L/2+x_0/2} \nabla^2 z dx \\
&= \kappa C_0 \int_{L/2-x_0/2}^{L/2+x_0/2} \left(\sum a_q q^2 \cos(qx) + \sum b_q q^2 \sin(qx)\right) dx \\
&= \kappa C_0 \left[\int_{L/2-x_0/2}^{L/2+x_0/2} \sum a_q q^2 \cos(qx)\, dx + \int_{L/2-x_0/2}^{L/2+x_0/2} \sum b_q q^2 \sin(qx)\, dx\right] \\
&= \kappa C_0 \left[\sum a_q q \sin(qx) - \sum b_q q \cos(qx)\right]_{L/2-x_0/2}^{L/2+x_0/2} \\
&= 2\kappa C_0 \left[\sum a_q q \cos(qL/2)\sin(qx_0/2) + b_q q \sin(qL/2)\cos(qx_0/2)\right] \\
&= 2\kappa C_0 \sum a_q q \cos(qL/2)\sin(qx_0/2).
\end{aligned} \tag{5.38}$$

The next term can be written as:

$$\frac{\kappa C_0^2}{4}\int_0^L \Gamma(x_0/2)\left(\nabla z\right)^2 dx = \frac{\kappa C_0^2}{4}\int_{L/2-x_0/2}^{L/2+x_0/2}\left(\nabla z\right)^2 dx$$
$$= \frac{\kappa C_0^2}{4}\int_{L/2-x_0/2}^{L/2+x_0/2}\left(-\sum a_q q\sin(qx)+\sum b_q q\cos(qx)\right)^2 dx. \quad (5.39)$$

We denote above integral by I. To evaluate I, one needs to consider two cases: $q = r$ and $q \neq r$ separately. For $\mathbf{q} = \mathbf{r}$,

$$I = \frac{\kappa C_0^2}{8}\sum_q \left[\left(a_q^2+b_q^2\right)q^2x_0 + \left(-a_q^2+b_q^2\right)q\sin(qx_0)\right]. \quad (5.40)$$

When $\mathbf{q} \neq \mathbf{r}$, we get,

$$I = \frac{\kappa C_0^2}{2}\sum_q\sum_r \frac{qr}{q^2-r^2}\cos(qL/2)\cos(rL/2)$$
$$\times\left\{\sin(qx_0/2)\cos(rx_0/2)\left[ra_qa_r+qb_qb_r\right]-\cos(qx_0/2)\sin(rx_0/2)\left[qa_qa_r+rb_qb_r\right]\right\}. \quad (5.41)$$

Collectively, we can express I as:

$$I = \frac{\kappa C_0^2}{2}\sum_q\sum_r \frac{\delta_{q,r}}{4}\left[\left(a_q^2+b_q^2\right)q^2x_0+\left(-a_q^2+b_q^2\right)q\sin(x_0)\right]+(1-\delta_{q,r})\frac{qr}{q^2-r^2}\cos(qL/2)\cos(rL/2)$$
$$\times\left\{\sin(qx_0/2)\cos(rx_0/2)\left[ra_qa_r+qb_qb_r\right]-\cos(qx_0/2)\sin(rx_0/2)\left[qa_qa_r+rb_qb_r\right]\right\}. \quad (5.42)$$

The last term can be expressed as:

$$\frac{\sigma}{2}\int_0^L\left(\nabla z\right)^2 dx = \frac{\sigma}{2}\int_0^L\left(-\sum a_q q\sin(qx)+\sum b_q q\cos(qx)\right)^2 dx$$
$$= \frac{\sigma}{2}\int_0^L\left(\sum_q\sum_r\left[a_qa_rqr\sin(qx)\sin(rx)-a_qb_rqr\sin(qx)\cos(rx)+b_qb_rqr\cos(qx)\cos(rx)\right]\right)dx, \quad (5.43)$$

which using orthogonality, reduces to:

$$\frac{\sigma}{2}\int_0^L\left(\nabla z\right)^2 dx = \sum_q\frac{\sigma Lq^2}{4}\left(a_q^2+b_q^2\right). \quad (5.44)$$

Hence, we obtain,

$$E = \frac{\kappa}{2}C_0^2x_0+\sum_q\sum_r\delta_{q,r}\left\{\frac{\kappa Lq^4}{4}\left(a_q^2+b_q^2\right)+2\kappa C_0a_qq\cos(qL/2)\sin(qx_0/2)+\frac{\sigma Lq^2}{4}\left(a_q^2+b_q^2\right)\right.$$
$$\left.+\frac{\kappa C_0^2}{8}\left[\left(a_q^2+b_q^2\right)q^2x_0+\left(-a_q^2+b_q^2\right)q\sin(qx_0)\right]\right\}+\frac{\kappa C_0^2}{2}(1-\delta_{q,r})\frac{qr}{q^2-r^2}\cos(qL/2)\cos(rL/2)$$
$$\times\left\{\sin(qx_0/2)\cos(rx_0/2)\left[ra_qa_r+qb_qb_r\right]-\cos(qx_0/2)\sin(rx_0/2)\left[qa_qa_r+rb_qb_r\right]\right\}, \quad (5.45)$$

where, $\delta_{q,r}$ is the Kronecker delta function. From above expression, it becomes clear that the energy contribution from a given Fourier mode is not decoupled from another, since the off-diagonal elements (obtained by setting $q \neq r$) are non-zero. This mode-mixing in Fourier coefficients implies that the Fourier modes are not exactly the eigenmodes of the system, when $H_0 \neq 0$. Moreover, when $H_0 \neq 0$, for a given mode, the energy of the sine (asymmetric about $L/2$) and the cosine (symmetric about $L/2$) modes are not equal to each other, since Eq. 5.45 is not invariant when a_q and b_q are swapped. The Helfrich Hamiltonian is nevertheless harmonic with respect to the Fourier coefficients as shown below. Differentiating E twice with respect to a_q, we obtain the stiffness (rigidity) associated with the q^{th} sine mode:

$$\frac{\partial^2 E}{\partial a_q^2} = \left[\frac{\kappa L q^4}{2} + \frac{\sigma L q^2}{2}\right] + \frac{\kappa C_0^2 q^2 x_0}{4} - \frac{\kappa C_0^2 q}{4}\sin(q x_0). \tag{5.46}$$

In order to determine whether the effective stiffness of mode q increases or decreases with x_0, we differentiate above expression to obtain,

$$\frac{\partial}{\partial x_0}\left(\frac{\partial^2 E}{\partial a_q^2}\right) = \frac{\kappa C_0^2 q^2}{4}\left(1 - \cos(q x_0)\right). \tag{5.47}$$

The right-hand side is always positive, which indicates that the effective stiffness of the sine mode q increases (or remains constant) with x_0. Differentiating Eq. 5.46 with respect to C_0, we obtain,

$$\frac{\partial}{\partial C_0}\left(\frac{\partial^2 E}{\partial a_q^2}\right) = \frac{\kappa C_0 q}{2}\left(q x_0 - \sin(q x_0)\right). \tag{5.48}$$

The right-hand side is always positive which indicates that the effective stiffness of the sine mode q increases with increasing C_0. Differentiating E twice with respect to b_q, we obtain the stiffness of the q^{th} cosine mode:

$$\frac{\partial^2 E}{\partial b_q^2} = \left[\frac{\kappa L q^4}{2} + \frac{\sigma L q^2}{2}\right] + \frac{\kappa C_0^2 q^2 x_0}{4} + \frac{\kappa C_0^2 q}{4}\sin(q x_0). \tag{5.49}$$

Indeed, the cosine (symmetric) and sine (asymmetric) modes have different effective stiffness values when $C_0 \neq 0$, however, the qualitative dependence of the stiffness with changing x_0 and C_0 remain the same.

We also derive the stiffness associated with mixed modes as:

$$\frac{\partial^2 E}{\partial a_q \partial a_r} = \frac{\kappa C_0^2}{2}\frac{qr}{q^2 - r^2}\cos(qL/2)\cos(rL/2)\Big\{r\sin(qx_0/2)\cos(rx_0/2) - q\cos(qx_0/2)\sin(rx_0/2)\Big\}. \tag{5.50}$$

While Eq. 5.46 defines the stiffness of harmonic potential given by Eq. 5.45 to a given cosine mode with wave-number q, Eq. 5.50 defines stiffness to a mixed modes of two cosines with wave-numbers r and q. We note that the stiffness associated with two mixed sine modes of different wave numbers

can be derived using a similar procedure, however the stiffness associated with mixed sine and cosine modes (either $a_r b_q$ or $a_q b_r$) is zero.

Using Eq. 5.46, we construct a stiffness matrix, K for the cosine modes with wave-number, q ranging from $2\pi/L$ to $10\pi/L$. Let K_0 be the stiffness matrix when $C_0 = 0$ and K be the stiffness matrix when $C_0 \neq 0$. We numerically compute the eigenvalues Λ_0, Λ and the eigenmodes v_0, v of the matrices K_0 and K, respectively. The renormalized stiffness, κ_{renorm} is then defined as $\Lambda_i/\Lambda_{0,i}$ where i represent the mode-number and is plotted in Fig. 7. The eigenmode matrix for $C_0 = 0$ in Fourier space is then simply

$$v_0 = \mathbf{I}. \tag{5.51}$$

For $C_0 \neq 0$, in Fourier space we get (where the parameters used are listed in Fig. 7):

$$v = \begin{bmatrix} 0.99994 & -0.0104 & 0.0033824 & -0.0011722 & 0.00031768 \\ 0.010452 & 0.99983 & -0.014253 & 0.0044099 & -0.0012582 \\ -0.0032468 & 0.014339 & 0.99983 & -0.010997 & 0.0029615 \\ 0.0010924 & -0.0042723 & 0.011083 & 0.99991 & -0.0068943 \\ -0.00028737 & 0.0011894 & -0.0029036 & 0.0069323 & 0.99997 \end{bmatrix}. \tag{5.52}$$

Here, the columns of above matrices represent the eigenmodes of the system. The angle θ_{proj} is then defined as the angle between the column vector of v_0 with the corresponding column vector of v. We also obtain the eigenmodes in Cartesian space by multiplying the above matrices by following transformation matrix, T.

$$T = \begin{bmatrix} cos(2\pi x/L) \\ cos(4\pi x/L) \\ cos(6\pi x/L) \\ cos(8\pi x/L) \\ cos(10\pi x/L) \end{bmatrix} \tag{5.53}$$

We denote the eigenmode matrices in Cartesian space as v_0^c and v^c for $C_0 = 0$ and $C_0 \neq 0$, respectively. In order to quantify the degree of mode-mixing when C_0 is non-zero, we calculate the angle θ_{proj} between each eigenmode of the system and the eigenmode of a related system with $C_0 = 0$. In Fig. 5.8 we plot these angles when $C_0(x_0/2) = 0.04$ 1/nm with $x_0 = 60$ nm, which signify the degree of mixing among different Fourier modes. We note that an angle of zero represents a pure mode, i.e. Fourier modes of the system being the same as its eigenmodes. In Fig. 5.9, we plot the difference in the membrane deformation (in Cartesian representation) when the membrane fluctuates by a unit amount along the corresponding eigenmodes for the $C_0 \neq 0$ case and the $C_0 = 0$ case; these plots quantify the degree of mode mixing due to curvature field.

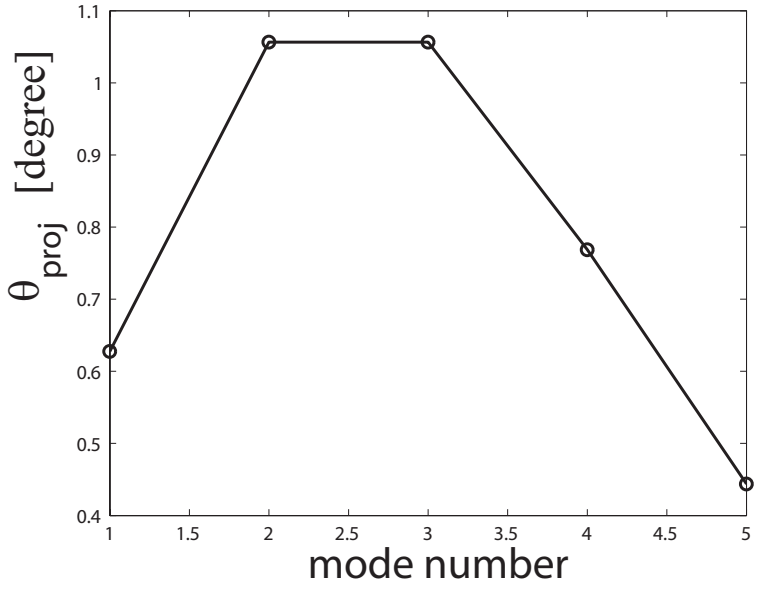

Figure 5.8: Angle between the eigenmode of a curvature-induced membrane and the corresponding mode of a membrane under zero intrinsic curvature. In generating these plots, we have employed $L = 250$ nm, $x_0 = 60$ nm and $\sigma = 0$ N/m.

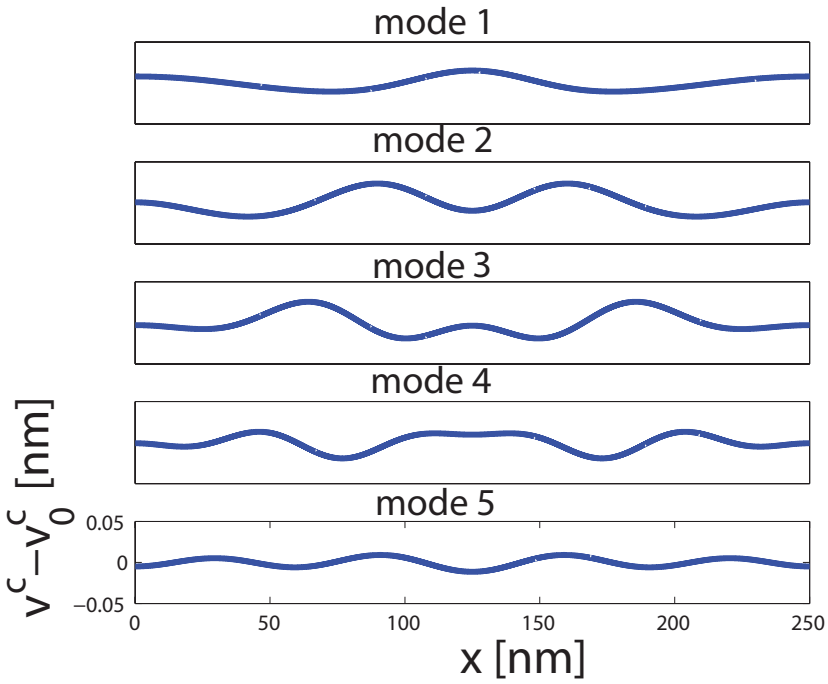

Figure 5.9: Membrane height difference for a unit displacement along each eigenmode v_0^c and v^c.

Chapter 6

Nanocarrier-Cell Adhesion Investigated using a Thermodynamic Model and Monte Carlo Simulations

6.1 Introduction

Targeted drug delivery using functionalized nanocarriers offers many benefits lacking in conventional drug delivery systems, among which are improved efficacy and reduced toxicity [84]. Of many available technologies, targeting of therapeutic agents to the endothelial cells via specific receptor-mediated adhesion (such as through intercellular adhesion molecule-1 or ICAM-1), leads to enrichment of specificity [118, 149].

Several models have been proposed for the treatment of receptor-mediated adhesion of cells [17], [18, 19, 69]. These models typically include the effects of receptor-ligand interaction strength, receptor and ligand densities, arrest/mobility of receptors/ligands on their respective surfaces, effects of membrane-mediated adhesion, etc., and have been successfully applied to neutrophil adhesion under uniform shear flow conditions [19]. Pioneering work by Bell [17, 18] on cell-cell adhesion laid the basic framework for much of the subsequent work in this field. In the Bell model, the specific attraction due to receptor-ligand bond formation is considered as a function of bond-length. Subsequent work by Hammer [19, 44, 69] on the simulation of the adhesive behavior of neutrophil (treated

as rigid spheres), with randomly distributed receptors, in near contact with a planar endothelium under shear flow, identified several regimes of rolling and arrest behavior of neutrophil and delineated a state diagram. Following this body of work, we focus here on developing a physically-based coarse-grained model for accurate in silico predictions of functionalized nanocarriers binding to endothelial cells cultured in vitro. We propose a viable procedure for integrating a large number of system parameters that affect the binding process including the effect of the endothelial glycocalyx layer representing a thermodynamic barrier to the nanocarrier adhesion, which thus far, has not been considered in prior works.

Glycocalyx is a carbohydrate-rich zone on the cell exterior, mainly consisting of glycoproteins and proteoglycans [133, 146]. Its presence on the endothelial cell surface has been shown to have an effect on the binding of nanocarriers. Although models are available to represent mechanical properties of glycocalyx [28, 178], to our knowledge, a thermodynamic model which quantitatively predicts the effect of glycocalyx on nanocarrier binding is not available. However, in vivo experimental data of Mulivor [116] strongly suggests that the (partial) removal of glycocalyx by enzymatic (heparinase-mediated) degradation strongly influences nanocarrier binding [116]. In this study, the authors infused the femoral vein of rat with a rat anti-ICAM-1 functionalized nanocarrier solution. To mimic the effect of glycocalyx removal, the venules were perfused with the heparinase enzyme solution. The authors recorded the transient number of bound nanocarriers using fluorescence microscopy in presence and absence of glycocalyx and observed that the removal of glycocalyx increases the number of bound nanocarriers by at least two-fold (see Fig. 6.2). These studies highlight the importance of considering the contributions of the glycocalyx layer in constructing an accurate model for nanocarrier binding.

In this work, we consider three physical parameters, namely, glycocalyx resistance, flexural rigidity of receptors, and receptor-ligand bond-stiffness, in mediating nanocarrier adhesion to endothelial cells and strive to construct a microscopic model capturing these important physical characteristics (see our schematic in Fig. 6.1). We develop rigorous procedures to estimate the parameter values of our model using independent experimental results reported in the literature, thus adopting a zero-fit approach. We then subject our model and simulation results to a rigorous test by comparing the predicted theoretical results with experimental results reported recently by Muro et. al. for the nanocarrier binding affinity to endothelial cells [117]. These authors investigated anti-ICAM (R6.5) functionalized polystyrene nanocarriers binding to HUVEC (human umbilical vein endothelial cells) at 4 ^{0}C under the conditions of cell fixation as well as stimulation by TNF-α. Finally, we provide results for parameter sensitivity in order to assess the role and importance of some key physical model parameters in governing the nanocarrier binding characteristics.

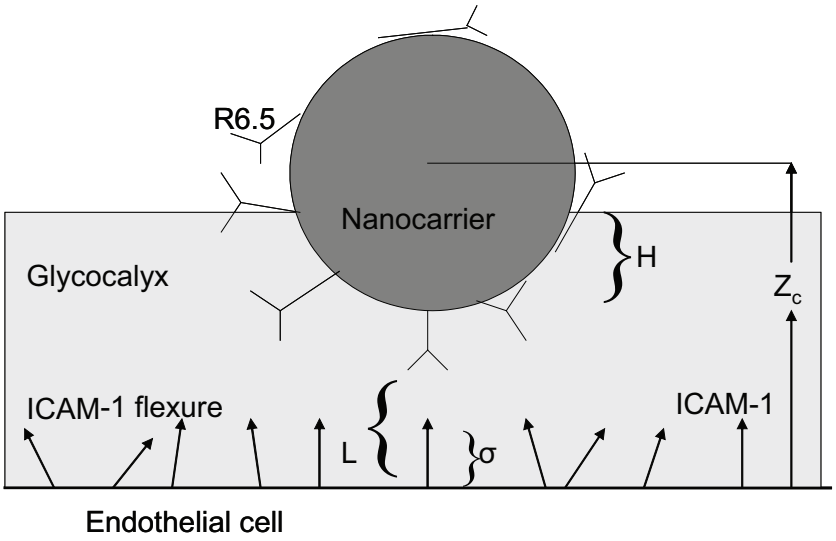

Figure 6.1: Schematic of the microscopic model for nanocarrier binding to endothelial cells.

6.2 Models and Methods

6.2.1 Models

A schematic of our microscopic model for nanocarrier binding to endothelial cell is depicted in Fig. 6.1. The largest length-scale considered in our model is that of the cell surface ($\approx \mu m$). In contrast, the relevant length-scale for interaction between proteins and ligands is 10 nm. The 2-orders of magnitude separation in length-scale forbids us to employ an atomistically detailed description for our system and warrants the use of coarse-grained models and simplifying assumptions. Following the work of Hammer et. al. [44, 69], we approximate the confluent endothelial cell surface by a planar non-deformable surface (a possible procedure for relaxing this assumption is given in section 6.5), while the polystyrene nanocarriers employed in the experiments of Muro [117] are modeled as rigid (hard) spheres. The nanocarrier is functionalized using antibodies specific to target antigens on the cell surface. Specifically, we consider the R6.5 antibody specific for ICAM-1 antigens in order to compare our model predictions with experiments [117] performed on the same system. In our model, the antibodies are distributed randomly, i.e. in random orientation at random positions, consistent with the experimental hydrophobic association protocol of Muro et al. [117] used to functionalize the nanocarrier surface (see Fig. 6.1). The antigens are in a vertical orientation (i.e. perpendicular to the cell surface) in their minimum energy configuration when unbound, and distributed randomly on the planar cell surface. Antigen flexure about this minimum energy configuration is also accounted for in our model, (see below).

parameter	value	ref
simulation cell area	1 μm^2	
simulation cell height	0.5 μm	
nanocarrier diameter	100 nm	
antingen length	19 nm	[88]
antibody length	15 nm	
antigen/antibody radius	1.5 nm	
no. of antibodies per nanocarrier	220	[117]
$\Delta G(\sigma)$	-7.98 $\times$ 10^{-20} J	[117]
bond spring constant	1000 dyn/cm	[185]
glycocalyx height	100 nm	[165]
glycocalyx spring constant	3.9 $\times$ 10^9 J/m^4	[116]
antigen flexural rigidity	700 pN-nm^2	

Table 6.1: System Parameters.

Antigen-Antibody Interaction

In our model, the antigen-antibody bond-energy depends on the bond-length as well as the bond-orientation. For the dependence of reaction free energy on the bond-length, the Bell model [18] is employed, according to which the binding free energy ΔG is a quadratic function of the bond-length L with a minimum at the equilibrium value of the bond length σ, i.e.

$$\Delta G(L) = \Delta G(\sigma) + \frac{1}{2}k(L-\sigma)^2. \tag{6.1}$$

Here, $\Delta G(\sigma)$ is the free energy of the reaction when the bond is at the equilibrium separation, σ. $\Delta G(L)$ is the free energy of reaction at bond length L, and k is the bond stiffness constant or bond spring constant.

Antigen Flexure

Flexure of antigens from their equilibrium upright position on the cell surface leads to an orientational dependence of the bond-energy. Considering small flexures, we model each antigen as a cantilever, and thus its contribution to the bond-energy ΔG due to flexure is equal to $(2EI/L^3)y_L^2$ (see 6.6.1), where y_L is the difference in the vertical distance of the tip of the bent antigen and that of an upright antigen, EI is the flexural rigidity (defined as the product of the Young's modulus E and the moment of inertia I), and L is the length of the antigen. Antibody flexure is not considered

in our model.

Weinbaum et. al. [178] estimate the flexural rigidity EI for a glycoprotein to be 700 pN-nm^2, i.e. 7×10^{-28} N-m^2. By using this value for EI along with the length of ICAM-1 (L=19 nm 15 inferred from electron microscopic study), we calculated the bending energy for ICAM-1 for small deflections: $U(y_L) = 2EI/L^3 y_L^2 = 2.04 \times 10^{-4} y_L^2$, where $U(y_L)$ is in joule and is y_L in meter; y_L is the distance of the tip from its equilibrium position.

Glycocalyx Resistance

As the nanocarrier approaches the cell surface, it encounters resistance due to the presence of the glycocalyx layer (see Fig. 6.1). Based on the biophysical characterization data of Squire et al. [165], we assume a height of 100 nm for the glycocalyx layer. The resistance offered by the glycocalyx layer, in general, comprises of a combination of osmotic pressure (desolvation or squeezing out of water), electrostatic repulsion, steric repulsion between the nanocarrier and the glycoprotein chains of the glycocalyx, and entropic forces due to conformational restrictions imposed on the confined glycoprotein chains. We lump these effects into a single term of mechanical resistance due to glycocalyx by assuming a harmonic potential of the form $1/2 k_{glyx} H^2$ per unit differential area, where H is the penetration depth of the nanocarrier into the glycocalyx. Here, k_{glyx} can be regarded as an effective stiffness constant per unit area that effectively incorporates the molecular interactions described above. This additional resistance enters into thermodynamic considerations in calculating the Gibbs free energy change of binding. Specifically, for the binding of the nanocarrier to the cell, we get:

$$\Delta G(H) = \Delta G(0) + \int \int \frac{1}{2} k_{glyx} H^2 dA, \tag{6.2}$$

where, $\Delta G(0)$ is the free energy of the system when no glycocalyx is present on endothelial cells, and the integration is over the area of nanocarrier that is immersed in glycocalyx.

6.2.2 Parameter Estimation

Based on the experiments of Muro [117] for free R6.5 (antibody) binding to free ICAM-1, $\Delta G(\sigma)$ is estimated to be -7.9×10^{-20} J/molecule at 4 ^{0}C. Consistent with the reported trend from the investigation of the temperature effects on the thermodynamic interaction between hen egg white lysozyme and Fab D1.3 antibody in a solvated environment for the temperature range 278 to 313 K by Zeder-Lutz [183], we assume that $\Delta G(\sigma)$ of the reaction is temperature-independent. In our model, the bond-spring constant k, and the equilibrium bond length σ, are also taken to be temperature independent (see section 6.4.3 for further comment on these assumptions). We calculate k_{glyx}

based on the in vivo experimental data of Mulivor (described in the introduction) [116]: assuming that the nanocarrier binding is a second order reaction with respect to free nanocarriers and free antigens, and unbinding is a first order reaction for the bound-complex, we have shown in section 6.6.2 that the concentration of bound nanocarriers as a function of time, $C(t)$, is given by:

$$C(t) = \frac{k_f B C_{max}}{(k_f B + k_r)} \times (1 - \exp[t(k_f B + k_r)]) \,. \tag{6.3}$$

Here, k_f and k_r are the forward and reverse rate constants, respectively, B is the concentration of free nanocarriers in solution, and C_{max} is the maximum concentration of nanocarriers that can bind to the cell-surface. By importing the values of B and C_{max} from the experiments of Mulivor et al., we regress k_f and k_r to fit the expression in Eq. 6.3 to the experimental data in Ref. [116], both in the presence of and in the absence of the glycocalyx, (see Fig. 6.2 and 6.6.2). Using the inferred values of k_f and k_r, we compute the equilibrium constant K in the presence and in the absence of glycocalyx. The difference between $k_B T \ln K$ in the presence and absence of glycocalyx yields the change in the reaction free energy due to glycocalyx, i.e., $\Delta G(H) - \Delta G(0)$, in Eq. 6.2. The value of the glycocalyx spring constant k_{glyx} (reported in Table 6.1) is then determined from Eq. 6.2, see also section 6.6.2. Following Evans and Ritchie [46], we derive the dependence of the

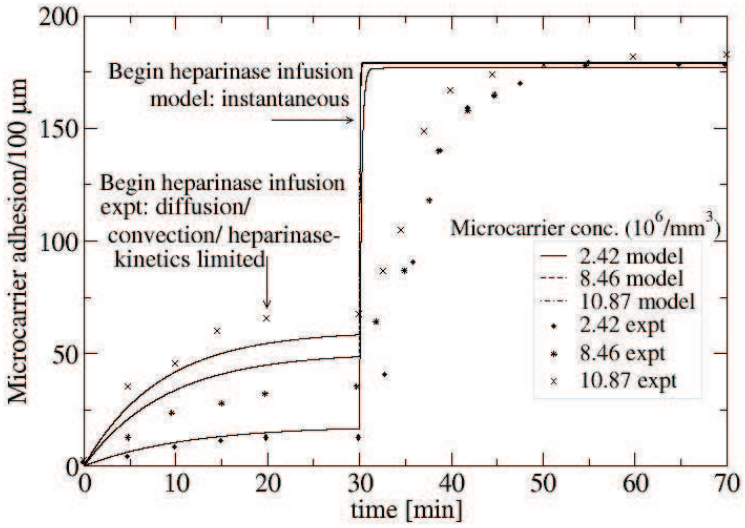

Figure 6.2: Regression of the glycocalyx model (Eq. 6.3, and Eq. 6.7) to the experimental data of Mulivor [116] provides an avenue to estimate the glycocalyx sprint constant k_{glyx} reported in Table 6.1.

antigen-antibody bond rupture force f (described by the Bell model [18]) on force-loading rate r_f as given by:

$$\frac{f \times r_f}{k_B T} = k k^0 exp[f^2/(2k)], \tag{6.4}$$

where, k^0 is the unstressed bond-dissociation rate and k is the bond-spring constant. Fitting the above expression to the force-spectroscopy data of Moy et. al. [185] gives k^0 and k, (see section 6.6.3).

6.3 Monte Carlo Protocol

A stochastic scheme based on the Metropolis Monte Carlo method [9] is developed for simulating the antibody (R6.5) functionalized nanocarrier binding to endothelial cells expressing antigens (ICAM-1) on the surface based on our model depicted in Fig. 6.1. Periodic boundary conditions are enforced along the cell surface and impenetrable boundaries are enforced in a direction normal to the cell surface. The choice of boundary conditions is chosen for computational convenience and is not expected to impact the results with any significance. A summary of the system parameters is provided in Table 6.1.

Steric interactions between nanocarriers and antigens are considered through hardcore potentials (i.e., they are treated as hardspheres and hardrods, respectively). This simplifies our treatment of multicarrier simulations without introducing any significant artifacts because the density of nanocarriers and of the surface antigens are still significantly low and surface coverages we explore in our simulations (and in the experiments) are very much in the dilute limit so that interparticle interactions are not important. Still, it may be worthwhile to investigate the sensitivity of our results to the short-range potential of protein-protein interaction. This can be accomplished by calculating the potential of mean force between two membrane-bound antigens using atomistic or coarse-grained molecular dynamics simulations and to incorporate the effects of van der Waals, electrostatics, and hydrogen bond interactions, explicitly.

During each step of the Monte Carlo simulation, (which is based on the Metropolis algorithm [9]), one of the following actions are attempted to generate new system configurations for the nanocarrier or the surface antigen: a nanocarrier is randomly selected and it either rotated or translated by a randomly chosen extent along a randomly chosen direction. If antigen diffusion is allowed in our model, then a randomly selected antigen is translated (on the cell-surface) by a random extent. The new system configuration is accepted with a probability: $\min[1, \exp(-(U_{new} - U_{old})/k_B T)]$, where k_B is the Boltzmann constant, T is the temperature in Kelvin scale, U_{new} and U_{old} are the potential energies of the new and old configurations, respectively, and the min operator selects

minimum of the two values. The energy, U arises due to the hardsphere potential term or the glycocalyx resistance term. Whenever an antibody reaches within the bonding distance of an antigen, an additional step of bond-formation or bond-breakage is considered. A bond is formed between a randomly selected antigen and antibody within the bonding distance with a probability: $\min[1, \exp(-\Delta G/k_B T)]$. If the selected antigen and antibody pair is already bonded, then the bond is broken with a probability: $\min[1, \exp(\Delta G/k_B T)]$, where, ΔG is the change in energy due to formation of bond at given length and orientation. These calculations are performed 500 million times to ensure that properties such as total energy and multivalency converge. The results are reported here as an average over four independent simulations, each with 0.5 billion Monte Carlo steps. The error bars are reported as the standard deviation resulting from the four independent simulation runs.

6.4 Results

6.4.1 Model Predictions and Comparison with Experiment

We perform simulations of nanocarrier adhesion to endothelial cells to make contact with the experimental work of Muro et. al. [117]. Consistent with their report, we choose the antigen density value of 1.6×10^6 antigens per endothelial cell. However, in converting this value to surface density of antigens in units of antigens/μm^2, we consider the uncertainty in the reported endothelial cell surface-area [104], namely, 800 to 2500 μm^2 per cell. We present our results for the two extreme values of the resulting antigen surface densities: 2000 and 640 antigens/μm^2.

Our results from simulations performed at 4^0C for the case of the antigens not allowed to diffuse on the cell surface (to mimic the scenario in fixed cells) are reported in Table 6.2 in which the multivalency calculated as the average number of antigen-antibody bonds formed per bound nanocarrier and the average binding energy of the nanocarrier binding are reported. For the range antigen and antibody densities we consider there is on an average two bonds per attached nanocarrier. However, owing to the bond-stretching the (negative) binding free energy of the nanocarrier (-14.5 to -16.7 kcal/mol) is considerably greater than -23 kcal/mol, which is twice the equilibrium binding free energy of the antigen-antibody interaction, (see Table 6.1). Using a Scatchard analysis of the experimental binding data [117], Muro et al. report an equilibrium dissociation constant K_D=77 pM for nanocarrier adhesion. This experimentally determined value of the binding affinity amounts to an equilibrium binding free energy of ΔG= -12.82 kcal/mol, here we have used the relationship, $K_D = \exp(\Delta G/k_B T)$. Considering that our modeling results of the binding energy are obtained without direct fitting to nanocarrier binding data, we conclude that

the agreement between simulations Table (6.2) and experiment (-12.82 kcal/mol) is very favorable.

antigens/μm^2	multivalency	binding energy (kcal/mol)
640	1.85 $\pm$ 0.1	-14.57 $\pm$ 0.72
2000	2.05 $\pm$ 0.1	-16.75 $\pm$ 0.34

Table 6.2: Binding of Nanocarriers to Nondiffusing ICAM-1 on the Endothelial Cell Surface: Model Predictions

In order to consider the effect of surface diffusion of antigens on nanocarrier binding, we also performed simulations allowing the antigens to diffuse (Table 6.3). Not surprisingly, we find that

antigens/μm^2	multivalency	binding energy (kcal/mol)
640	2.65 $\pm$ 0.4	-24.16 $\pm$ 3.22
2000	2.4 $\pm$ 0.2	-21.82 $\pm$ 2.42

Table 6.3: Binding of Nanocarriers to Diffusing ICAM-1 on the Endothelial Cell Surface: Model Predictions

allowing the surface antigens to diffuse in our simulations leads to increases in the multivalency as well as the binding affinity (i.e., a corresponding decrease in the negative binding energy) of nanocarrier binding, see Figs. 6.3 and 6.4.

In order to further establish the relationship between diffusing surface antigens and enhanced multivalency/binding energy, we map the in-plane 2-dimensional radial distribution function [9] related to the spatial distribution of surface antigens in our simulations in Fig. 6.5. The radial distribution function is defined as the probability of finding two antigens at a given separation relative to the same probability if the antigens were completely randomly distributed. At a given separation, the radial distribution function value of greater than one indicates clustering of antigens at that separation. As evident from Fig. 6.5, the ICAM-1 antigens cluster within a separation of 50 nm, which corresponds to the size (radius) of the nanocarriers. Moreover, as evident from the comparison of the radial distribution function plots in the presence and absence of the nanocarrier, the ICAM-1 clustering is clearly mediated by nanocarrier adhesion. These observations establish that the enhancement of multivalency and reduction of binding energy associated with the bound nanocarrier due to the diffusion of surface antigens is clearly mediated by antigen clustering.

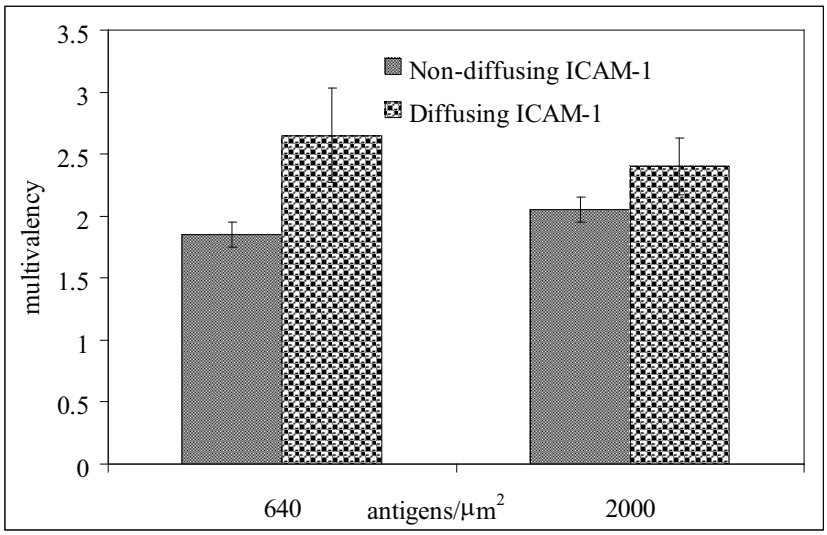

Figure 6.3: Effect of ICAM-1 diffusion on nanocarrier multivalency: a visual comparison of data from Tables 6.2 and 6.3.

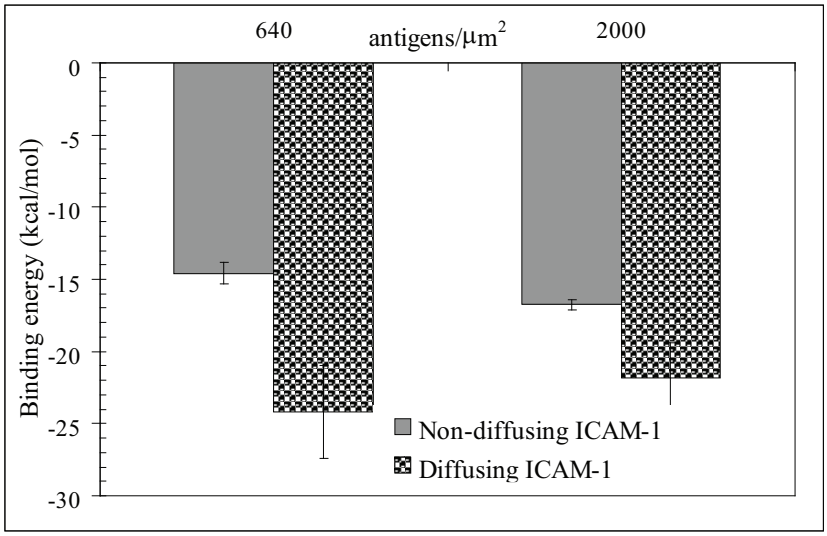

Figure 6.4: Effect of ICAM-1 diffusion on nanocarrier binding energy: a visual comparison of data from Tables 6.2 and 6.3.

6.4.2 Parameter Sensitivity to Model Predictions

In order to dissect the effect/sensitivity of the various physical components in our model on the binding characteristics of nanocarriers, we have performed additional simulations by varying key parameters, namely the bond stiffness constant and the flexural rigidity, over a range of 3 orders

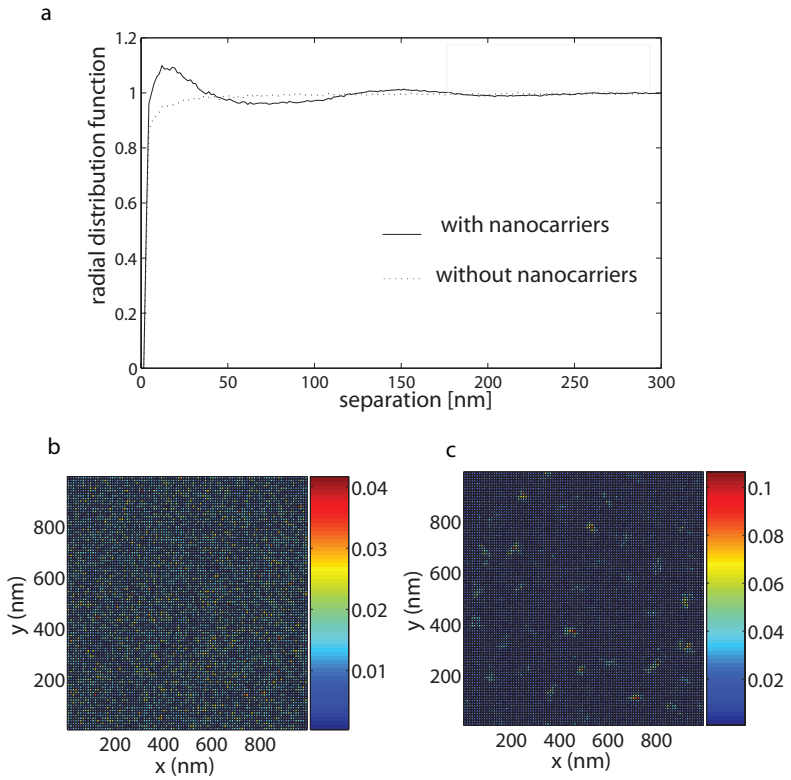

Figure 6.5: (a) Radial distribution function of diffusing antigens on the cell surface in the presence (solid line) and absence (dotted line) of bound nanocarriers. Simulations are performed with 640 antigens/μm^2 and 50 nanocarriers at 40 ^{0}C. (b) Percentage of probability of spatial occupancy of surface antigens in the absence of bound nanocarriers. (c) Percentage of probability of spatial occupancy of surface antigens in the presence of bound nanocarriers. A visual comparison of (b) and (c) clearly indicates clustering of antigens only in the presence of bound nanocarriers.

of magnitude. We report our results of this sensitivity analysis both in the presence and in the absence of glycocalyx in Figs. 6.6 and 6.7. The effect of increasing the bond-stiffness constant (Fig. 6.6) is to decrease the multivalency and increase the (negative) binding energy of nanocarriers (at a rate that is steeper than a linear dependence). The presence of glycocalyx does not affect the multivalency but increases the binding energy. Interestingly, the difference in binding energy with and without glycocalyx is constant for all values of the bond-stiffness constants explored. The effect of varying the flexural rigidity on the multivalency and binding energy is similar to that we observe for the effect of the bond-stiffness constant (compare Figs. 6.6 and 6.7): i.e., multivalency decreases and binding energy increases with increasing flexural rigidity and the presence of glycocalyx does not affect the multivalency but increases the binding energy for each value of the flexural rigidity.

Again, the difference in the binding energy in the absence and presence of the glycocalyx is constant to a statistical significance for all values of the flexural rigidity we have explored. The dependence of the binding characteristics on the two parameters (namely the bond-stiffness constant and the flexural rigidity) we have uncovered provides new insight into the molecular parameters governing nanocarrier binding and establishes that these parameters act independently of the glycocalyx in mediating the binding equilibrium.

6.4.3 Role of Glycocalyx in Mediating Temperature Effects of Nanocarrier Binding

At equilibrium, the change in the Gibbs free energy of a process is related to its dissociation constant by the relationship, $\Delta G = RT \ln K_D$. In our model (see section 6.2.2 for a rationale), ΔG is temperature independent (we note that in traditional thermochemistry of gas and aqueous phase reactions, we substitute $\Delta G = \Delta H - T\Delta S$ and assume that ΔH and ΔS are temperature independent, to get $d/dT \ln K_D = -\Delta H/RT^2$. However, in biomolecular reactions, these assumptions may not be generally valid due to a coupling of conformational and chemical degrees of freedom, and due to competing solvation and hydrophobic effects.); hence,

$$\frac{d}{dT} \ln K_D = -\frac{\Delta G}{RT^2} \tag{6.5}$$

This expression indicates that the magnitude and sign of ΔG determines the dependence of $\ln K_D$ with temperature. Since ΔG is usually a negative quantity for receptor-ligand interactions (with the exception of some active processes requiring metabolism 22), the binding decreases with increasing temperature. In the mean-field limit (approximation) [26] for binding of nanocarriers, the overall free energy change can be represented as additive contributions of several terms: $\Delta G = \Delta G_{bonding} + \Delta G_{glyx} + \Delta G_{flex}$, where ΔG is the overall change in the free energy of the process, $\Delta G_{bonding}$ is change in free energy due to antigen-antibody bond-formation, ΔG_{glyx} is the free energy required to overcome glycocalyx resistance and ΔG_{flex} is the free energy contribution due to antigen flexure. Note that ΔG_{glyx} is positive, while $\Delta G_{bonding}$ is negative. Hence, the presence of glycocalyx is expected to alter the temperature dependence of the equilibrium dissociation constant for binding, K_D. That is, the temperature dependence of binding of nanocarriers to cells depends not only on the free antigen-antibody binding free energy, but also on endothermic terms such as the glycocalyx resistance (and perhaps the antigen flexural rigidity).

By carrying out simulations of binding at different T, we observe the expected effect of increase in the equilibrium dissociation constant with increase in temperature (Table 6.4). Intriguingly, we predict that this increase in the equilibrium dissociation constant of the nanocarrier with increase in

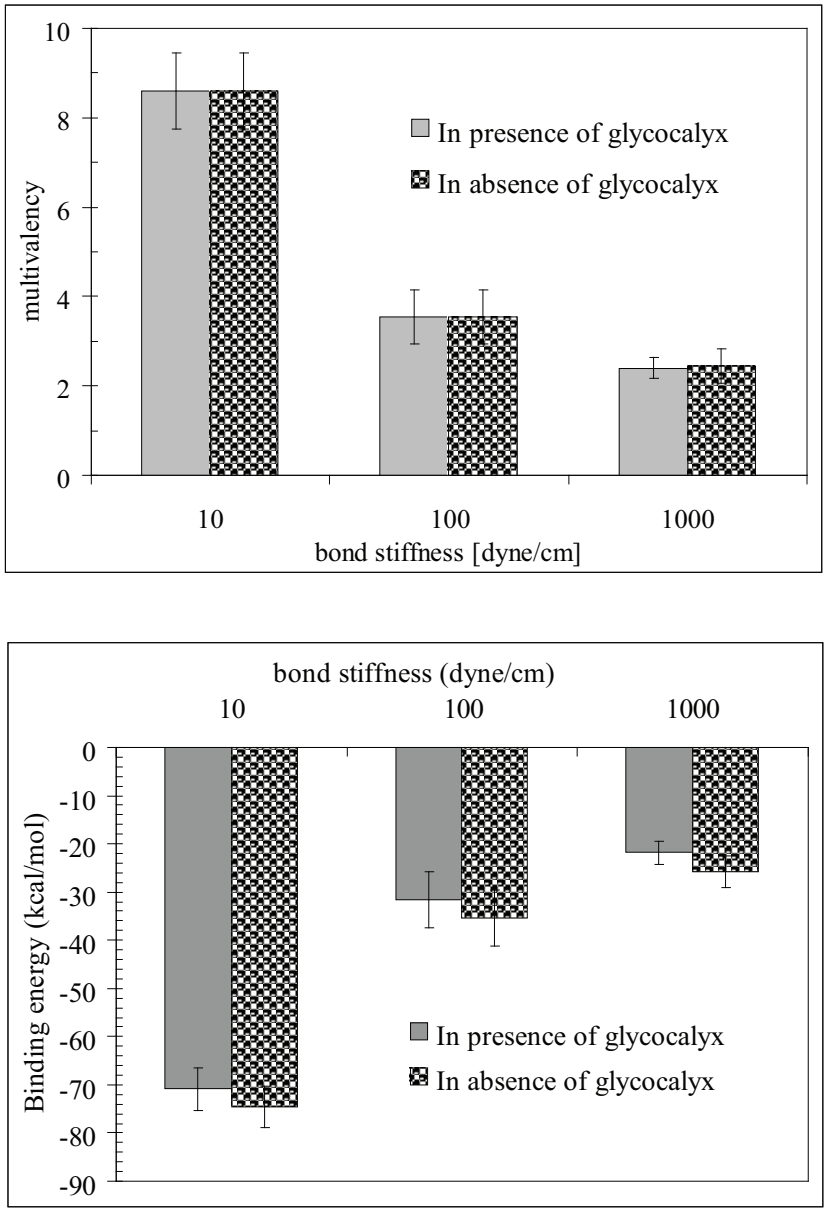

Figure 6.6: Effect of bond-stiffness (k) on nanocarrier (a) multivalency, and (b) binding energy for diffusing ICAM-1. Presence of glycocalyx does not affect the multivalency, though it increases the (negative) binding energy. Simulations are performed for 2000 antigens /μm^2.

temperature gets smaller with increase in glycocalyx resistance (see Table 6.4 and Fig. 6.8). However, with respect to quantitatively capturing the temperature dependence in our model, we issue the following cautionary note: even though, we have developed rational procedures for estimating the key parameters of our model there is in general a need for more characterizing biophysical

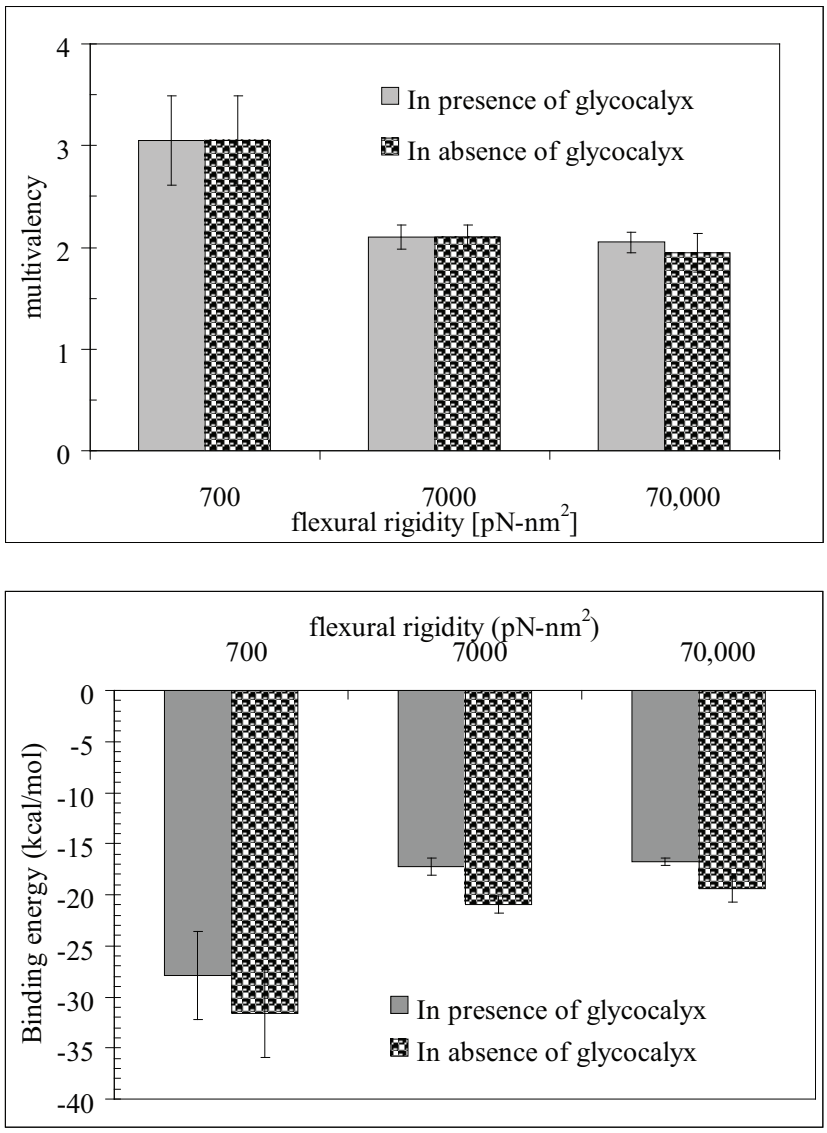

Figure 6.7: Effect of ICAM-1 flexural rigidity on nanocarrier (a) multivalency and (b) binding energy for non-diffusing ICAM-1. Presence of glycocalyx does not affect the multivalency, though it increases the (negative) binding energy. Simulations are performed for 2000 antigens /μm^2.

experiments to relieve the additional assumptions we have made, especially with respect to temperature dependence. For example, in our current model, the receptor-ligand complex bond spring constant is assumed to be temperature independent due to the lack of any supporting experimental data. Single molecule AFM experiments conducted over a limited temperature range suggests temperature softening of proteins [152], however, similar studies on protein-protein complexes are

glycocalyx spring constant (J/m^4)	$\ln K_D^{4^0C}$	$\ln K_D^{37^0C}$	$\ln\left(K_D^{37^0C}/K_D^{4^0C}\right)$
0	-94.4 ± 3.5	-87.8 ± 0.9	6.5
3.9×10^9	-87.74 ± 3.6	-81.8 ± 0.9	5.9
1.0×10^{10}	-77.34 ± 3.6	-72.5 ± 0.9	4.8

Table 6.4: Effect of Glycocalyx on the Nanocarrier Dissociation Constant. Values are reported for diffusing ICAM-1 and with flexural rigidity of 7 pN-nm^2.

not yet available. In the future, such experiments would furbish the requisite temperature corrections to the bond-spring constant. Similarly, there is a growing need for independent characterizing biophysical experiments on antigen flexure and glycocalyx resistance for a enhancing the accuracy predictions relating to temperature effects.

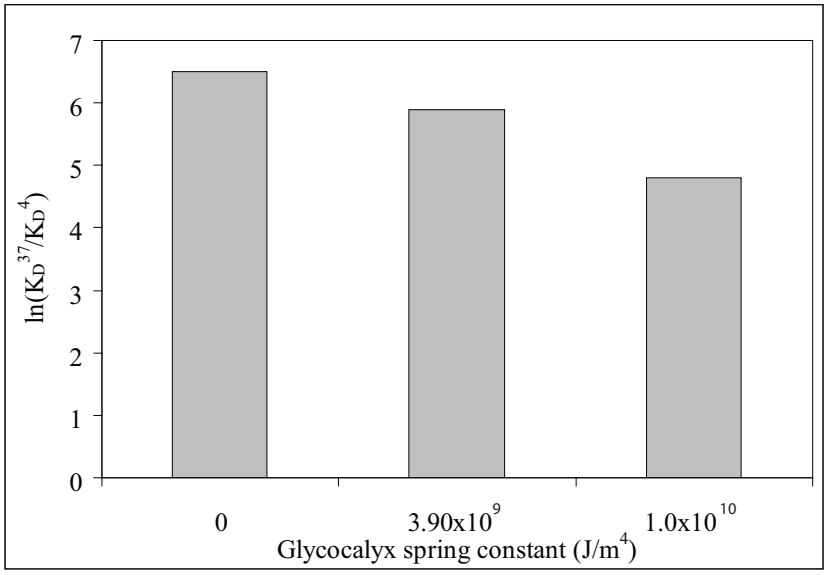

Figure 6.8: Difference of $\ln K_D$ of binding at 37 ^{0}C and 4 ^{0}C plotted against the glycocalyx spring constant k_{glyx}. The difference between $\ln K_D$ at 37 ^{0}C and 4 ^{0}C decreases with increasing glycocalyx resistance, thus reducing the temperature dependence of the binding process.

6.5 Discussion and Conclusions

We describe an equilibrium model (Fig. 6.1) for quantifying the effect of glycocalyx in mediating the interaction of functionalized nanocarriers with endothelial cells. Rather than fitting model parameters to reproduce experimental binding data of nanocarriers to cells, we have described several new

strategies (sections 6.6.1, 6.6.2, 6.6.3, Fig. 6.2, and Table 6.7) for a rational parameter estimation based on independent (single molecule and cell-based) characterizing experiments reported in the literature. This rational approach enables us to not only predict experimental binding constants of nanocarriers to endothelial cells without directly fitting to the binding data (Figs. 6.3, 6.4, 6.6, 6.7 and Tables 6.3, 6.4), but also enables us to transfer the parameter values across similar systems.

We have shown that we can quantitatively reproduce the experimental binding affinities in a regime where the multivalency of nanocarrier is small ($\approx$2). The favorable agreement between simulations and experiment also validates our simplifying assumptions, however, we note that experiments under which high multivalency of nanocarriers (e.g., by increasing antibody density on the nanocarrier surface, or by replacing rigid nanocarriers by filomicelles) would provide a more rigorous test for our model assumptions, for a recent review, see Kane [82]. Our simulations provide quantitative descriptions for the multivalency in nanocarrier binding (Figs. 6.3, 6.6, 6.7), as well as for the degree of clustering of antigens (Fig. 6.5). Such a clustering of antigens is also suggested based on indirect inferences by Muro et. al. [119] in their experiments of nanocarrier adhesion to live endothelial cells. A more direct experimental validation of the clustering of ICAM-1 may be obtained via fluorescent labeling and fluorescence microscopy. Our study also identifies two interesting parameters (see further discussion below): glycocalyx resistance and antigen flexural rigidity, both of which reduce binding of nanocarriers and alter the sensitivity of the nanocarrier binding constant to changes in temperature. Both these parameters are physical and can be controlled experimentally: properties of the glycocalyx can be altered either by controlled cross-linking or by controlled enzymatic (heparinase) degradation, while the flexural rigidity of the antigens can be re-engineered by designing suitable mutant receptors. We suggest that for studying the effects of temperature on nanocarrier binding and testing our predictions in Table 6.4, the ideal experimental setup nanocarriers binding to fixed cells in vitro with arrested endocytosis between 4 and 37 ^{0}C. These, used in combination with experiments using engineered systems to alter glycocalyx properties can directly validate our model predictions in Table 6.4 and Fig. 6.8 with respect to the role of glycocalyx in altering the temperature dependence of nanocarrier binding to cells. A similar approach can be used to study the effect of antigen flexure on the temperature dependence of nanocarrier binding.

The interplay between different molecular and physical parameters often makes the results of biological experiments (such as nanocarrier binding to cells) difficult to analyze. By using our model, we have identified and dissected the effect of various parameters on the system's equilibrium behavior. The role of bond spring constant on carrier-binding to cells has been recognized by several researchers starting from the pioneering works of Bell [17, 18, 44, 69]. Our study here

identifies two interesting new parameters, namely, glycocalyx resistance and antigen flexural rigidity, which are also important determinants of nanocarrier binding. The presence of glycocalyx effectively increases the binding free energy by repelling nanocarrier away from the endothelium surface without affecting the multivalency for binding. This conclusion is unaltered for the entire range of bond stiffness and flexural rigidities we have explored in our simulations (Figs. 6.6, 6.7). For this reason, the contribution from the glycocalyx is independent and uncorrelated from those due to the other parameters such as bond stiffness and flexural rigidity. We note that apart from this thermodynamic contribution, the presence of the glycocalyx significantly introduces several kinetic and hydrodynamic effects thereby likely altering the transient characteristics of nanocarrier binding which we have not considered here; for a brief review, see Weinbaum et al. [178].

The effect of antigen flexure can be understood by considering two competing effects: (1) antigen flexural rigidity reduces nanocarrier binding by effectively increasing the binding free energy (by an amount equal to the average strain energy due to flexure) in comparison to a freely flexing antigen. We note that the binding free energy is a negative quantity and an increase implies less binding. (2) However, in comparison to a rigid antigen, a flexing antigen allows for a better exploration of the conformational space and enhances multivalency. The net effect is an increase in binding affinity due an enhancement in the average number of receptor-ligand bonds. For the range of parameters we have explored, we find that upon increasing the flexural rigidity, the proportion by which the multivalency decreases translates quantitatively into the proportion by which the corresponding binding free energy increases, suggesting that the second effect dominates over the first (Fig. 6.7). This behavior underscores the effect of flexural rigidity on nanocarrier binding and is unaltered in the presence or absence of glycocalyx. The analogous effect of varying the bond-stiffness (Fig. 6.6) on the multivalency and binding energy has a subtle but important difference. In this case, while an increase in bond stiffness leads similarly to an overall decrease in multivalency and increase in binding free energy, the proportion by which the multivalency decreases does not quantitatively translate into (and is greater than) the proportion by which the binding free energy increases. This difference suggests that for the case of bond-stiffness, the analogous competing effects (1) and (2) are both important. This is a reflection of the fact that the role of strain energy associated with bond-stiffness in increasing the effective binding free energy is significantly greater than the corresponding role of the strain-energy due to flexure for the systems we have studied.

Even though we have focused on an equilibrium model and simulations, the model itself can as such be incorporated in a kinetic setting with minimal adjustments: for example, by replacing the Monte Carlo protocol by a Langevin dynamics protocol. Moreover, even though our study was focused on rigid spherical nanocarriers to make contact with the experiments of Muro et

al. [117] using polystyrene nanospheres, there has appeared some very interesting recent data in the literature on the effect of nanocarrier size and shape [27, 59] and nanocarrier flexibility [59, 168] on binding properties. Extension of our model to treat rigid non-spherical nanocarriers is straightforward. However, including the effects of nanocarrier deformability in flexible carriers is more challenging. In this case, the choice of model integration would be dictated by the ratio of timescales: that associated with nanocarrier flexibility and that associated with the receptor-ligand binding reaction. This extension is also necessary for relaxing the assumption of the cell membrane surface as a planar rigid surface. In a live cell, membrane can undergoes undulations and a nanocarrier bound to live endothelial cell can additionally undergo endocytosis, which is preceded by membrane deformation and wrapping around the bound nanocarrier. Gao et. al. [56] have studied this problem in a model geometry (uniformly distributed antibodies and continuous density profile for antigens). As part of future work, we plan to combine our model discussed here along with a recent multiscale protocol [179] for membrane dynamics we developed in our laboratory in order to rigorously include the effects of membrane and carrier flexibility. Still, the simplified approach presented here, subject to the assumptions we have highlighted, qualifies as a predictive tool, and helps to provide a molecular resolution to the physico-chemical interactions and presents a unified molecular and energetic analyses of the nanocarrier binding process.

6.6 Appendix

6.6.1 Flexural Rigidity Of Antigens

The energy stored in a beam due to a constant moment acting on it is given by $U = M^2L/2EI$, where, M is the moment, L is the length of the beam and EI is the flexural rigidity of the beam. The deflection of a beam (oriented along x-axis with fixed end at the origin) is given by [144] $d^2y/dx^2 = -M/EI$. For a constant M, we obtain, $y = (-M/2EI)\,x^2 + Ax + B$. To solve for A and B, we set $y(0) = 0$ and $y'(0) = 0$, and thus obtain $y = (-M/2EI)\,x^2$. Thus, the deflection of the free-tip is given by $y(L) = y_L = (-M/2EI)\,L^2$. Substituting this result in the expression for the energy yields, $U(y_L) = (-2EIy_L/L^2)^2(L/2EI) = (2EI/L^3)y_L^2$.

6.6.2 Free Energy Change Due To Glycocalyx Resistance

In this section, we represent a free nanocarrier as B, a free antigen on the cell as σ, and a bound nanocarrier as C. We can write the nanocarrier adhesion as a reaction (assuming each nanocarrier binds to one antigen only): $B + \sigma \leftrightharpoons C$; $dC/dt = k_f B\sigma - k_r C$; k_f and k_r denote the respective

rates.

In a flow chamber experiment, the concentration of unbound nanocarriers is a constant. We can also express σ in terms of $\sigma = C_{\max} - C$, where, $C_{\max}$ is the maximum concentration of nanocarriers that can bind to the cell surface. Hence, $dC/dt = k_f B(C_{\max} - C) - k_r C$, with an initial condition of $C(t = 0) = 0$. We can integrate this differential equation to get:

$$C(t) = \frac{k_f B C_{\max}}{(k_f B + k_r)} \times (1 - \exp[t(k_f B + k_r)]) \,. \tag{6.6}$$

In the work of Mulivor [116], B is specified in units of number of nanocarriers per mm^3, while C is specified as number of nanocarriers adsorbed per 100 μm of venule. We take volume of 100 μm of the venule as our unit-volume. Diameter of each venule is 39.5 μm, and so the volume per 100 μm of venule is 1.2254×10^{-4} mm^3. Hence, the units for B we have adopted and their relationship to the convention of Mulivor et. al. is provided in Table 6.5. From the results of Mulivor, we deduce that nanocarriers/100 μm of venule.

B ($10^6/mm^3$)	B(no. of nanocarriers/100 μm of venule)
2.42	294.55
8.46	1036.99
10.87	1332.01

Table 6.5: Concentration of Nanocarriers

Hence, we fit the expression $C(t) = ((k_f B C_{\max})(k_f B + k_r)) \times (1 - \exp[t(k_f B + k_r)])$ to the experimental data of Mulivor in the absence of glycocalyx to obtain k_f and k_r (Table 6.6).

B(no. of nanocarriers/100 μm of venule)	k_f (no./100 μm of venule)	k_r (1/min)
294.55	2.436×10^{-5}	0.08304
1036.99	1.897×10^{-5}	0.07393
1332.01	3.755×10^{-5}	0.07965

Table 6.6: Rate Constant of Nanocarrier Binding Reaction

After removal of glycocalyx (t=30 min in the work of Mulivor), we can use the same rate equation, but with a slightly different initial condition: $C(t' = 0) = C_0$, where, $t' = t - 30$ min. We get,

$$C(t') = \frac{k_f B C_{\max}}{(k_f B + k_r)} + \left(C_0 - \frac{k_f B C_{\max}}{(k_f B + k_r)} \right) \times \exp[-(k_f B + k_r) t']. \tag{6.7}$$

After $t = 30$ min, the glycocalyx is removed. We assume that the glycocalyx removal only changes (increases) the forward rate, k_f, while, k_r remains the same. By fitting the Eqns. 6.6 and 6.7,

we obtain $k_f(t < 30\,\text{min}) = 500 \times k_f(t > 30\,\text{min})$. This implies that the equilibrium constant in presence of glycocalyx is reduced by a factor of 500 relative to that in its absence, i.e., $K = 500K_{\text{glyx}}$. Hence,

$$\Delta G_{\text{glyx}} = \Delta G + k_B T \ln 500 = \Delta G + 2.573 \times 10^{-20} \tag{6.8}$$

Within our harmonic model, the total resistance offered by the glycocalyx to nanocarrier adhesion is $E_{\text{glyx}} = 1/2 k_{\text{glyx}} \int\int \left(z - (L - z_c)\right)^2 dA$, (see Fig. 6.1 for nomenclature), where, the integration is over the area of nanocarrier that is immersed in the glycocalyx. The integral expressed in spherical coordinate system is:

$$E_{\text{glyx}} = \frac{1}{2} k_{\text{glyx}} \int_{\phi_0}^{\pi} \int_{0}^{2\pi} \left[R\cos\phi - (L - z_c)\right]^2 R^2 \sin\phi d\theta d\phi, \tag{6.9}$$

where, $\phi_0 = \cos^{-1}\left((L - z_c)/R\right)$ and R is the hard sphere radius. The integral is solved to yield:

$$E_{\text{glyx}} = \frac{1}{2} k_{\text{glyx}} \left[\frac{2\pi R^4}{3}(\cos^3\phi_0 + 1) + 2\pi R^3 \sin^2\phi_0 (L - z_c) + 2\pi R^2 (L - z_c)^2 (\cos\phi_0 + 1)\right], \tag{6.10}$$

which, upon further simplification gives,

$$E_{\text{glyx}}(z_c) = \pi R^2 k_{\text{glyx}} \left[\frac{R^2}{3}(\cos^3\phi_0 + 1) + R\sin^2\phi_0 (L - z_c) + (L - z_c)^2 (\cos\phi_0 + 1)\right]. \tag{6.11}$$

Equating $\Delta G_{\text{glyx}} - \Delta G$ in Eq. 6.8 to $E_{\text{glyx}}(z_c)$ in Eq. 6.11 allows us to estimate the value of k_{glyx} consistent with the experimental data of Mulivor et. al. This value for the glycocalyx spring constant (k_{glyx}) is provided in Table 6.1.

6.6.3 Force Spectroscopy

In force spectroscopy experiments, a constant/variable loading rate (force/time) is applied to the bonded antigen-antibody, and the time (i.e. force) at which bond ruptures is recorded [70, 185]. This experiment is repeated number of times to give rupture force distribution at a given loading rate.

From Evans [46], the probability of bond-rupture in a time interval $(t, t + dt)$ is given by:

$$p(t, f) = k_{\text{off}}(f) \exp\left[-\int k_{\text{off}}(f) dt\right]. \tag{6.12}$$

The pre-factor represents the probability of dissociation in the next short interval of time, dt, whereas the exponential term represents the probability of the bond having survived up to time, t. We express $\Delta G(L) = -k_B T \ln K = -k_B T(\ln k_{\text{on}} - \ln k_{\text{off}})$ using the Bell [18] model, as $\Delta G(L) = \Delta G(\sigma) + 1/2k(L - \sigma)^2$. We assume that k_{on} is bond-length independent (since k_{on} is often diffusion-based; this assumption is consistent with Bell [17]). Hence, we obtain,

$$\Delta G(L) - \Delta G(\sigma) = k_B T(\ln k_{\text{off}}(L) - \ln k_{\text{off}}(\sigma)) = \frac{1}{2} k (L - \sigma)^2, \tag{6.13}$$

$$k_{\text{off}}(L) = k_{\text{off}}(\sigma) \exp\left[\frac{\beta}{2} k(L-\sigma)^2\right] \tag{6.14}$$

i.e.

$$k_{\text{off}}(L) = k^0_{\text{off}} \exp\left[\frac{\beta}{2} k(L-\sigma)^2\right] \tag{6.15}$$

Consistent with the harmonic approximation of Bell, $f = -k(L-\sigma)$. Using this definition in the above equation, we can express $k_{\text{off}}(L) = k^0_{\text{off}} \exp\left[(\beta/2)(f^2/k)\right]$, and hence the probability as:

$$p(t,f) = k^0_{\text{off}} \exp\left(\frac{\beta}{2}\frac{f^2}{k}\right) \exp\left[-\int k^0_{\text{off}} \exp\left(\frac{\beta}{2}\frac{f^2}{k}\right) dt\right] \tag{6.16}$$

Expressing time in terms of the loading rate as $t = f/r_f$ yields:

$$p(f) = k^0_{\text{off}} \exp\left(\frac{\beta f^2}{2k}\right) \exp\left[-\int k^0_{\text{off}} \exp\left(\frac{\beta f^2}{2k}\right) \frac{1}{r_f} df\right]. \tag{6.17}$$

The median of the probability distribution in Eq. 6.17 is obtained by setting $d/df\, p(f) = 0$, i.e., $d/df \ln p(f) = 0$ to get $\beta f \times r_f = k \times k^0_{\text{off}} \exp\left(\beta f^2/2k\right)$.

Hence, by fitting the equation to single molecule data, we can calculate bond-spring constant k and k^0_{off}. That is, we plot $x = \beta f^2/2$ versus $\beta f \times r_f$ to get bond-spring constant k and k^0_{off} (see Table 6.7).

antigen-antibody pair	r_f (pN/s)	k (dyn/cm)	k^0_{off} (1/s)	r^2
ILFA-1/iICAM-1 [185]	20-10,000	1143.38	10.34	0.9955
hLFA-1/iICAM-1 [185]	20-10,000	1219.66	2.3	0.9989
ILFA-1/iICAM-1 w/EDTA [185]	20-10,000	484.5	8.475	0.9979
P-selectin/PSGL-1 [70]	100-10,000	2509.4	2.06	0.9987
P-selectin/LS174T [70]	200-5000	1310.44	5.86	0.9943

Table 6.7: Rate Constant of Nanocarrier Binding Reaction

Chapter 7

Geometry of mediating protein affects the probability of loop formation in DNA

7.1 Introduction

Since its discovery in the 1980s enzyme mediated DNA looping has been implicated as the key to many important biological processes. For example, the activity of the *lac*, *gal* and *lambda* operons in *E.coli* is known to be regulated by the formation of DNA loops mediated by their respective repressor proteins [151]. Similarly, the functioning of many restriction enzymes is known to be controlled by the formation of loops in DNA [68]. A subclass of these enzymes called two-site restriction endonucleases efficiently cleave the double stranded DNA only if they interact with the DNA at two distant sites. In fact, a majority of reactions on DNA that include transcription, replication and repair, site-specific recombination etc., are mediated by multimeric proteins that interact with DNA at multiple sites [68]. As a result the biochemistry and biophysics of these reactions have been the subject of many experimental, computational as well as theoretical investigations. A key question in this context is, "What molecular machinery or mechanism governs the rate at which two distant sites on the DNA are brought close to each other?"

The quest to address this question has produced several studies [57], through which a reasonably clear picture has emerged for the related process of DNA cyclization in which two sticky ends (short regions of single-stranded DNA with complementary base-pairs) of a piece of linear double

stranded DNA are juxtaposed to produce a circular DNA loop in the absence of any mediating protein. The equilibrium constant for the cyclization reaction is governed by the length of the DNA involved [159]. For DNA lengths longer than 300 base-pairs (bp), this has been proved by the remarkable agreement of bulk biochemical experiments [31], Monte-Carlo (MC) simulations [40], and theories based on the worm-like-chain (WLC) models of DNA [159, 180]. There is still some debate [31, 40] about the cyclization propensity of short (about 100 bp) DNA fragments – the data from some bulk biochemical experiments have been explained on the basis of non-linear models that require the formation of flexible hinges (or kinks) in the DNA [93, 180] while those from another set of bulk experiments seem to agree quite well with the traditional WLC model of DNA without any need for non-linearities such as kinks or hinges [40].

On the other hand, enzyme mediated DNA loops have been studied primarily by single molecule techniques which burst into the scene about two decades ago. The majority of experiments involving DNA looping are carried out using the tethered particle assay in which one end of the DNA is immobilized by attaching it to a cover-slip or to an optically trapped bead while the Brownian motion of the other end, also attached to a bead, reports on the formation/breakage of enzyme mediated loops [49]. The bead at the other end can be trapped optically or magnetically [99] allowing for the possibility of exerting forces and moments on the DNA which can attenuate the rate of the looping reaction. This technique has been used to study the kinetics of formation/breakage of loops formed by the *lac*, *gal*, *lambda*-repressors [49, 99, 187] as well those by the restriction enzymes NaeI and NarI [169]. The constant formation/breakage of the loops (over times scales on the order of 10s for NaeI [169], for instance) in these experiments which typically span several minutes or hours ensures that this process is well described by equilibrium binding statistics. Once again, an important question that arises in this context concerns the effect of the length of the DNA loop on the rates of the forward/backward reaction or equivalently on the equilibrium constant of looping. This question of length dependence was addressed in a recent single molecule experiment in which the probability of loop formation was measured as a function of DNA length for several two-site restriction enzymes [58]. The key results of this experiment were that, (i) the probability of forming short DNA loops (about 100bp or less) is much higher than predicted by a theory based on the WLC theory of DNA mechanics alone, (ii) the data agree better with theories of DNA with kinks and hinges, (iii) the probability density as well as the optimal loop length is highly dependent on the looping protein. In this set of experiments large forces were required to accelerate the rate of the loop breaking reaction for some proteins implying that the results report on the probability of loop formation alone and not on the equilibrium constant of the loop formation/breakage reaction.

It is our goal in this paper to explore a possible explanation for these observations by accounting

for the geometry of the looping protein. We do not invoke non-linear theories of DNA involving kinks or hinges. We also assume that the protein acts as a coupler and has no elasticity of its own. The calculations presented here have been carried out in two-dimensions so that the only mode of deformation available to the DNA is bending in a plane. As a result other sources of non-linearities such as coupling between twisting and bending modes [32, 137] are not considered in this model. In contrast to the work of Merlitz *et al.* [113], we also do not account for the electrostatic interaction and the stretching energy of the DNA. These calculations are a precursor to more comprehensive three-dimensional calculations where the DNA can bend and twist [32]. An advantage of two-dimensional calculations is that the analytical theory remains tractable while not sacrificing the important concept of the competition between elasticity and entropy that governs the physics of DNA cyclization and looping reactions at equilibrium. For example, the peak in the Jacobson-Stockmayer (J) factor [77] for DNA cyclization can be seen both in two as well as three-dimensional MC simulations although it is shifted to longer DNA lengths in the two-dimensional setting since entropic forces are relatively weaker in this case [86]. We show in this paper that the mere introduction of the span of the protein complex (denoted by the length scale a throughout this paper) together with the competition of elastic and entropic forces results in probability density functions (probability of loop formation as function of length) that can vary significantly with protein geometry. A battery of MC methods have been employed to arrive at the probability density functions presented in this paper. The details are explained in section 7.3. In some cases we have also verified our MC calculations by comparing with analytical calculations based on the treatment of DNA as a fluctuating elastic rod.

We observe two important effects that seem to directly depend on the size of the enzyme: (i) the overall propensity of loop formation at any given value of the DNA contour length increases with the size of the enzyme, and (ii) the contour length corresponding to the first peak as well as the first well in the probability density functions increases with the size of the enzyme. Another interesting outcome of the MC simulations of DNA loops presented in this paper is the visualization of the fluctuating shape. We find that for loop lengths which are small multiples of the DNA persistence length the shape fluctuates close to an equilibrium shape which can be calculated from the Kirchhoff theory of rods. The fluctuations around the equilibrium shape contribute to the configurational entropy. If the fluctuations are small enough we can expand the elastic energy functional up to quadratic order in the fluctuations around equilibrium and obtain a fluctuation operator. The eigenmodes of this operator show us the collective motions of the DNA molecule. We have analytically calculated the slowest eigenmode of this fluctuation operator and compared our expressions with the results of a numerical eigenfunction analysis of the MC data. Remarkably,

we find good agreement between the two methods. To our knowledge this is the first time the shape fluctuations have been computed using analytical techniques for this problem. We note that a similar computation of eigenfunctions for boundary conditions involving a given force and zero moments at the ends was performed by Kulic *et al.* [91]. Such shape fluctuations in macromolecules are now known to play a key role in determining the free energy change associated with binding two species [53].

7.2 Theory

7.2.1 Mechanics of the DNA loop

In this paper we model the DNA as an inextensible, homogeneous, isotropic rod with bending stiffness K_b. K_b can be determined from the persistence length ξ_p through the relation $\xi_p = \frac{K_b}{k_B T}$ where k_B is the Boltzmann constant and T is the absolute temperature. In this paper we take $\xi_p = 50$nm [107] for double-stranded DNA and $k_B T = 4.1$pNnm which corresponds to value at room temperature. The protein is modeled as a coupler of size a. For example, a dimer of the restriction enzyme BfiI has size of 10nm (PDB ID: 2C1L). More precisely, a is the spatial distance between the points at which the protein binds to the DNA. The protein is usually a dimer, tetramer etc., and is often symmetric. We therefore expect the DNA loop to be symmetric as well and choose the y-axis as the axis of symmetry (Fig. 7.1). The protein exerts a force F on the DNA which, by symmetry, has to lie along the x-axis in our model. With no other forces being exerted on the DNA in the looped region we know that equilibrium demands that

$$K_b \theta'' + F \sin\theta = 0, \tag{7.1}$$

where $\theta(s)$ is the angle made by the tangent at any point s to the positive x-axis and $'$ denotes differentiation with respect to the arc-length s. Recalling that $K_b \theta'(s) = M(s)$ is the bending moment we can see that Eq. 7.1 is a second order non-linear differential equation in $\theta(s)$ which expresses a balance of moments at every point on the DNA. The solution of Eq. 7.1 requires that we specify two boundary conditions. We will consider several possibilities here. If the protein is a rigid jig then we will require

$$\theta(0) = 0, \qquad \theta(\frac{L}{2}) = \pi + \theta_a. \tag{7.2}$$

The first of these conditions is required by the assumption of symmetry while the second one will be dictated by the constraint posed by the protein-DNA interaction. We assume that the angle θ_a can be reasonably determined from the co-crystal structure of the protein bound to the DNA and that the protein is rigid enough to exert a moment on the DNA to ensure that the boundary

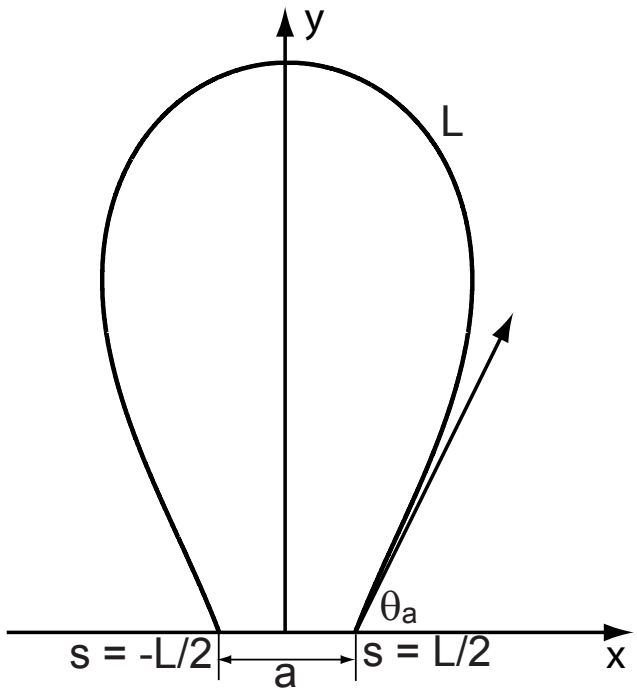

Figure 7.1: Schematic of protein mediated two-dimensional DNA loop. a is the size of the protein holding the loop.

condition is obeyed. If on the other hand the protein is flexible (for example, *lac*-repressor [55, 112] and AraC [71]) then the appropriate boundary conditions would be that the protein does not exert any moments on the DNA. In such a scenario the boundary conditions would be

$$\theta(0) = 0, \qquad \theta'(\frac{L}{2}) = 0. \tag{7.3}$$

Finally, the constant F is determined by enforcing the constraint on the end-to-end distance

$$\int_{-\frac{L}{2}}^{\frac{L}{2}} \cos\theta ds = a. \tag{7.4}$$

The boundary value problem consisting of the differential equation 7.1 together with boundary conditions given by Eq. 7.2 and Eq. 7.4 (as well as its three-dimensional version) has been solved analytically by Purohit and Nelson [137]. For solving the problem with boundary conditions Eq. 7.3 it is useful to recall that the solution to Eq. 7.1 can be written in terms of elliptic functions to

obtain the following:

$$\theta'(s) = \frac{2k}{\lambda}\mathrm{cn}(\frac{s}{\lambda}|k),$$
$$\cos\theta(s) = 1 - 2k^2\mathrm{sn}^2(\frac{s}{\lambda}|k),$$
$$\sin\theta(s) = 2k\mathrm{sn}(\frac{s}{\lambda}|k)\mathrm{dn}(\frac{s}{\lambda}|k), \tag{7.5}$$

where $\lambda = \sqrt{\frac{K_b}{F}}$ and k are constants. Clearly, $\theta'(\frac{L}{2}) = 0$ requires $\mathrm{cn}(\frac{L}{2\lambda}|k) = 0$ which is possible only if $\frac{L}{2\lambda} = K(k)$ where $K(k)$ is the complete elliptic integral of the first kind. This constraint together with the following can be solved to determine λ and k for given values of L and a.

$$2E(k) - K(k) = \frac{2a}{L}K(k), \tag{7.6}$$

where $E(k)$ is the complete elliptic integral of the second kind. Eq. 7.6 above results from the constraint $\int_{-L/2}^{L/2}\cos\theta ds = a$. It is clear that the angle θ_a at the ends of the loop is then determined through

$$\theta_a = \pi - \cos^{-1}(1 - 2k^2). \tag{7.7}$$

Viewed differently, k (with $0 \leq k \leq 1$) parameterizes the dependence of the angle θ_a on $\frac{L}{a}$ through equations 7.6 and 7.7. This dependence has been plotted in Fig. 7.2. The equilibrium shapes of the loop obtained above do not account for the role of fluctuations. In general this is a difficult exercise, but in the limit of small fluctuations around the equilibrium configuration, we can make considerable progress by expanding the energy upto quadratic order in the fluctuations.

In the case of the DNA loop, we expand the energy upto quadratic order in the fluctuations $\delta\theta(s)$ of the angle $\theta(s)$ made by the tangent to the x-axis. In other words, we write

$$E[\theta(s) + \delta\theta(s)] = E[\theta_{eq}(s)] + \frac{\delta\theta(s)\mathbf{T}(s)\delta\theta(s)}{2}, \tag{7.8}$$

where the stiffness $\mathbf{T}$ (also called the fluctuation operator) contains information about fluctuations, and $E[\theta_{eq}(s)]$ is the elastic energy corresponding to the equilibrium shape of the loop. Note that there is no first order term in $\delta\theta$ since equilibrium implies that $\frac{\delta E}{\delta\theta} = 0$. The eigenmodes of the fluctuation operator ultimately contribute to the entropy. In the section 7.6.1 we explicitly compute the fluctuation operator for a DNA loop and determine its lowest eigenmode. We then compare the analytical expressions with our MC simulations and plot the results in fig.7.3.

7.3 Simulation Methods

Summary: We employ a battery of MC methods to quantify the behavior of the DNA loop in two-dimensions. We calculate the loop formation probability, $P(L;a)$ of a fragment of the DNA

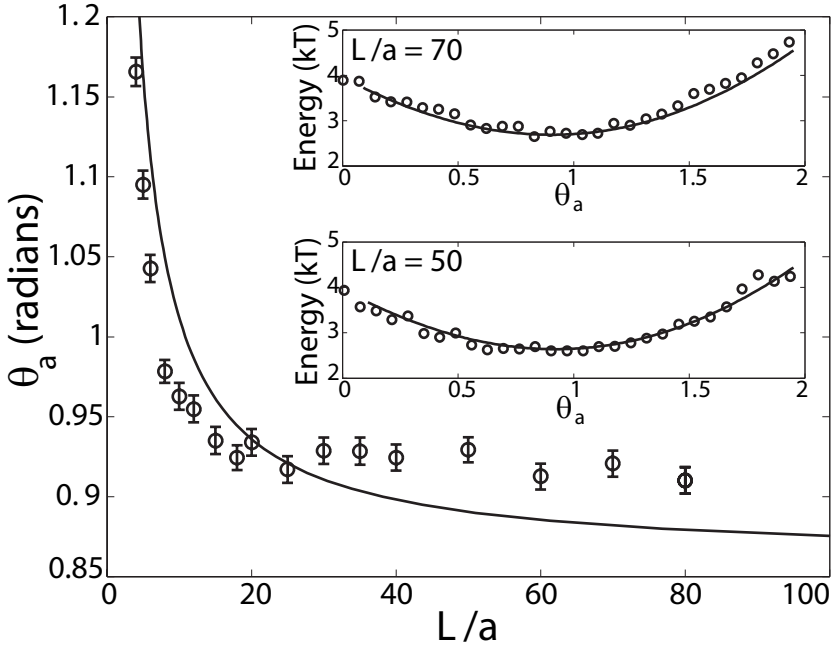

Figure 7.2: Most probable angle θ_a plotted as function of L/a. Error bars represent standard error in the reported values. As $a \to 0$ we see that $\theta_a \to 49.5^o$ which corresponds to a loop opening angle of 81^0 predicted by Shimada and Yamakawa [159]. The most probable angle was obtained from the probability distribution of the end angles of the loops generated by the MC simulations. The line is the result of a calculation based on a minimization of elastic bending energy which predicts that the optimal loop is the one whose curvatures are zero at the ends. This condition corresponds to a situation in which the protein exerts no moments on the DNA. The inset shows the energy of an elastic rod plotted as a function of θ_a for $L = 5\xi_p$ and two different values of L/a. In both the panels we also plot $-\log(P(\theta_a; L/a)) + C$ where C is an arbitrary constant using data from MC simulations and find good agreement. We note that the energy wells in both the panels are shallow (which implies that we should expect a large variance)which explains why the MC data for most probable θ_a for large values of L/a does not agree too well with the curve.

of length L and given end-to-end distance, a when the opening angle is allowed to vary using the method (described in section 3.1) proposed by Czapla *et. al.* [32]. A Metropolis based Monte Carlo method (described in section 3.2) is used to quantify fluctuations of the DNA loop while the density of states monte carlo (DOSMC), see section 3.3, is used to validate the quasi-harmonic assumption employed in our theory. Our methods are checked for consistency by comparing mean

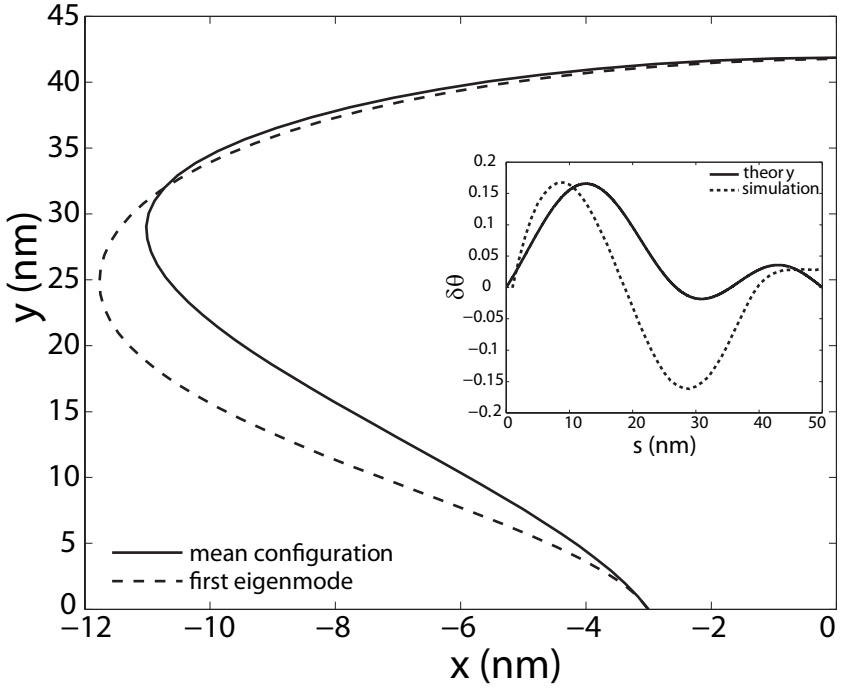

Figure 7.3: The first eigenmode of the fluctuating loop obtained from MC simulations. The solid line represents the mean configuration and the dashed line represents the deformation due to the fluctuations along the first eigenmode. The end-to-end distance of the loop is fixed and so are the angles made by the tangents (to the x-axis) at the ends. The inset shows the corresponding change in the tangent angle $\delta\theta$ as a function of the arc-length s calculated using theory (solid line plotted using Eq. 7.23) and using MC simulations (dotted line) calculated as described in Eigenmode Calculations.

potential energy of an ensemble of fluctuating DNA loop configurations of a given loop by all three methods. In the above simulation protocols, we discretize the double stranded DNA of fixed L and a into N rigid links, each of length Δs. Unless specified, the link length is taken to be 1 nm, i.e. $\xi_p/50$. Following Klenin [89], we also calculate the correction to the persistence length due to discretization of DNA. This correction is small since the chosen link length is small compared to the DNA persistence length, and hence, it is neglected. To treat the angles at the boundaries, we use the boundary condition that $\theta'(\pm L/2) = 0$, which corresponds to a flexible protein (see Eq. 7.3). In our simulations, we use $\xi_p = 50$ nm and $k_BT = 4.1$ pNm. We describe the potential energy

of each conformation of the DNA loop as

$$E\left[\theta\left(s\right)\right] = \sum_{i=1}^{N-1} \frac{\xi_p \left(\Delta\theta_i\right)^2 k_B T}{2\Delta s}, \tag{7.9}$$

where we have replaced the derivative $\frac{d\theta}{ds}$ by $\frac{\Delta\theta_i}{\Delta s}$, the bending modulus K_b by $\xi_p k_B T$, and summed over all the links.

7.3.1 P(L;a) calculation

We employ a methodology, termed as Gaussian sampling, from the work of Czapla *et. al.* [32]. This MC method is superior to the more traditional Metropolis MC method for calculating $P(L;a)$ because it is computationally efficient, and it does not suffer from correlations between trial configurations. In the Gaussian Sampling protocol, the DNA chain is grown link-by-link by adding a new link to the pre-existing chain at the growing end until the desired DNA length is reached. Adding a new link at an angle $\Delta\theta_i$ to the growing end demands an energy $\left(\xi_p(\Delta\theta_i)^2 k_B T\right) / (2\Delta s)$. Hence, this angle is sampled from the following Gaussian distribution dictated by a Boltzmann distribution at equilibrium:

$$p(\Delta\theta_i) = \sqrt{\frac{\xi_p}{\Delta s}} \frac{1}{2\pi} \exp\left(-\frac{\xi_p \Delta\theta_i^2}{2\Delta s}\right). \tag{7.10}$$

Since, rigid body (overall) translation and rotation of the DNA loop do not contribute to loop formation probability, we effectively remove them by constraining the first link in a vertical orientation at the origin. Once the DNA has grown to a total length of L, the distance between the first and the last link is computed. If this distance lies in the interval $[a-\delta, a+\delta]$, we record it as a "hit" (where δ is the tolerance). This process is repeated 1 billion times (N_{try}) yielding N_{hits} hits. $P(L;a)$ is simply the ratio of N_{hits} to N_{try}. Results are reported as an average over 4 different runs with different initial conditions for the random number seed to generate $p(\Delta\theta_i)$ in Eq. 7.10. To quantify the dependence of the angle θ_a on L/a, for every hit, the observed value of θ_a is recorded, and a mean is computed over the N_{hits} values after each simulation run.

Figures 7.4 and 7.5 report the equilibrium probability of loop formation P(L;a) for different values of L and a while Fig. 7.2 reports the equilibrium value of average opening angle (defined as $\pi - 2\theta_a$) over all conformations recorded as hits as a function of L/a.

7.3.2 Eigenmode calculation

Eigenmodes of the DNA thermal fluctuations can be extracted based upon the knowledge of various loop configurations. In our model, we sample DNA loop configurations from a constant length-constant separation-constant temperature ensemble. New loop conformations are generated from

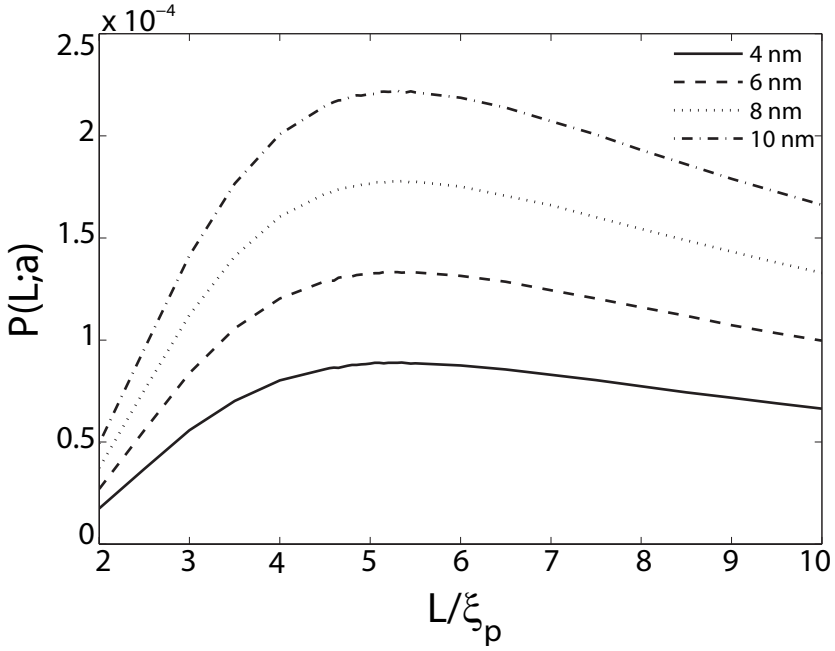

Figure 7.4: Probability of loop formation $P(L;a)$ plotted as a function of non-dimensionalized length L/ξ_p for various values of the end-to-end distance a. The probability is peaked around $L/\xi_p = 5$. There is also a second peak at much smaller values of L/ξ_p which is depicted in Fig. 7.5. A peak at $L/\xi_p \approx 5$ is expected from the classical WLC model of DNA which does not account for the presence of the protein. The location of this peak shows only a weak dependence on a. Link length = 2.5 nm; tolerance in a = 0.5 nm. Coefficient of variation of P(L;a) (not shown in the figure) is less than 1 %.

existing one by crankshaft rotation [172]. A sub-chain containing a random number of links is flipped about an axis joining the end points of this segment. This new conformation is selected with a probability of acceptance $\min\left[1, \exp\left(-\frac{E_{new}-E_{old}}{k_B T}\right)\right]$ to satisfy the Metropolis criterion [9], where E_{new} and E_{old} are the energies of the new and old conformations, respectively and the min function selects the minimum of the two terms in parenthesis. In our model, overlap of DNA segments is not allowed and therefore, trial moves generating loop-segment overlap ($E_{new} = \infty$) are automatically discarded by the acceptance criteria. The eigenmode calculations can be performed by either imposing fixed end-angles or variable end-angles in the simulation. However, the theoretical calculation of the first eigenmode (see section 7.6.1) is performed for the case when the end-angles are fixed. Therefore, to make the explicit comparison with the theoretical result, we impose that the end-angles are fixed in our Metropolis MC simulations. Rigid body translation and

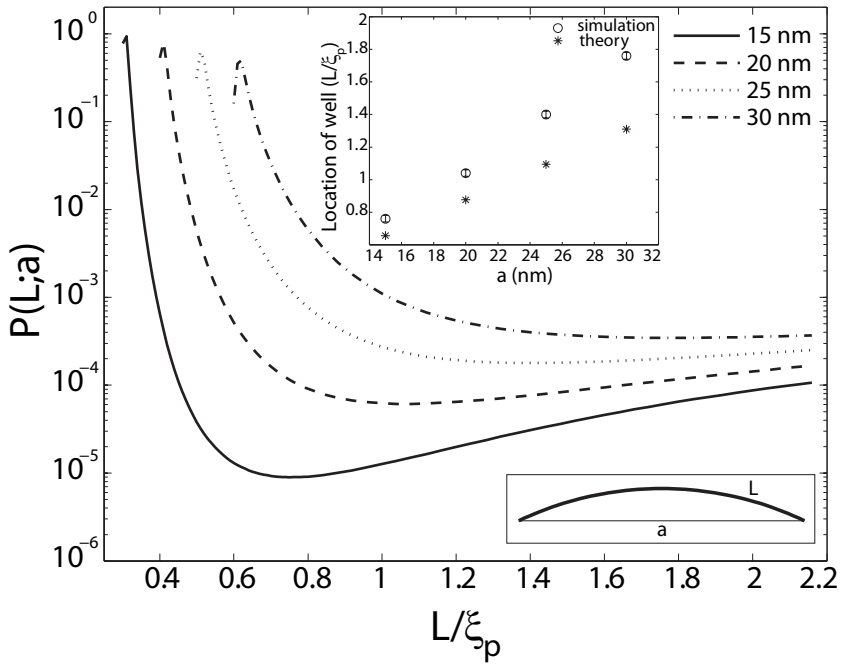

Figure 7.5: Probability of loop formation $P(L;a)$ plotted as a function of non-dimensionalized length L/ξ_p for various values of the end-to-end distance a. The presence of a new length scale a imposed by the protein results in a second peak at small values of L. The WLC theory for cyclization does not predict this peak. The wells in the probability distributions correspond to lengths at which the elastic energy required to bend a short fragment of DNA to satisfy the constraint on end-to-end distance is a local maximum. The inset on the top shows that there is good correlation between the locations of the well determined from the MC simulations *vs.* the locations of maximum bending energy. The disagreement between these two calculations increases with increasing length due to the increasing effects of fluctuations. The inset in the bottom depicts the shape of a DNA loop when $L \approx a$. Link length = 1.0 nm; tolerance in $a = 0.5$ nm. Coefficient of variation of P(L;a) (not shown in the figure) is less than 1 %.

rotation are removed by holding the end-points of the DNA loop fixed. Each MC run is carried out 1 billion times to ensure that the system reaches equilibrium and the properties (average energy) converge.

The initial geometry of the links of the DNA loop, to begin the MC simulations, is obtained from the minimum energy configuration by solving the following discrete version of Eq. 7.1:

$$K_b \left(\frac{\theta_{i+1} - 2\theta_i + \theta_{i-1}}{(\Delta s)^2} \right) = -F \sin(\theta_i). \tag{7.11}$$

This equation is a boundary value problem and is solved numerically using a shooting method [75] by varying the force, F (Lagrange multiplier) in order to satisfy the constraint of end-to-end distance.

To calculate the eigenmodes of DNA loop fluctuations from the MC data, a covariance matrix $C_{ij} = \langle (r_i - \langle r_i \rangle)(r_j - \langle r_j \rangle) \rangle$ is constructed [10], where r_i is the position vector of each link, and $\langle \cdot \rangle$ represents average over conformations sampled from the MC run. Eigenvectors of this matrix represent the principal modes of loop fluctuations, while each eigenvalue indicates the squared amplitude of the fluctuations along each eigenmode. Since, the eigenvectors are orthogonal, they represent independent modes (basis functions) for describing the collective DNA loop fluctuations in the equilibrium ensemble of the conformations.

Fig. 7.3 reports the calculated shape of the first (slowest) eigenmode resulting from the covariance analysis (see above).

7.3.3 Validation of the quasiharmonic assumption

To calculate the eigenfunctions of the fluctuation operator, **T** (see section 2.2), we expanded the potential energy functional to quadratic order in $\delta\theta$, thus treating the DNA loop as quasiharmonic system. In this section, we describe a method to validate this assumption by comparing the configurational density of states (DOS) of the DNA loop against that of n-independent harmonic oscillators. To this end, we use the DOSMC method, developed by Wang and Landau [175], to calculate DOS of the DNA loop. DOSMC is an enhancement over conventional MC techniques since it directly produces the DOS, $g(E)$ instead of the canonical distribution $g(E)e^{-\frac{E}{k_B T}}$ generated by conventional techniques. DOSMC achieves this task by performing a random walk in energy space instead of random walk in the conformational space. Starting from $g(E) = 1$ and energy histogram, $h(E) = 0$, random walks in the energy space are performed by generating new loop conformations by crankshaft rotation (see section 3.2). The new conformation is accepted with a probability $\min\left[\frac{g(E_{old})}{g(E_{new})}, 1\right]$. Each time an energy state is visited, the corresponding DOS and energy histogram are updated according to $g(E) = g(E) \times f$ and $h(E) = h(E) + 1$, where f is a modification factor greater than 1 (in our simulations, we take $f = e^1$). The random walk in energy space is continued until the accumulated energy histogram is flat within a predefined tolerance (we define a histogram to be flat when $h(E)$ is within $\pm 5\%$ of average $h(E)$). To increase the accuracy of $g(E)$ (which is proportional to $\ln f$), f is reduced according to the rule $f_{new} = \sqrt{f_{old}}$, and the histogram is reset to zero, i.e. $h(E) = 0$. These steps are performed until the desired accuracy in $g(E)$ is obtained. In this work, simulations are performed till f reduces to 10^{-7}. To speed up the simulations, the energy space is divided into overlapping energy windows. Any walk outside the corresponding energy window is rejected. To satisfy the boundary condition imposed by Eq. 7.3,

the energy cost to change the terminal angle the last/first link makes with the positive x-axis is set to zero. At the end, resultant pieces of $g(E)$ in the respective windows are merged together so as to minimize the error between $g(E)$ in the overlapping regions. The obtained $g(E)$ is an accurate estimate of the configurational DOS of the system upto a constant multiplicative factor.

For a DNA loop of n links (i.e. length $n\Delta s$) in 2 dimensions, a total of $2n+2$ coordinates need to be specified. However, the following constraints on the system reduce the degrees of freedom available to the DNA loop: (i) absence of rigid body translation and rotation defines 3 constraints, (ii) each link length being constant defines n constraints, and (iii) distance between first and last link being constant defines 1 constraint. Hence, the DNA loop effectively has only $(n-2)$ degrees of freedom. The quasiharmonic treatment of the DNA loop assumes that DNA motion can be treated as a collection of $(n-2)$ independent harmonic oscillators. For a system comprised of m independent harmonic oscillators, the number of states with a total configurational energy between energy E and $E+dE$ is $N(E)dE$, where $N(E)$ is given by [140]:

$$N(E) \propto \int_{-\infty}^{\infty} \delta\left(E - \sum_{i=1}^{m} \frac{1}{2} k_i x_i^2\right) \prod_{i=1}^{m} dx_i, \tag{7.12}$$

where δ is the Dirac delta function, and k_i and x_i are the respective spring constant and displacement of the i^{th} oscillator. The DOS for this system is then $g(E) = \frac{dN(E)}{dE}$ yielding $g(E) \propto E^{\frac{m}{2}-2}$ (in deriving this relation, we first performed the integration in Eq. 7.12 [131]). Hence, if the quasiharmonic approximation holds for a DNA loop of n links, its DOS should obey $g(E) \propto E^{\frac{n-2}{2}-2}$. By comparing the slope of the $\ln g(E)$ versus E plot (see Fig. 7.6) from the DOSMC simulations to the slope, which is equal to the density of states exponent, from the above expression, i.e. $(n-2)/2-2$, (see Fig. 7.6 inset) we can assess the validity of quasiharmonic approximation for the DNA loop.

7.4 Results and Discussion

The main message of this paper is that the probability of loop formation in DNA is affected by the geometry of the looping protein. This result is manifest in the Fig. 7.4, 7.5 and 7.2. Fig. 7.4 shows the probability of loop formation $P(L;a)$ as a function of the length L of the loop and the size of the protein a. As expected from the classical WLC model [181] of DNA there is a peak in the probability of loop formation for $L/\xi_p \approx 5$. This is a result of the competition between elastic bending and entropy. The probability is not much affected by the protein size a at these lengths since $a << L$. Similar conclusions were reported also by Merlitz *et al.* [113] who showed (using a Brownian dynamic simulation) that the effect of the finite size of the looping protein are most dramatic for contour lengths less than 300bp and small for lengths greater than 500bp. This does

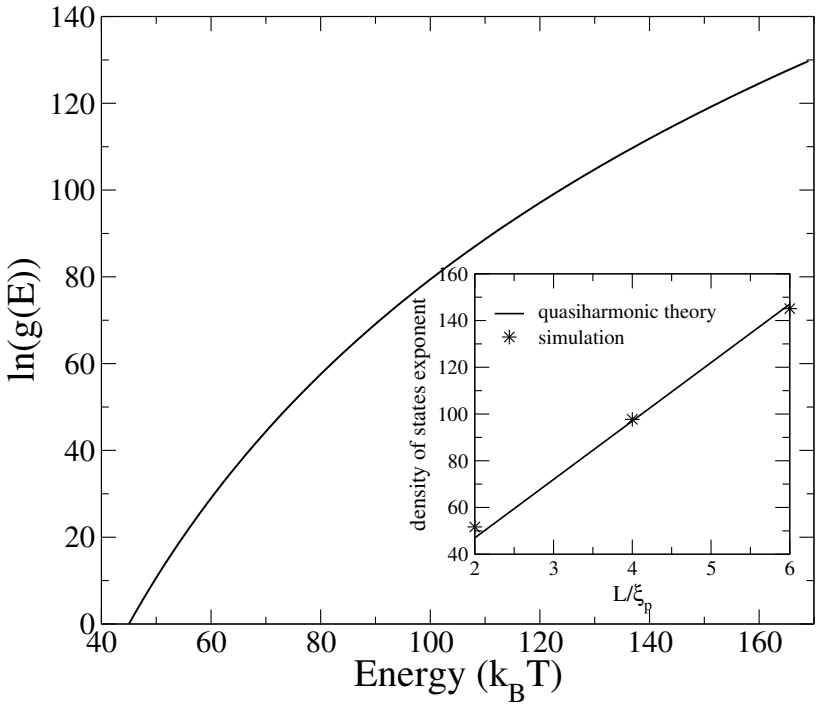

Figure 7.6: DOS for the 200 nm fluctuating DNA loop plotted as a function of the energy. The inset shows the DOS exponent as a function of the non-dimensionalized length L/ξ_p. The excellent agreement between the slope predicted from quasiharmonic theory of independent oscillators with that from DOSMC simulations shows that expanding the energy upto quadratic order in the fluctuations in $\theta(s)$ is a good approximation for the lengths of the DNA considered in this paper.

not imply, however, that the size of the protein is irrelevant for these loop lengths. This can be better appreciated from Fig. 7.2 which summarizes the effect of protein size on the value of the loop opening angle. For example, the optimal opening angle of a DNA loop is known to be 81^o when $a \to 0$ [159] but for $a = 10$nm at $L \approx 250$nm we find an optimal opening angle of 75^o. Fig. 7.2 also suggests that the most probable shape of the loop corresponds to the case in which the curvatures at the ends are zero. Evidence for this assertion comes from the strong correlation between the continuous line obtained from an argument resting on the minimization of elastic energy of the loop and the data obtained from MC simulations, and the fact that an opening angle of 81^o for $a = 0$ calculated by Shimada and Yamakawa does actually correspond to the zero end curvature condition. This observation implies that the most probable loop shape is one in which the protein exerts no moments on the DNA at their points of contact. The agreement between the curve obtained from the elastic calculation and the data obtained from MC simulations seems to get poorer as $L \to \infty$.

The reason for this can be understood by looking at the insets of Fig. 7.2. The continuous lines in the inset were obtained by calculating (following Purohit and Nelson [137]) the elastic energy of the loop as a function of the end-angle θ_a for $L = 5\xi_p$ and two different values of a. The open circles are data from MC simulations for the same values of L and a. The probabilities were converted into energies (upto an additive constant) through the Boltzmann law. It is remarkable that the data from the MC simulations agree so well with the elasticity calculation. This suggests that the shapes of the loop corresponding to different values of the fluctuating variable θ_a are such that the corresponding energies are not too different from the equilibrium shape for those boundary conditions. We also see that for large values of L/a the probability of having an end-angle θ_a is peaked at the value of θ_a corresponding to zero end moments. However, the energy well is shallow, implying that the variance is large. This is the reason behind the relatively poorer agreement between the two methods used for determining the most probable value of the end angles. One has to do an impractically large MC calculation to obtain better agreement.

The most significant effects of protein size are felt at small values of the length L. The probability of loop formation is peaked at values of L that are comparable to a as seen from Fig. 7.5. This peak is significantly higher than the peak observed at $L/\xi_p \approx 5$ and has not been predicted by the classical WLC model of DNA. Some researchers have suggested that looping probabilities will necessarily be high when the DNA contour length is comparable to the span of the protein complex but a quantitative prediction remains lacking [39]. In fact, most studies which predict high probability of loop formation at short DNA lengths do so only after the introduction of defects, such as, kinks or hinges in the DNA, thus deviating from the WLC model [39, 145, 150, 180]. A notable exception is a study by Merlitz *et al.* [113] which shows, through Brownian Dynamics simulations based on the classical WLC model of DNA, that the probability of loop formation is enhanced more than 10 fold at $L \approx 40$nm when we go from $a = 0$ to $a = 10$nm. They also analyzed the effects of non-linearities such as, permanent bends in the DNA, and showed how these defects can greatly enhance looping probabilities and rate constants for contour lengths L in the interval $40\text{nm} < L < 100\text{nm}$ for various values of the span a. Merlitz *et al.* do not report results for lengths shorter than 40nm, but it would not be unreasonable to expect that to obtain high looping probabilities in this regime would require introduction of non-linearities in the DNA. However, this is exactly the regime where we have obtained a second peak and valley in the looping probabilities. In the light of this observation the significance of the results summarized in Fig. 7.5 is that high looping probabilities for short DNA contour lengths ($L < 40$nm) can be explained with the classical WLC model of DNA (without non-linearities such as kinks or permanent bends) if we account for the geometry of the looping protein. At these short contour lengths shape fluctuations make only a small contribution to the

free energy so that the peak in probability is simply a result of the low elastic bending energy required to satisfy the constraint on the end-to-end distance placed by the looping protein. In fact, the location of the well in the probability distribution between the two peaks (at $L \approx a$ and $L \approx 5\xi_p$) is strongly correlated with the length at which the elastic bending energy has a local maximum (see inset in Fig. 7.5).

The results summarized in Fig. 7.4 and 7.5 could also provide an alternative interpretation for the experimental results of Smith *et al.* [58]. In this experiment the probability of loop formation was measured as a function of the length of the loop for several enzymes which interact with DNA at two separate sites [58]. The main results of these experiments were that the probability distribution was different for different proteins and that looping at short contour lengths was far more probable than predicted by the WLC theory alone. The authors had also found two peaks in the probability distribution for looping by some proteins. Qualitatively similar observations in bulk experiments were made by Reuter *et al.* [142] who found that the propensity of cutting by certain two-site restriction enzymes (EcoRII) was peaked at two different contour lengths with the highest propensity occurring at the peak at short lengths. They had suggested that at short contour lengths the DNA is slightly bent to meet the constraints placed by the enzyme while at longer lengths it was looped. All of these observations are replicated in our model which accounts for the effects of protein size. A direct comparison of our results with those of Smith *et al.* [58] is not possible since our calculations have been carried out only in two dimensions whereas the experiments are fully three dimensional. Also, despite our results which rely solely on an elastic rod model of DNA the possibility of kink or hinge formation at high curvatures still remains open.

An important by-product of our MC simulations is that we have decomposed the fluctuating shapes of the loop into eigenmodes. Such a decomposition is possible when the fluctuations around equilibrium are small so that the energy of an arbitrary shape can be expressed as the sum of the energy of the equilibrium shape and a term that is quadratic in the small fluctuations. For the case of the DNA loop the shape can be written in terms of the angle $\theta(s)$ which is the angle made by the tangent to the loop to the positive x-axis. Fig. 7.3 shows the deviations in the shape of the loop and the angle $\delta\theta(s)$ as a function of the arc-length s. The first eigenmode (corresponding to the largest eigenvalue of covariance matrix) is shown together with comparison to an analytical result. The analytical calculation is performed in a slightly different context in which the force at the ends (as opposed to the end-to-end distance) as well as the angles made by the tangents at the ends are held fixed. Despite this difference in the boundary condition, the theory and simulations yield similar variation for the change in the tangent angle along the arc length of the DNA (see Figure 5, inset). Both the results show that the shape fluctuations are large in the regions of the

loop which are nearly straight (low curvature) and small in the highly curved regions. This would imply that the entropic contributions to the free energy of the loop have their origin in the low curvature regions. A similar conclusion was also reached by Fain *et. al.* [47] in their analysis of plectonemes in DNA where it was determined that most of the free energy of the plectonemes was elastic bending and twisting energy while the entropic part was always negligible. To the best of the authors' knowledge this is the first report on the fluctuating modes of a DNA loop subjected to clamped boundary conditions. Calculations such as these could be important building blocks for determining the free energies of binding/unbinding reactions of biological entities which have only recently been shown to depend strongly on configurational entropy.

Finally, from our DOSMC simulations, we have confirmed that expanding the potential energy of the DNA loop to quadratic order in fluctuations is a good approximation (see Fig. 7.6). The assumption of quasiharmonicity simplifies a variety of thermodynamic property calculations, the most prominent example being the entropy. Based on the conformational sampling of metropolis MC and its subsequent eigenvector decomposition, we can calculate the quasiharmonic configurational entropy of the DNA loop [10]. Furthermore, the DOS can be directly used to compute the free energy and entropy, quantities which are not directly available in conventional MC methods.

7.5 Conclusions

In this work we have summarized the effects of the size of the mediating protein on the propensity of loop formation in DNA. Many of the qualitative features observed in recent single molecule experiments on enzyme mediated DNA looping are reproduced by the WLC theory if we take into account the non-zero size of the looping enzyme. Two important effects that seem to directly depend on the size of the enzyme are that, (i) the overall propensity of loop formation at any given value of the DNA contour length increases with the size of the enzyme, and (ii) the contour length corresponding to the first peak as well as the first well in the probability density functions increases with the size of the enzyme. These qualitative features of the results can be readily tested by performing the looping experiments with looping proteins of known sizes. Also, of special interest are the eigenmodes of DNA fluctuations. Our theoretical calculations and MC simulations have shown that the fluctuations in the DNA are large where the curvature is small. Perhaps this observation can also be verified from experiments where real time motions of DNA are recorded [132]. Furthermore, we have shown the applicability of this coarse-grained model for DNA to other biological problems like determination of fluctuations in tension at the ends of DNA hairpin (see Appendix 7.6.2).

7.6 Appendix

7.6.1 Fluctuation operator

In order to visualize the fluctuations away from the equilibrium shape $\theta_{eq}(s)$ we vary the shape by $\delta\theta(s)$ and expand the following potential energy functional (see Eq. 7.13) characterizing a bent rod upto quadratic order in $\delta\theta(s)$.

$$E[\theta(s)] = \int_{-\frac{L}{2}}^{\frac{L}{2}} \frac{K_b}{2}\theta'^2 ds - \int_{-\frac{L}{2}}^{\frac{L}{2}} F\cos\theta ds. \tag{7.13}$$

The first term in the above potential energy is the elastic bending energy and the second term is the potential energy of the applied force F. We assume here that a known force F is applied at the ends of the loop. This is different from specifying a given end-to-end distance on the loop as a constraint as summarized by Eq. 7.4. In that case F should be interpreted as a Lagrange multiplier enforcing the constraint on the end-to-end distance. Here we will work with the case when the force F is specified since the mathematics in this situation is relatively simpler. We now wish to compute $\mathbf{T}$ which is the so-called 'fluctuation operator' and is given by

$$\delta E = E[\theta_{eq}(s) + \delta\theta(s)] - E[\theta_{eq}(s)] = \delta\theta\frac{\mathbf{T}}{2}\delta\theta. \tag{7.14}$$

Fortunately, this exercise has been carried out by Kulic *et al.* [91] who have shown that the fluctuation operator is given by

$$\frac{\sqrt{K_b F}}{k_B T}\mathbf{T} = \frac{\sqrt{K_b F}}{k_B T}\left(-\frac{\partial^2}{\partial t^2} + 2k^2\mathrm{sn}^2(t|k) - 1\right) \tag{7.15}$$

and $t = s/\lambda$ and the equilibrium shape of the loop is described by Eq. 7.5. We are interested in the eigenvalues ν_p and eigenfunctions $f_p(s)$ of this operator which satisfy

$$\mathbf{T}f_p = \nu_p f_p, \qquad f_p(\pm\frac{L}{2\lambda}) = 0. \tag{7.16}$$

The second condition is a result of requiring that $\delta\theta(\pm\frac{L}{2}) = 0$ which would be the case if the angle at the ends of the loop were constrained by a rigid protein. If on the other hand, the protein was flexible then we would require $\delta\theta'(\frac{L}{2}) = 0$ which leads to

$$\mathbf{T}f_p = \nu_p f_p, \qquad f_p'(\pm\frac{L}{2\lambda}) = 0. \tag{7.17}$$

Real numbers ν_p and corresponding functions $f_p(s)$ satisfying the equation $\mathbf{T}f_p = \nu_p f_p$ for the operator $\mathbf{T}$ given by Eq. 7.15 are known (see Kulic *et al.* [91]). The eigenvalues and corresponding

eigenfunctions are:

$$k^2 - 1 \quad \text{with eigenfunction} \quad \mathrm{dn}(t|k), \tag{7.18}$$

$$0 \quad \text{with eigenfunction} \quad \mathrm{cn}(t|k), \tag{7.19}$$

$$k^2 \quad \text{with eigenfunction} \quad \mathrm{sn}(t|k). \tag{7.20}$$

$\nu_p = 0$ and $f_p(s) = \mathrm{cn}(\frac{s}{\lambda}|k)$ satisfy the conditions summarized by Eq. 7.17. However, none of these eigenfunctions satisfy Eq. 7.16. But, fortunately the operator $\mathbf{T}$ also has a continuous spectrum apart from the discrete eigenvalues given above. The spectrum was determined as part of a one-dimensional problem in solid-state physics regarding the valence and conduction bands in solids [167]. The eigenvalues and eigenfunctions of the continuous spectrum are:

$$\nu_p = \frac{k^2}{\mathrm{cn}^2(t_p|\sqrt{1-k^2})}, \quad f_p(t) = \frac{H(t+it_p|k)}{\Theta(t|k)} \exp(-tZ(it_p|k)), \tag{7.21}$$

where $H(t|k)$,$\Theta(t|k)$ and $Z(t|k)$ are Jacobi's eta, theta and zeta functions and $-2K(\sqrt{1-k^2}) \leq t_p \leq 2K(\sqrt{1-k^2})$ and $K(k)$ is the complete elliptic integral of the first kind. The lower bound on the continuous spectrum of eigenvalues is obtained when $t_p = 0$ or $t_p = \pm 2K(\sqrt{1-k^2})$ resulting in $\nu_p = k^2$ which leads to the eigenfunctions $f_p(t) = C_1(k)\mathrm{sn}(\frac{\pi t}{2K(k)}|k)$ and $f_p(t) = C_2(k)\mathrm{sn}(\frac{\pi t}{2K(k)}|k)\cos(\frac{2\pi t}{K(k)})$ where $C_1(k)$ and $C_2(k)$ are real numbers that depend only on k. But, we note that the eigenvalue $\nu_p = k^2$ also has another eigenfunction $f_p(t) = \mathrm{sn}(t|k)$. In other words, the eigenspace corresponding to the eigenvalue k^2 is spanned by three eigenfunctions and we can satisfy the boundary condition that $\delta\theta(\frac{L}{2}) = 0$ by finding constants α and β such that

$$\mathrm{sn}(\frac{\pi L}{4\lambda K(k)}|k)\left(\alpha + \beta\cos(\frac{\pi L}{\lambda K(k)})\right) + \mathrm{sn}(\frac{L}{2\lambda}|k) = 0. \tag{7.22}$$

The required eigenfunction corresponding to eigenvalue k^2 is then simply a linear combination of these eigenfucntions:

$$f_p(s) = \alpha\mathrm{sn}(\frac{\pi s}{2\lambda K(k)}|k) + \beta\mathrm{sn}(\frac{\pi s}{2\lambda K(k)})\cos(\frac{2\pi s}{\lambda K(k)}) + \mathrm{sn}(\frac{s}{\lambda}|k). \tag{7.23}$$

7.6.2 Simulated distribution of tensions in the thermal dissociation of DNA hairpins

We model the ssDNA loop of the DNA hairpin as being inextensible and homogeneous in two-dimensional space (thus ignoring the twisting energy) with bending stiffness K_b, where K_b is related to the persistence length, ξ_p through the relation $\xi_p = K_b/k_BT$. In this work, we take ξ_p to be 1.4 nm [92] for ssDNA and temperature, T to be 300 K. The length per base pair of ssDNA is taken to be 0.63 nm [120]. To account for the thermal fluctuations of the DNA loop, we use a

Metropolis-based Monte Carlo method as described in section 7.3.2. We discretize the ssDNA into N rigid links, each of length Δs. Unless specified, the link length is taken to be 0.1 nm. A special care is taken to find the energy contribution of first and last link since the angle between the first link and the link before it, say 0^{th} link (and similarly angle between the last link and the following link, say $(N+1)^{th}$ link) is not simulated. In our model, we assume that 0^{th} link and $(N+1)^{th}$ link are always vertical.

Umbrella Sampling

We define a biasing potential U_b which is zero if $a_i \leq a \leq a_i + \Delta a$ and infinity elsewhere. We perform Monte-Carlo simulations as outlined in section 7.3.2 in different windows of a. In our simulation, we use eight windows with $\Delta a = 0.2$ nm and we set the overlap between neighboring windows to be 0.1 nm. For each window, we perform four billion MC steps to compute histogram of a, $P(a)$. At the end of the simulation, we translate $P(a)$ in each window such that the $P(a)$ in the overlap region match. From the overall $P(a)$ versus a graph, we calculate $W(a) = -k_B T \ln[P(a)]$ as the potential of mean force as a function of a. A second-order polynomial is fitted to $W(a)$ versus a data. Then, we compute the loop stiffness as:

$$k = \frac{\partial^2 W}{\partial a^2} \tag{7.24}$$

and the mean force as:

$$\langle F \rangle = -\frac{\partial W}{\partial a}|_{a=a_0} \tag{7.25}$$

where a_0 is the equilibrium distance between the loops and is taken to be 0.9 nm [45] (which is the phosphate-phosphate distance in the B-DNA). The standard deviation of the force distribution was then calculated as:

$$\sigma_F = \sqrt{k k_B T} \tag{7.26}$$

Conversion from 2D simulation to 3D simulation

We seek a simple scaling argument to convert $\langle F \rangle$ and σ_F obtained for a two-dimensional DNA loop to a three-dimensional loop. For a freely jointed chain (FJC) in two or three-dimensional space, the end-to-end distance, a, is related to the applied force, F, through $F = -ka$, where $k = k_B T d/Lb$ is the effective loop stiffness, b is the Kuhn length, L is the contour length and d is the dimensionality [21]. We rewrite $k = k_B T d/2L\xi_p$, where we have employed the relationship, $b = 2\xi_p$. Furthermore, the persistence length is dependent on the bending stiffness of the polymer, $\xi_p = 2K_b/k_B T$ in two-dimensions and $\xi_p = K_b/k_B T$ in three-dimensions. Hence, for simulations using the same value of bending stiffness for a polymer loop in two and three dimensions, the

loop stiffness scales as $k_{3D}/k_{2D} = 3$. Since $\sigma_F = \sqrt{kk_BT}$, we obtain $\sigma_{F,3D}/\sigma_{F,2D} = \sqrt{3}$ and $\langle F_{3D}\rangle/\langle F_{2D}\rangle = \sqrt{3}$. Table 7.1 summarizes our corrected σ_F. For the longest loops, the force fluctuations decrease with increasing loop length similar to the expectation for a freely jointed chain $\sigma_F = k_BT/\sqrt{bL}$.

Time Scale for Force Fluctuation

From the exercise in the above section, we obtain an estimate for the stiffness of the potential energy landscape of the hairpin loop along the coordinate a. For an overdamped Langevin equation of a harmonic oscillator, the characteristic time scale over which the position (and hence the force) becomes decorrelated is given as

$$\tau_F = \frac{\chi}{2k} \tag{7.27}$$

where χ is the friction coefficient. In the Rouse model for the polymer, the friction coefficient is assumed to be the sum of frictional coefficient of each monomer unit, $\chi = N\chi_1$, where we treat each monomer unit as a Stoke-Einstein sphere to obtain $\chi_1 = 6\pi\mu R$, where μ is the viscosity (10^{-4} Pa-s) and R is the hydrodynamic radius ($\Delta s/2$) of each monomer unit. So, we get

$$\tau_F = \frac{3N\pi\mu\Delta s}{2k}. \tag{7.28}$$

Run	L [nm]	k [N/m]	σ_F [pN]	$\langle F\rangle$ [pN]
1	2.0	0.059	15.6	28.5
2	2.6	0.075	17.6	20.4
3	2.6	0.071	17.2	19.0
4	3.3	0.046	13.8	23.2
5	6.0	0.010	6.4	10.0
6	6.0	0.011	6.6	9.9

Table 7.1: A second-order polynomial was fitted to the W(a) versus a data. The r^2 value for each fit was greater than 0.94. For a few cases, two independent simulations were performed with different random number seeds.

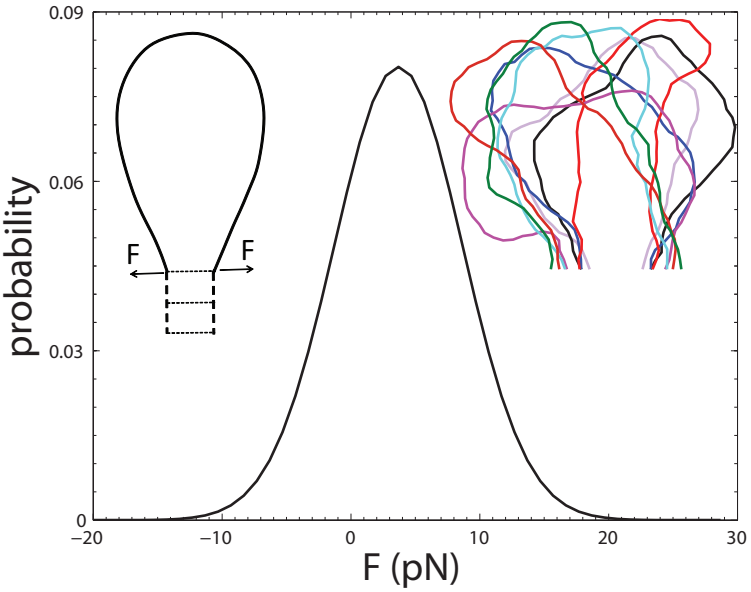

Figure 7.7: Semi-flexible polymer loops give rise to Gaussian fluctuating forces. The force, F, distribution at the loop-end for a 6 nm contour length ssDNA loop is shown, as obtained by Monte-Carlo technique. The left inset depicts a cartoon of the DNA hairpin. The force acting along the loop-ends is taken to be positive if it increases the loop-ends separation. The right inset depicts snapshots of the loop's thermal fluctuations.

Chapter 8

Conclusions and Future Directions

The primary aim of this work was to develop a minimalistic model for the endocytosis and compute the bioenergetics of membrane deformation during the process of endocytosis. Endocytosis is a highly complex process involving an orchestration of plethora of proteins. Though recent experiments have shed some light on the possible roles of various proteins involved in this process, a detailed mechanistic model of endocytosis has been lacking. We have presented a compact bioenergetic model which imposes the correct thermodynamic constraints on the process of vesicle nucleation in endocytosis, as well as quantitatively explains several experimental observations on the process of vesicle nucleation induced by the clathrin-coated assembly prior to vesicle scission in mammalian cells. In this work, we have restricted our analysis to the membrane budding and have not included the step of membrane vesicle pinch-off from the mother bilayer.

Broadly, the endocytic proteins can be classified into three categories: (i) Cargo protein (ii) Adaptor proteins that play a role in recruiting various endocytic proteins to the endocytic vesicle and (iii) Curvature inducers. A single protein can often fall into multiple categories. For example, epsin has the capability to induce and recognize curvature in the membrane however, it can also serve as an adaptor protein through its various motifs. A comprehensive network model of endocytosis is a topic of high interest however it requires a detailed biochemical knowledge of protein-protein and protein-membrane interaction along with the three-dimensional structure of the proteins. In lack of this data, we have adopted a biophysical philosophy that a minimalistic endocytosis model should be able to delineate the role played by these proteins if we balance for the free energy of membrane deformation by protein-protein and protein-membrane interactions.

Accordingly, we formulate a minimalistic model, by restricting our focus to three proteins: clathrin, epsin and AP-2, and their role in the nucleation of a vesicle bud on the cell membrane.

Mammalian cells have a diverse set of proteins which often serve as surrogates and participate in compensatory mechanisms. In this regard, our choice of the endocytic accessory proteins for the ingredients for the minimal model represents the roles for the scaffolding proteins (clathrin), curvature inducing proteins (epsin) and the adaptor proteins (AP-2). We employ field-theoretic simulation methodologies to address how the energetics of vesicle formation in a membrane is stabilized by the presence of the endocytic proteins.

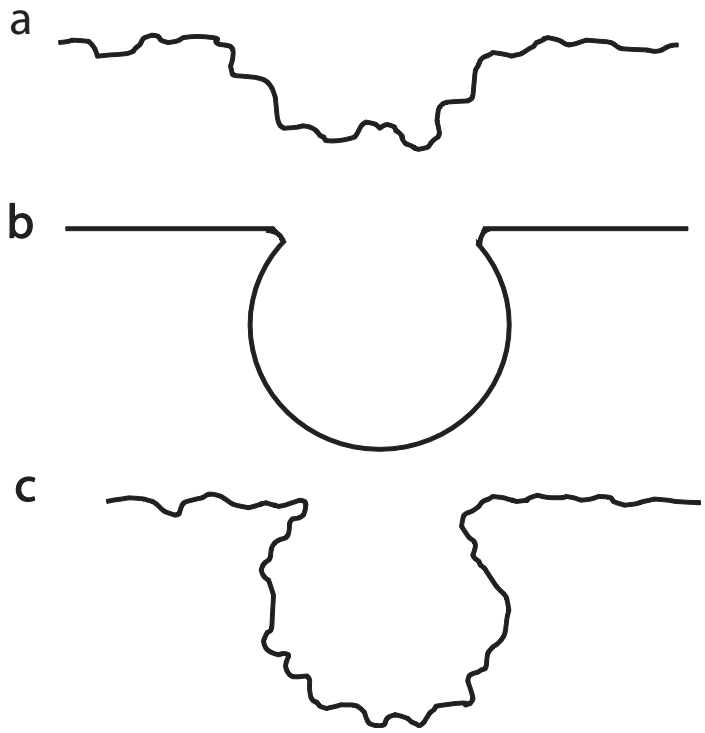

Figure 8.1: A schematic of membrane profiles that can be obtained by (a) Monge (b) Surface evolution and (c) Local Coordinate formalisms.

A multitude of models are available to model membrane deformation from nanoscale to microscale (see Fig. 2.1). Since the process of endocytosis happens at the microscale, we used generalized elasticity model of the membrane as proposed by Helfrich. Role of curvature inducing proteins can be also accounted for in the Helfrich model through a spontaneous curvature function which can be, in general, a function of both time and spatial coordinates along with type of protein and its density. Solving the Helfrich Hamiltonian exactly poses great challenge and hence, we develop few novel techniques to solve this Hamiltonian in various limiting cases (see Fig. 8.1). Monge formalism can depict membrane deformation due to curvature inducing proteins when the membrane deformation is small. This formalism can account for the role of temperature and diffusion

of curvature inducers in the membrane deformation (see section 2.3 for more details). Surface of evolution formalism allows to study large membrane deformations but only under a critical assumption of axial symmetry. This precludes the study of temperature and protein-diffusion effects (see section 2.4 for more details). Realizing that to study the process of endocytosis from the nucleation to the bud maturation stage, one needs to account for the temperature, protein-diffusion and large membrane deformation, we propose an alternative formalism of local TDGL (see section 8.1 for more details).

Using Monge TDGL to study membrane deformation when the curvature inducing proteins (epsin) can diffuse on the membrane, we observe a rich phase behavior of cooperativity in membrane deformation and protein localization. We observe that positional and orientational ordering of these proteins depend on protein density and (magnitude and range of) protein induced curvature. The state diagram depicts two regimes showing nucleation of vesicle-buds via distinct mechanisms (nucleation via orientational ordering and nucleation cooperativity), the regime showing repressed undulations of the membrane at high protein density (repressed undulation), and an intervening regime showing no nucleation with only regular thermal undulations in the membrane. The emerging potential of mean-force between two epsins on the membrane surface highlights a competition between energetic repulsion and entropic attraction. The spontaneous positional and orientational ordering of epsins (in general of any diffusing curvature inducer) resulting in a membrane invagination can be a key to the clathrin-independent endocytosis.

We capture the complete energetics of membrane deformation from the early stage to the mature bud stage using surface of evolution approach. We model the curvature induced by clathrin assembly (i.e. clathrin cage along with epsin and AP2) as a constant curvature field over a small region of the membrane. We argue that the membrane deformation energy of about 500 k_BT to form a mature bud is compensated by various protein-membrane interactions. The energetic stabilization provided by clathrin polymerization is not sufficient to stabilize the membrane bud. We demonstrate that if sufficient number of epsins are incorporated into the membrane bud, the resulting energetic stabilization can overcome the membrane bending energy penalty. The number of epsins in a given size of membrane bud are estimated based on the number of vertices in the clathrin cage; with the assumption that an epsin binding site on the clathrin is localized at the vertices of clathrin cage. We use this simplistic model to explain a recent experiment performed in neuronal cells which reports that by inhibiting clathrin-epsin interaction, more synaptic vesicles get trapped in the initial stages of bud growth as opposed to the wild-type cells where the number of vesicles increases almost exponentially with the progression of the bud-growth.

Since the surface of evolution approach does not account for the change in membrane entropy as

membrane deforms, we use thermodynamics integration (TI) technique to compute the membrane free energy as the membrane deforms due to increasing spatial extent of clathrin coat. Our results indicate that change in entropy plays a minor role in determining membrane free energy change when the membrane deforms. Fourier transformation of the membrane Hamiltonian shows that the membrane fluctuation modes are not independent in the Fourier space when a curvature inducing protein is present. Hence a special care should be taken while interpreting the experimentally observed membrane height fluctuations of a curved membrane. Furthermore, the Fourier decomposition reiterates the fact that membrane bending rigidity increases in the vicinity of curvature inducing proteins thus possibly reducing the thermal fluctuations of the membrane in the vicinity of curvature inducing proteins.

8.1 Extension: Local Coordinate Formalism

Under conditions of extreme curvature, overhangs appear in the cell membrane. This necessitates a fundamentally different approach from Monge formalism to compute the cell membrane shapes and associated energies under conditions of extreme curvature.

Under these conditions of extreme curvature, the Monge formalism (see section 2.3) cannot be used since the formation of overhangs precludes the description of the membrane as the graph of a function $z = F(x, y)$. This forces us to consider a local gauge approach to compute membrane shapes. Keeping the same membrane description as a surface S embedded in 3-dimensional Euclidean space with global coordinates x, y, z, we introduce a local scheme as follows. Fundamental results from the theory of surfaces in differential geometry tell us that around any point p on S, there exists a coordinate neighborhood which we denote by S_p such that S_p can be described as the graph of a function. We now claim that with this description, we can obtain the local free energy of the patch S_p. Let $(\vec{I}, \vec{J}, \vec{K})$ be an orthogonal coordinate system with coordinates $\{u, v, w\}$ centered at p with $\vec{K}$ pointing in the direction of the unit normal N_p to S_p at p. Then as noted above, in the local coordinates $\{u, v, w\}$, the patch S_p can be written as the graph of the function $w = g(u, v)$.

Let R be the projection of the graph of $w = g(u, v)$ onto the $u - v$ plane. We proceed as in the global Monge gauge. We consider a partition of the domain R in the $u - v$ plane by subrectangles R_{ij} which induces a partition on the local patch S_p in the form of $g(R_{ij})$. Again we let $\hat{A}_{ij}$ be the projection of $g(R_{ij})$ onto the tangent space and $A_{flat\ ij} = \Delta u \Delta v$. Then the area of the projection of $g(R_{ij})$ onto the tangent space is:

$$\hat{A}_{ij} = \frac{A_{flat,\ ij} |\nabla g - \vec{K}|}{|(\nabla g - \vec{K}) \cdot \vec{K}|} \tag{8.1}$$

where $\vec{K}$ is the normal to the $u-v$ plane. Simplifying the expression for $\hat{A}_{ij}$, we obtain the following:

$$\hat{A}_{ij} = A_{flat,\ ij}[1 + (\nabla g)^2]^{\frac{1}{2}} \tag{8.2}$$

Hence the contributions to the free energy E_{ij} of a membrane patch $g(R_{ij})$ due to mean curvature and Gaussian curvature are given below as:

$$E_{bend,\ ij} = \frac{\kappa \Delta u \Delta v}{2}[1 + (\nabla g)^2]^{\frac{1}{2}}[H - H_o]^2 \tag{8.3}$$

$$E_{Gauss,\ ij} = \overline{\kappa} K[1 + (\nabla g)^2]^{\frac{1}{2}} \Delta u \Delta v \tag{8.4}$$

To calculate the contribution due to frame energy we need to be careful. We recall that the frame energy contribution arises because the membrane is part of some larger system. Using the approximation $\hat{A_{ij}}$ to the membrane domain patch $g(R_{ij})$ with area A_{ij}, the frame energy of a patch $g(R_{ij})$ of the local membrane S_p is given by:

$$E_{frame} = \sigma(\hat{A_{ij}} - A^o_{flat,ij}) \tag{8.5}$$

σ is the frame tension and $A^o_{flat,ij}$ is the projected area of the membrane domain area $\hat{A_{ij}}$ onto the $x-y$ plane (not onto the $u-v$ plane). This is because frame energy arises as a result of membrane deformation from the global flat state. We now express the membrane patch S_p as the zero level set of the function $h(u,v) = g(u,v) - w$. The normal vector at the point p is then given by $\nabla g - \vec{K}$. The projected area $A^o_{flat,ij}$ of the membrane domain area $\hat{A_{ij}}$ onto the $x-y$ plane is expressed as:

$$A^o_{flat,ij} = \hat{A_{ij}} \frac{|(\nabla g - \vec{K}) \cdot \vec{k}|}{|\nabla g - \vec{K}|} \tag{8.6}$$

We now define the following transformation between the coordinates $(\vec{I}, \vec{J}, \vec{K})$ and the global coordinates $(\vec{i}, \vec{j}, \vec{k})$:

$$\vec{I} = a_1\vec{i} + a_2\vec{j} + a_3\vec{k} \tag{8.7}$$

$$\vec{J} = b_1\vec{i} + b_2\vec{j} + b_3\vec{k} \tag{8.8}$$

$$\vec{K} = c_1\vec{i} + c_2\vec{j} + c_3\vec{k} \tag{8.9}$$

With this transformation,

$$\nabla g - \vec{K} = (g_u a_1 + g_v b_1 - c_1)\vec{i} + (g_u a_2 + g_v b_2 - c_2)\vec{j} + (g_u a_3 + g_v b_3 - c_3)\vec{k} \tag{8.10}$$

Hence $(\nabla g - \vec{K}) \cdot \vec{k} = (g_u a_3 + g_v b_3 - c_3)$. We then have:

$$A^o_{flat,ij} = \hat{A_{ij}} \frac{|g_u a_3 + g_v b_3 - c_3|}{[1 + (\nabla g)^2]^{\frac{1}{2}}} \tag{8.11}$$

Substituting $\hat{A}_{ij} = A_{flat,\ ij}[1 + (\nabla g)^2]^{\frac{1}{2}}$ into the expression above, we obtain the following:

$$A^o_{flat,ij} = A_{flat,\ ij}[1 + (\nabla g)^2]^{\frac{1}{2}} \frac{|g_u a_3 + g_v b_3 - c_3|}{[1 + (\nabla g)^2]^{\frac{1}{2}}} \tag{8.12}$$

which further simplifies to

$$A^o_{flat,ij} = |g_u a_3 + g_v b_3 - c_3| A_{flat,\ ij} \tag{8.13}$$

The frame energy finally takes the form

$$E_{frame} = \sigma A_{flat,\ ij}([1 + (\nabla g)^2]^{\frac{1}{2}} - |g_u a_3 + g_v b_3 - c_3|) \tag{8.14}$$

Using the approximation $[1 + (\nabla g)^2]^{\frac{1}{2}} \approx [1 + \frac{1}{2}(\nabla g)^2]$, the frame energy has the form:

$$E_{frame} = \sigma A_{flat,\ ij}(1 + \frac{1}{2}(\nabla g)^2 - |g_u a_3 + g_v b_3 - c_3|) \tag{8.15}$$

The total local energy E of the membrane patch S_p is given by

$$E = \sum_{i,j} E_{bending,\ ij} + E_{Gauss,\ ij} + E_{frame,\ ij} \tag{8.16}$$

$$= \sum_{i,j} \left(\left(1 + (\nabla g_{ij})^2\right)^{\frac{1}{2}} \left(\frac{\kappa}{2} [H_{ij} - H_{o,\ ij}]^2 + \overline{\kappa} K_{ij} \right) + \sigma \left(1 + \frac{1}{2}(\nabla g)^2 - |g_u a_3 + g_v b_3 - c_3| \right) \right) \Delta u \Delta v \tag{8.17}$$

Where $\nabla g_{ij},\ H_{ij},\ H_{o,\ ij}$ are evaluated at (u_i^*, v_j^*) in R. Taking finer and finer partitions, the Riemann sum becomes the integral:

$$E = \int\int_R \frac{\kappa}{2}[1+(\nabla g)^2]^{\frac{1}{2}}[H-H_o]^2 + \sigma(1+\frac{1}{2}(\nabla g)^2 - |g_u a_3 + g_v b_3 - c_3|) + \overline{\kappa} K[1+(\nabla g)^2]^{\frac{1}{2}} du dv \tag{8.18}$$

Repeating the same approximations as in the global case but replacing F by g, we have that the local free energy E is:

$$E = \int\int_R \frac{\kappa}{2}[\nabla^2 g - H_o]^2 + (\frac{\kappa}{4} H_o^2 + \frac{\sigma}{2})(\nabla g)^2 + \sigma(1 - |g_u a_3 + g_v b_3 - c_3|) + \overline{\kappa}(g_{uu} g_{vv} - g_{uv}^2) du dv \tag{8.19}$$

Applying the variational derivative $\frac{\delta E}{\delta g}$ to the above energy functional and noting that the variational derivative of the term $\int\int_R \sigma(1 - |g_u a_3 + g_v b_3 - c_3|) du dv$ in (8.19) is zero, we obtain locally the Ginzburg-Landau equation for a topologically invariant transformation given in terms of the coordinates (u, v, w) as:

$$\begin{aligned} \frac{1}{M}\frac{\partial g}{\partial t} =& H_o \kappa \left(g_u H_{o,u} + g_v H_{o,v}\right) + \left(\frac{\kappa}{2} H_o^2 + \sigma\right)\left(g_{uu} + g_{vv}\right) \\ & - \kappa \left(g_{uuuu} + g_{vvvv} + 2 g_{uuvv}\right) + \kappa \left(H_{o,uu} + H_{o,vv}\right) \end{aligned} \tag{8.20}$$

8.1.1 Numerical Solution

In the local coordinate scheme, the grid sizes changes with the evolution of the membrane. This results in the need to develop a nonhomogeneous central difference scheme to model membrane dynamics. We recall that a general Taylor series is given by (see Eq. 2.34):

$$F(x+h) = \sum_{k=0}^{\infty} \frac{h^k}{k!} F^k(x) \tag{8.21}$$

We want to obtain a central difference approximation of order 2 for first order, second order, and fourth order derivatives for a nonhomogeneous grid size. For a central difference approximation of $F^{(1)}(x)$ of order 2, we rewrite $F(x+h)$ as:

$$F(x+h) = F(x) + hF^{(1)}(x) + \frac{h^2}{2} F^{(2)} + \bigcirc(h^2) \tag{8.22}$$

and then solve the equation

$$C_1 F(x+h_1) + C_2 F(x) + C_3 F(x-h_2) = F^{(1)}(x) \tag{8.23}$$

Equating similar terms, this results in the following system of equations to find C_1, C_2, C_3

$$\begin{bmatrix} 1 & 1 & 1 \\ h_1 & 0 & -h_2 \\ \frac{h_1^2}{2} & 0 & \frac{h_2^2}{2} \end{bmatrix} \begin{bmatrix} C_1 \\ C_2 \\ C_3 \end{bmatrix} = \begin{bmatrix} 0 \\ 1 \\ 0 \end{bmatrix} \tag{8.24}$$

Second order central difference approximations of F of order 2 are obtained in the same spirit by solving the equation

$$C_1 F(x+h_1) + C_2 F(x) + C_3 F(x-h_2) = F^{(2)}(x). \tag{8.25}$$

which leads to the following matrix characterization of C_1, C_2, C_3

$$\begin{bmatrix} 1 & 1 & 1 \\ h_1 & 0 & -h_2 \\ \frac{h_1^2}{2} & 0 & \frac{h_2^2}{2} \end{bmatrix} \begin{bmatrix} C_1 \\ C_2 \\ C_3 \end{bmatrix} = \begin{bmatrix} 0 \\ 0 \\ 1 \end{bmatrix} \tag{8.26}$$

Central difference approximation for $F^4(x)$ of order 2 can be written as:

$$C_1 F(x+h_1) + C_2 F(x+h_2) + C_3 F(x) + C_4 F(x-h_3) + C_5 F(x-h_4) = F^{(4)}(x). \tag{8.27}$$

which leads to the following matrix:

$$\begin{bmatrix} 1 & 1 & 1 & 1 & 1 \\ h_1 & h_2 & 0 & -h_3 & -h_4 \\ \frac{h_1^2}{2} & \frac{h_2^2}{2} & 0 & \frac{h_3^2}{2} & \frac{h_4^2}{2} \\ \frac{h_1^3}{3!} & \frac{h_2^3}{3!} & 0 & \frac{-h_3^3}{3!} & \frac{-h_4^3}{3!} \\ \frac{h_1^4}{4!} & \frac{h_2^4}{4!} & 0 & \frac{h_3^4}{4!} & \frac{h_4^4}{4!} \end{bmatrix} \begin{bmatrix} C_1 \\ C_2 \\ C_3 \\ C_4 \\ C_5 \end{bmatrix} = \begin{bmatrix} 0 \\ 0 \\ 0 \\ 0 \\ 1 \end{bmatrix} \tag{8.28}$$

We obtain mixed order partial derivative central difference approximations of order 2 for z_{xxyy} as done in the homogeneous case (see Sec. 2.3.2).

$$\begin{aligned} z_{xxyy} = &\Big[C_1(D_1 z_{i-2} + D_2 z_{i-1} + D_3 z_i + D_4 z_{i+1} + D_5 z_{i+2})_{j-1} \\ &+ C_2(D_1 z_{i-2} + D_2 z_{i-1} + D_3 z_i + D_4 z_{i+1} + D_5 z_{i+2})_j \\ &+ C_3(D_1 z_{i-2} + D_2 z_{i-1} + D_3 z_i + D_4 z_{i+1} + D_5 z_{i+2})_{j+1}\Big] + \bigcirc(h^2) \end{aligned} \tag{8.29}$$

The C_1, C_2, C_3 as obtained in (8.26) are computed along the y axis and D_1, D_2, D_3, D_4, D_5 are obtained through following matrix equation:

$$\begin{bmatrix} 1 & 1 & 1 & 1 & 1 \\ h_1 & h_2 & 0 & -h_3 & -h_4 \\ \frac{h_1^2}{2} & \frac{h_2^2}{2} & 0 & \frac{h_3^2}{2} & \frac{h_4^2}{2} \\ \frac{h_1^3}{3!} & \frac{h_2^3}{3!} & 0 & \frac{-h_3^3}{3!} & \frac{-h_4^3}{3!} \\ \frac{h_1^4}{4!} & \frac{h_2^4}{4!} & 0 & \frac{h_3^4}{4!} & \frac{h_4^4}{4!} \end{bmatrix} \begin{bmatrix} D_1 \\ D_2 \\ D_3 \\ D_4 \\ D_5 \end{bmatrix} = \begin{bmatrix} 0 \\ 0 \\ 1 \\ 0 \\ 0 \end{bmatrix} \tag{8.30}$$

The spatial derivatives of the spontaneous curvature function are calculated in the similar fashion. The Eq. 8.20 is then solved using Explicit scheme in time as done in Eq. 2.39.

This discretized equation is applied to the solution of our membrane deformation problem as follows. Let S be a differentiable surface embedded in 3-dimensional Euclidean space, then for any point $p \in S$, there exists a coordinate neighborhood S_p on S such that S_p can be written as the graph of a function $z = F(x, y)$ [25].

We use the above theorem to numerically solve the membrane evolution problem. We start with a rectangular grid on the region D occupied by the membrane. At each time step, we consider a point $p = (x, y, z)$ and the neighboring points to it. These points together with p will constitute the lattice approximation to the coordinate neighborhood S_p. We solve the membrane evolution equation, Eq. 8.20 in a coordinate system (x', y', z') defined by finding the plane of best fit to the 5 points and expressing these points in the coordinates (x', y', z') specified by the plane. The solution then obtained is then reexpressed in the old coordinates (x, y, z). This process is repeated for each point p at every time step.

Determination of Local Coordinate System

We outline a description of the transformation matrix that transforms (x, y, z) coordinates to (x', y', z') for the grid-point (m,mm). We construct a vector $\vec{A}$ such that grid-points immediately to the left and righ of (m,mm) lie on this vector. We also construct another vector $\vec{B}$ such that grid-points immediately to the left and above (m,mm) lie on this vector. Vector $\vec{P}$ is obtained as

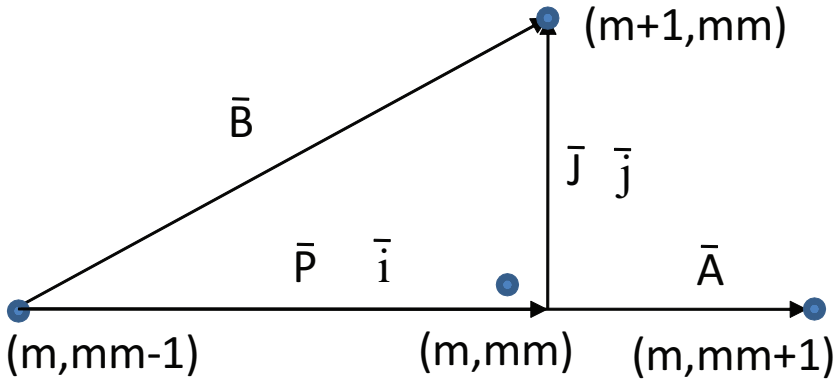

Figure 8.2: A schematic outlining the procedure used to determine local coordinate system a grid-point (m,mm).

the projection of $\vec{B}$ onto $\vec{A}$.

$$\vec{P} = \frac{\vec{A} \cdot \vec{B}}{|\vec{A}|^2} \vec{A} \tag{8.31}$$

$\vec{i}$ and $\vec{j}$ are unit vectors along $\vec{P}$ and $\vec{B} - \vec{P}$ respectively. A vector, $\vec{k}$ normal to both $\vec{i}$ and $\vec{j}$ is obtained as:

$$\vec{k} = \vec{i} \times \vec{j} \tag{8.32}$$

The vectors $\vec{i}, \vec{j}, \vec{k}$ constitute the local coordinate system for the grid-point (m,mm).

Alternatively, a set of two orthogonal vectors can be fitted to the four nearest neighbors of the grid-point (m,mm) and subsequently a vector normal to both of these vectors can be found. This route of calculating local coordinate system is more accurate but it also more computing-intesive, and thus was not implemented in this work. However, in future, the C++ code can be easily modified to incorporate this procedure.

Preliminary Results

Using a spontaneous curvature function of the form $H_0 = \nabla^2 \left(C_0 \exp\left[-r^2/2R_0^2\right] \right)$ where r is the distance from the origin, we generate resulting membrane deformation profiles. For this choice of spontaneous curvature function, it can be easily shown that for an infinite membrane, the membrane deformation at equilibrium is given as $z = C_0 \exp\left[-r^2/2R_0^2\right]$. Left panel of Fig. 8.3 shows a good agreement between the membrane deformation profiles as predicted by Monge and local-TDGL formalisms for small value of spontaneous curvature, i.e. $C_0 = 10$ 1/nm and $R_0 = 100.0$ nm. However, for larger value of spontaneous curvature, i.e. $C_0 = 50$ 1/nm and $R_0 = 100.0$ nm, membrane deformation predicted by local-TDGL matches better with the exact results. Note that

the disagreement between local-TDGL and exact result near the boundary of the membrane is due to different boundary conditions employed for solving the respective equations.

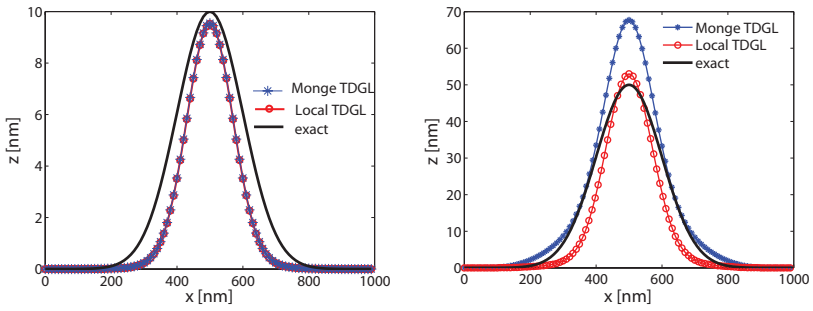

Figure 8.3: Comparison of membrane deformation profile calculated using Monge-TDGL and local-TDGL. For Monge and local TDGL, the results are obtained using pinned boundary conditions on $1 \times 1 \mu m^2$ membrane patch while exact results are obtained for an infinite membrane. Left panel: $C_0 = 10$ 1/nm and $R_0 = 100.0$ nm Right panel: $C_0 = 50$ 1/nm and $R_0 = 100.0$ nm.

8.2 Extension: Membrane dynamics in a fluid medium

Cell membrane dynamics in vivo occurs in a fluid medium. Our previous analysis studied dynamics phenomenologically without considering the effects of the medium on the dynamics of the membrane. In this section, we seek to develop a formalism to study the effects that fluids exert on cell membranes.

The equations of motion that determine the dynamics of cell membranes in a fluid medium can be developed by a recourse to the hydrodynamics equation. We make the assumption that the fluid is incompressible and can be described by Newtonian viscosity. Then the ambient fluid hydrodynamics is described by Navier-Stokes equation along with the fluid continuity equation.

$$\begin{aligned} \rho(\partial_t \mathbf{v} + (\mathbf{v} \cdot \nabla)\mathbf{v}) &= -\nabla p + \eta \nabla^2 \mathbf{v} + \mathbf{f}(\mathbf{r}) \\ \nabla \cdot \mathbf{v} &= 0 \end{aligned} \tag{8.33}$$

where $\mathbf{v}(\mathbf{r})$ is the velocity of the fluid, ρ, η are the density and the dynamic viscosity respectively of ambient fluid and $\mathbf{p}$ is the pressure. $\mathbf{f}(\mathbf{r})$ is the (body) force density acting on the fluid. Membrane dynamics occurs is in the low Reynolds number domain [100]. This allows us to linearize the Navier-Stokes equation by ignoring the left hand side of the Eq. 8.33. Hence the Navier-Stokes

equation reduces to

$$\nabla p - \eta \nabla^2 \mathbf{v} = \mathbf{f}(\mathbf{r}) \tag{8.34}$$

$$\nabla \cdot \mathbf{v} = 0 \tag{8.35}$$

We solve the linearized Navier-Stokes equation via a Fourier trasform [38,101]. The solution depends on the boundary condition. We specify that membrane lies in an infinite fluid which implies that $\mathbf{v} = 0$ far from the membrane. At the membrane surface, we use no-slip boundary condition. This results into:

$$\mathbf{v}(\mathbf{r}) = \int \Lambda(\mathbf{r} - \mathbf{r}') \cdot \mathbf{f}(\mathbf{r}') d\mathbf{r}' \tag{8.36}$$

where $\Lambda(\mathbf{r})$ is the Oseen tensor [38]:

$$\Lambda(\mathbf{r}) = \frac{1}{8\pi\eta r}(\mathbf{I} + \hat{r}\hat{r}), \tag{8.37}$$

$\mathbf{I}$ is the identity matrix and $\hat{r}$ is the unit vector parallel to position vector $\mathbf{r}$. We can interpret the Eq. 8.36 as the convolution of Oseen tensor with the force vector. Within the Monge formalism, the force acts on the membrane in the z direction only and is given by $-\frac{\delta E}{\delta z}$ and $\mathbf{r} = (x, y)$. Thus the equation of motion for the membrane in the ambient fluid takes the following form

$$\frac{dz(\mathbf{r}, t)}{dt} = -\int_A \Lambda(\mathbf{r} - \mathbf{r}') \frac{\delta E[z(\mathbf{r}', t)]}{\delta z(\mathbf{r}', t)} \, d^2\mathbf{r}' + \xi(\mathbf{r}, t) \tag{8.38}$$

where $\xi(\mathbf{r}, t)$ is the noise term satisfying fluctuation-dissipation theorem. We now derive an expression for this noise term. Towards this end, we consider a simplified form of the Hamiltonian given by Eq. 2.20:

$$E = \int_A \frac{\kappa}{2}[\nabla^2 z(\mathbf{r})]^2 + \frac{\sigma}{2}[\nabla z(\mathbf{r})]^2 \, d^2\mathbf{r} \tag{8.39}$$

Applying the following Fourier transform

$$z(\mathbf{k}, t) = \int_A z(\mathbf{r}, t) e^{-i\mathbf{k}.\mathbf{r}} \, d^2\mathbf{r} \tag{8.40}$$

to the equation of membrane motion (Eq. 8.38), we get

$$\frac{\partial z(\mathbf{k}, t)}{\partial t} = -\Lambda(\mathbf{k})(\kappa k^4 + \sigma k^2) z(\mathbf{k}, t) + \xi(\mathbf{k}, t) \tag{8.41}$$

where $\Lambda(\mathbf{k})$ is the Fourier transform of Oseen tensor and is given as

$$\Lambda(\mathbf{k}) = \frac{1}{4\eta k} \tag{8.42}$$

It is worthwhile to point out that mode $k = 0$ leads to divergence of Eq. 8.41. This mode can be neglected since it represents overall translation of the membrane. Let $\omega(\mathbf{k}) = \Lambda(\mathbf{k})(\kappa k^4 + \sigma k^2)$ we get

$$\frac{\partial z(\mathbf{k}, t)}{\partial t} = -\omega(\mathbf{k}) z(\mathbf{k}, t) + \xi(\mathbf{k}, t) \tag{8.43}$$

Solution of this non-homogeneous ordinary differential equation (8.43) gives

$$z(\mathbf{k},t) = z(\mathbf{k},0)e^{-\omega(\mathbf{k})t} - e^{-\omega(\mathbf{k})t}\int_0^t e^{-\omega(\mathbf{k})t'}\,\xi(\mathbf{k},t')\,dt' \tag{8.44}$$

For the random term, we assume following two properties [170]:

$$\langle \xi(\mathbf{k},t)\rangle = 0 \tag{8.45}$$

$$\langle \xi(\mathbf{k},t)\xi(\mathbf{k}',t')\rangle = \Gamma\delta_{\mathbf{k},-\mathbf{k}'}\delta(t-t') \tag{8.46}$$

where Γ is an unknown constant. With the above assumptions and knowing that $\langle z(\mathbf{k},0)\xi(\mathbf{k},t)\rangle = 0$, $\langle z(\mathbf{k},t)z(\mathbf{k}',t')\rangle$ becomes

$$\langle z(\mathbf{k},t)z(\mathbf{k}',t')\rangle = z^2(\mathbf{k},0)e^{-2\omega(\mathbf{k})t} + \frac{\Gamma}{2\omega}\delta_{\mathbf{k},-\mathbf{k}'}\left(1-e^{-2\omega t}\right) \tag{8.47}$$

At very large time limit, the above equation reduces to

$$\langle z(\mathbf{k},t)z(\mathbf{k}',t')\rangle = \frac{\Gamma}{2\Lambda(\mathbf{k})(\kappa k^4+\sigma k^2)}\delta_{\mathbf{k},-\mathbf{k}'} \tag{8.48}$$

The membrane Hamiltonian (see Eq. 8.39) in Fourier space can be written as:

$$E = \frac{1}{2A}\sum_{\mathbf{k}}\left(\kappa k^4+\sigma k^2\right)\langle z(\mathbf{k})z(\mathbf{k}')\rangle \tag{8.49}$$

where A is the area of the membrane patch under study. As the energy is quadratic in $|z_{\mathbf{k}}|$, by the Equipartition theorem [26], energy of each mode is $k_BT/2$. Equating it to above expression for energy leads to

$$\langle z(\mathbf{k})z(\mathbf{k}')\rangle = \frac{k_BTA}{\kappa k^4+\sigma k^2} \tag{8.50}$$

Equating $\langle z(\mathbf{k})z(\mathbf{k}')\rangle$ from Eq. 8.48 and from Eq. 8.50, we get

$$\Gamma = 2k_BTA\Lambda(\mathbf{k}) \tag{8.51}$$

To summarize, the noise term is completely specified by following two properties

$$\langle \xi(\mathbf{k},t)\rangle = 0 \tag{8.52}$$

$$\langle \xi(\mathbf{k},t)\xi(\mathbf{k}',t')\rangle = 2k_BTA\Lambda(\mathbf{k})\delta_{\mathbf{k},-\mathbf{k}'}\delta(t-t') \tag{8.53}$$

Note that in Fourier space, ξ has both real (r) and imaginary (c) part. We write $\xi = r + ic$ where $i = \sqrt{-1}$. When $k' = -k$, $r(k) + ic(k) = r(-k) - ic(-k)$ leads to

$$\langle r(k,t)r(k,t')\rangle + \langle c(k,t)c(k,t')\rangle = 2\kappa_BTA\Lambda(\mathbf{k})\delta(t-t') \tag{8.54}$$

Hence, when the mode is purely real, random term is drawn from a Gaussian distribution with a variance of $2\kappa_BTA\Lambda(\mathbf{k})\delta(t-t')$, while for all other modes, both real and imaginary part are drawn from a Gaussian distribution with variance $\kappa_BTA\Lambda(\mathbf{k})\delta(t-t')$.

For a cell, viscosities in the cytoplasmic domain and extracellular domain differ by about factor of 6. Lin et. al. [101] has derived a general expression showing that average viscosity should be used Oseen tensor in such cases. As a further extension, they have also derived an expression to account for the finite extent of fluid. Qualitatively, the general effect of the wall near a fluctuating cell membrane is to slow down the relaxation of the membrane.

8.2.1 Method Implementation and Validation

The numerical solution of Eq. 8.38 closely follows the procedure outlined in section 2.3.2. However, there are few key difference to implement the Oseen tensor. It is easier to perform the integration (convolution) on the right-hand side of Eq. 8.38 in Fourier space since the convolution of two functions becomes multiplication of the functions in Fourier space. We numerically compute force, $F(\mathbf{r}', t) = -\frac{\delta E}{\delta z}$in real space on each grid point of the membrane using the explicit Euler scheme, at a given time, t (see section 2.3.2). The (discrete) Fourier transform of $F(\mathbf{r}', t)$ is then multiplied by Fourier transform of the Oseen term, and the contribution of random term is added. Note that the $k = 0$ mode leads to divergence of the equations since it represents a rigid body translation of the membrane. Hence, $k = 0$ mode is neglected in our calculations. Then the Fourier invertion results in the membrane configuration at the next time interval.

For thermal undulations in the membrane, the normalized height-heigth autocorrelation is given as [100]:

$$\frac{\langle z(t+\tau)z(t)\rangle}{\langle z^2\rangle} = \frac{\sum_k e^{-\omega_k t}\left(\kappa k^4 + \sigma k^2\right)^{-1}}{\sum_k \left(\kappa k^4 + \sigma k^2\right)^{-1}} \tag{8.55}$$

where the decay frequency is

$$\omega_k = \frac{\kappa k^4 + \sigma k^2}{4\eta k} \tag{8.56}$$

The equal-time correlation in position can be written as [100]:

$$\frac{\langle z(\mathbf{r})z(\mathbf{r}')\rangle}{\langle z^2\rangle} = \frac{\sum_k \cos\left[\mathbf{k}\cdot(\mathbf{r}-\mathbf{r}')\right]\left(\kappa k^4 + \sigma k^2\right)^{-1}}{\sum_k \left(\kappa k^4 + \sigma k^2\right)^{-1}} \tag{8.57}$$

We compare our simulation results against the normalized height-height autocorrelation (Eq. 8.55) and equal-time position correlation (Eq. 8.57) in Fig. 8.4. As we see, the simulation results follow analytical curve closely but in a fluctuating manner. If we look at the derivation of analytical results, we realize that in (continuous) Fourier space, each mode dynamics is given as

$$\frac{dz_k}{dt} = -\left(\frac{\kappa k^4 + \sigma k^2}{4\eta k}\right) z_k + \Lambda_k \zeta_k \tag{8.58}$$

We can derive its autocorrelation in a manner analogous to "derivation of noise term". Note that (continuous) Fourier transform of biharmonic (and other derivatives, as well) is k^4, however, discrete

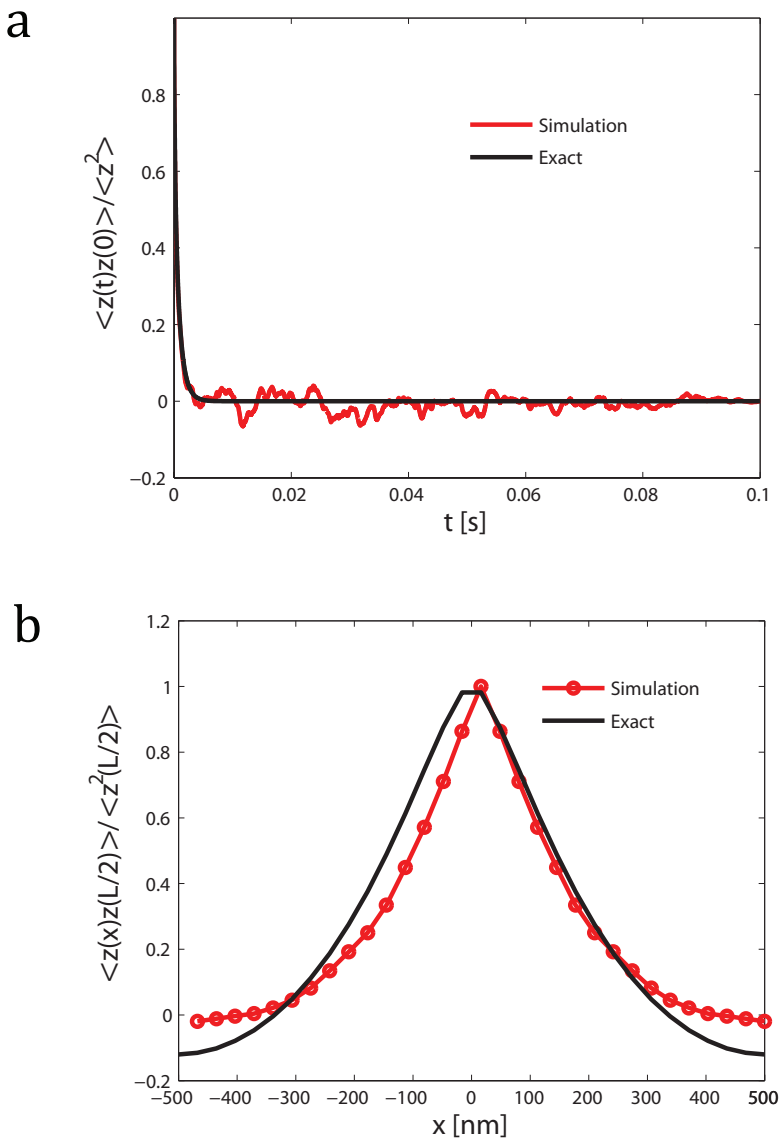

Figure 8.4: (a) Normalized time correlation averaged over all the grid-points of the membrane. (b) Normalized position correlation averaged over a time-period of 0.1 s. The results are plotted for a $1 \times 1 \mu m^2$ membrane patch with κ=5 k_BT, σ=3 μN/m and surrounding fluid viscosity, η=0.06 poise corresponding to cytoplasmic viscosity. The membrane is discretized with 70 grid-points along its length.

Fourier transform of *discretized biharmonic* is not necessarily just k^4. So, while above derivation for height-heigth autocorrelation is exact for continuous biharmonic, it is not necessarily exact for our discrete version. So, we do not expect the results to match exactly. The fluctuations in our

correlation must be due to some imaginary frequencies since real frequencies always decay without oscillations.

8.3 Extension: Three Dimensional Structure of Endocytic Proteins

8.3.1 Block Model of Proteins

In this work, we have employed a very minimal model for the proteins: proteins like epsin are represented as hard-spheres while clathrin is represented solely by its curvature function. Direct incorporation of three-dimensional detailed atomic structure of the endocytic proteins in our work will be cumbersome and computationally expensive. Instead we speculate that the following procedure might be more viable. We introduce a "block-model" for proteins that epitomizes protein shape, effective charge distribution, non-specific attraction, and specific interaction through recognition motifs, all at a coarse-grained level (see Fig. 8.5). The three-dimensional space is discretized

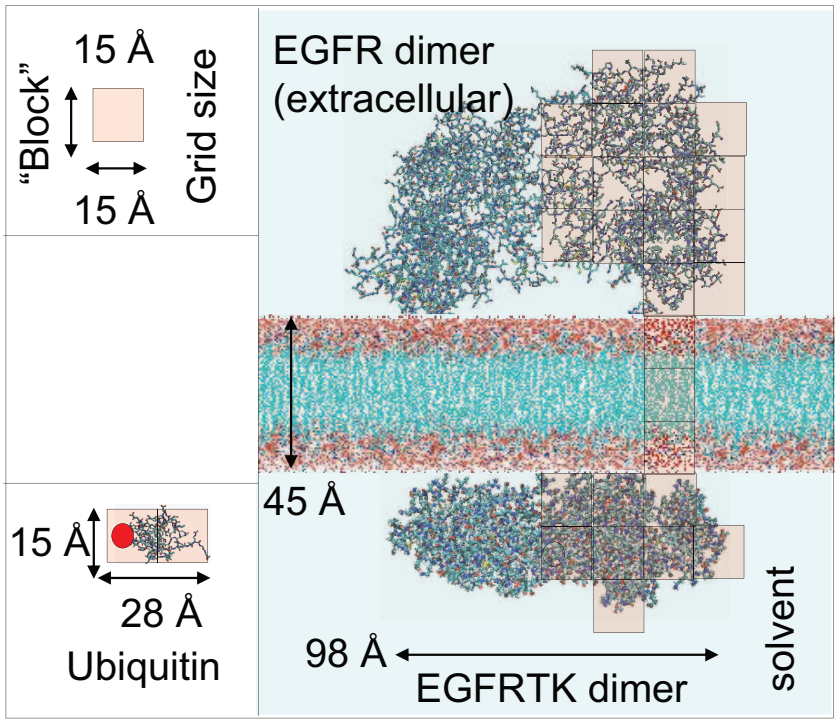

Figure 8.5: Coarse-grained protein model.

into a lattice using a rectilinear grid with grid-size $a_0 = 1.5$ nm, chosen to be equal to the size

of ubiquitin. Each grid unit, i.e. a $1.5 \times 1.5 \times 1.5$ nm^3 cube is considered a "block". Each protein is represented as a combination of rigid blocks, and the blocks themselves are not allowed to overlap with one-another. The fully atomistic model for each protein can be obtained from crystallographic data. In case, fully atomistic crystallographic data of full protein is not available, we resort to homology modeling to build a model for the missing parts of the protein. To construct the block-model for each protein, the blocks are stacked on each other and then super-imposed on the atomic model of the protein. Blocks that have less than 20% atomic occupancy by volume are deleted and the rest retained to form the coarse-grained spatial model. Furthermore, more details can be included in this block-model of proteins by including non-specific interactions like electrostatic and van der Waals interactions through proper assignment of net charges and net Lennard-Jones parameters to each block. Specific intermolecular interactions between domains of different proteins can also be handled via this model. If a protein-block houses a protein fragment with specific binding site recognizing a partner protein (such as a dimer of EGFR), the block is represented by a red dot. Blocks with red dots, in addition to Coulombic and dispersion terms, are represented by an effective interaction energy term equal to the free energy ΔG of binding to the partner. To recognize the specific nature of such interactions, these terms are non-zero only if two red-dots of complementary proteins fall on the common face of adjacent blocks. The $\Delta G = k_B T \ln K_M$ of such interactions is calculated from the corresponding equilibrium constant K_M available from literature [51, 52, 97, 136]; we note that K_M is the dissociation constant with units of M and ΔG is the free energy of association.

8.3.2 Homology Modeling of Proteins

A fully atomistic model depicting the spatial and temporal orientation of the proteins involved in endocytosis would be very helpful in determining a set of rules (e.g. does steric hindrance prevents two proteins to be docked in close proximity at the same time) that govern the geometry of endoctyic complex. Motivated by the map of clathrin cage at 2.1 nm [163] resolution, we speculate that addition of further details to this coarse map of clathrin-AP-2 cage would be a fruitful exercise. However, a quick overview of the crystallographic database (RCSB database) indicates that full atomistic models of key proteins involved in endocytosis like EGFR dimer, AP-2, Clathrin and Epsin are missing. Full-length protein models of the endocytic proteins and their assemblies can offer a valuable insight into the spatial organization of these proteins. A block model of the protein (see section 8.3.1) can also be constructed based on full-length models. Homology modeling is a powerful tool to predict protein structures (target) based on amino acid sequence identity to a protein of known structure (template). While the construction of accurate protein models is

valuable, the first step is to assemble a low resolution complex of proteins, and visualize how they are spatially arranged and may interact. By visualizing the clathrin-mediated endocytic complex, viewers can discern the spatial interaction of their domains. In the following paragraph, we provide a summary of the general method that can be followed to construct a homology model of a protein.

Amino acid sequence information and a list of existing structures for a protein are available online provided from UniProt (http://www.uniprot.org), a comprehensive online resource of protein information. The atomistic (X-ray or nmr) crystal structure of the protein can be downloaded from the RCSB databank (http://www.rcsb.org), which hosts an archive of 3D protein structures. If the full-length atomistic structure of the protein is not available, then process of template selection, alignment and model building can be done using SWISS-MODEL [156]. SWISS-MODEL (http://swissmodel.expasy.org) is an online server for automated comparative modeling of three-dimensional protein structures. In some cases, an immediate homolog of the protein is not available. In such cases, PSIPRED [80] (http://bioinf.cs.ucl.ac.uk/psipred/) can be used to identify more distant homologs. If target sequence has inserted residues relative to the template structure or have regions that are structurally different from the corresponding regions in the template, then structural information about these regions (termed as loops) cannot be extracted from the template structure. ModLoop [50] (http://modbase.compbio.ucsf.edu/modloop/modloop.html) can be used to model such loops. This method is limited to 20 residues, and is generally not advisable for more than 14 residues since the accuracy of the conformation declines with the number of residues. ModLoop uses algorithms from MODELLER which rely on the satisfaction of spatial constraints, and does not use a template protein. Protein visualization and editing program DeepView [66] (http://spdbv.vital-it.ch/) which interfaces with Swiss-Model is used to visulize and refine the protein structure obtained from homology modeling. Refinements in the structure like changing bond angles of residues, rotating fragments of the entire protein can be easily performed with DeepView. It also displays Ramachandran Plots, allowing the user to move points on the plot to actually change the dihedral angles of the residue in the workspace. In the following section, we follow the above-mentioned procedure to construct a homology model of AP-2 protein.

AP-2 Model

AP-2 is a hetero-tetrameric protein composed of four subunits: α, $\beta 2$, $\mu 2$ and $\sigma 2$. Each of the two large (approx. 100 kDa) α and $\beta 2$ subunits consists of a N-terminal domain (trunk) and a globular C-terminal domain (appendage), which are connected by a flexible linker. It has two binding sites for PtdIns(4,5)P_2 - one triplet lysine cluster located on N-terminal region of α subunit and another on $\mu 2$ subunit [76] which interact independently with phosphoinositides. $\mu 2$ subunit also harbors a

binding site for Yxxϕ motif present on the cargo. Specifically, μ2 subunit interacts with FYRALM motif on EGFR where the Y974 is located close to the C-terminal tail of EGFR (the homologous motif on ErbB2 is FY_{1005}RSLL while both ErbB3 and ErbB4 lack this motif). However, bindig of μ2 domain to the phosphoinositide and Yxxϕ motif requires phosphorylation of μ2Thr156 by AAK1. Presumably, the phosphorylation of μ2Thr156 leads to a conformational change leading to increases accessibility of μ2 for binding to phosphoinositide and the cargo. AP2 also interacts with clathrin through the β2 hinge and appendage domains [130] while the α appendage interacts with epsin [22].

A crystal structure of the core of AP-2 is available in RCSB database(PDB ID: 2VGL). Crystal structures of both $\alpha-$ (PDB ID: 1B9K) and $\beta2-$ (PDB ID: 1E42) appendages are also available. These X-ray crystallography structures were submitted to SWISS-MODEL to build any missing regions aside from the appendage linker regions. ModLoop was used to fill in the structure of first and last few residues. Linker region of AP-2 connecting the appendages to the core do not share any homology to the available protein stuctures. Since the linkers are >100 residues, loop modeling cannot be used. Hence, we assume that the linker region lack any secondary structure and we generate their (random-chain) structures using CHARMM. The complete AP-2 model (see Fig. 8.6) is then checked for its structural quality based on Ramachandran plot. The largest dimension of AP-2 is $\approx$ 53 nm (based on the distance between the two appendages) while the size of the AP-2 core is $\approx 12 \times 10$ nm^2.

The procedure outlined above can be used, in principle, to generate homology models of phosphorylated μ2Thr156-AP-2 as well. Furthermore, homology models of epsin and EGFR dimer can as well be constructed. However, more experimental data might be required for relative placement of the domains when the domains on the protein are connected by flexible linkers.

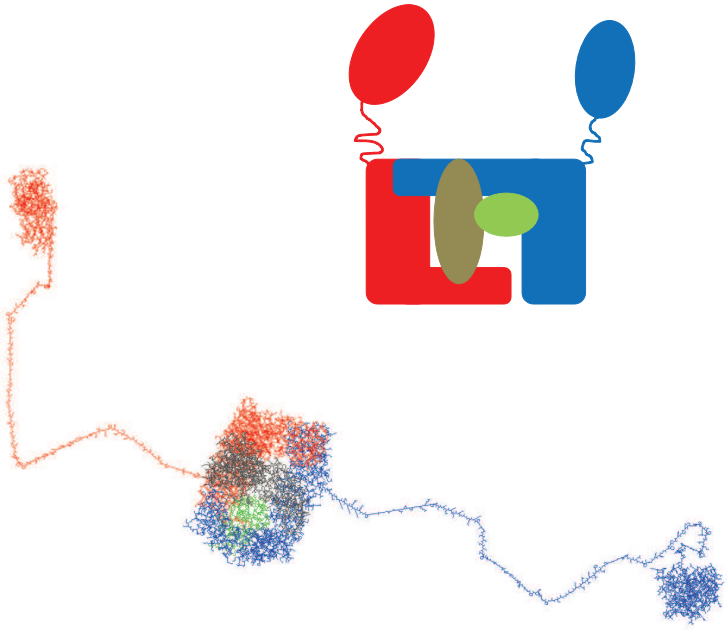

Figure 8.6: Homology model of AP-2. All four domains of AP-2 -α (blue), β2 (red), μ2 (gray) and σ2 (green) - are depicted. The inset shows a schematic of AP-2 adaptor.

Bibliography

[1] U. Agero, L. G. Mesquita, B. R. A. Neves, R. T. Gazzinelli, and O. N. Mesquita. Defocusing microscopy. *Microsc. Res. Tech.*, 65(3):159–165, 2004.

[2] U. Agero, C. H. Monken, C. Ropert, R. T. Gazzinelli, and O. N. Mesquita. Cell surface fluctuations studied with defocusing microscopy. *Phys. Rev. E*, 67(5):051904, 2003.

[3] N. J. Agrawal and R. Radhakrishnan. Role of glycocalyx in mediating nanocarrier cell adhesion explored using a thermodynamic model and monte carlo simulations. *J. Phys. Chem. C*, 111:15848–15856, 2007.

[4] N. J. Agrawal and R. Radhakrishnan. Calculation of free energies in fluid membranes subject to heterogeneous curvature fields. *Phys. Rev. E*, 80:11925, 2009.

[5] N. J. Agrawal, R. Radhakrishnan, and P. K. Purohit. Geometry of mediating protein affects the probability of loop formation in dna. *Biophys. J.*, 94(8):3150–3158, 2008.

[6] N. J. Agrawal, J. Weinstein, and R. Radhakrishnan. Landscape of finite-temperature equilibrium behavior of curvature inducing proteins on a bilayer membrane explored using a linearized elastic free energy model. *Mol. Phys.*, 106(15):1913–1923, 2008.

[7] R.C. Aguilar and B. Wendland. Endocytosis of membrane receptors: Two pathways are better than one. *Proc. Natl. Acad. Sci. U.S.A.*, 102(8):2679–2680, 2005.

[8] B. Alberts, Bray D., A. Johnson, J. Lewis, M. Raff, K. Roberts, and P. Walter. *Essential Cell Biology*. Garland Publishing, New York, 2004.

[9] M.P. Allen and D.J. Tildesley. *Computer simulation of liquids*. Oxford science publications, Oxford, 1987.

[10] I. Andricioaei and M. Karplus. On the calculation of entropy from covariance matrices of the atomic fluctuations. *J. Chem. Phys.*, 115(14):6289–6292, 2001.

[11] H. Aranda-Espinoza, A. Berman, N. Dan, P. Pincus, and S. Safran. Interaction between inclusions embedded in membranes. *Biophys. J.*, 71(2):648–656, 1996.

[12] G. B. Arfken. *Mathematical methods for physicists*. Academic Press, Orlando, 1985.

[13] E. Atilgan and S. X. Sun. Shape transitions in lipid membranes and protein mediated vesicle fusion and fission. *J. Chem. Phys.*, 126(9):095102, 2007.

[14] K. G. Bache, T. Slagsvold, and H. Stenmark. Defective downregulation of receptor tyrosine kinases in cancer. *Embo J.*, 23(14):2707–2712, 2004.

[15] T. Baumgart, Das S., Webb W. W., and Jenkins J. T. Membrane elasticity in giant vesicles with fluid phase coexistence. *Biophys. J.*, 89(2):1067–1080, 2005.

[16] T. Baumgart, Hess S. T., and Webb W. W. Imaging coexisting fluid domains in biomembrane models coupling curvature and line tension. *Nature*, 425(6960):821–824, 2003.

[17] G. I. Bell. Models for specific adhesion of cells to cells. *Science*, 200(4342):618–627, 1978.

[18] G. I. Bell, M. Dembo, and P. Bongrand. Cell adhesion. competition between nonspecific repulsion and specific bonding. *Biophys. J.*, 45(6):1051–1064, 1984.

[19] S. K. Bhatia, M. R. King, and D. A . Hammer. The state diagram for cell adhesion mediated by two receptors. *Biophys. J.*, 84:2671, 2003.

[20] P. D. Blood and G. A. Voth. Direct observation of bin/amphiphysin/rvs (bar) domain-induced membrane curvature by means of molecular dynamics simulations. *Proc. Natl. Acad. Sci. U.S.A.*, 103(41):15068–15072, 2006.

[21] D. H. Boal. *Mechanics of the cell*. Cambridge University Press, Cambridge, 2002.

[22] T. J. Brett, L. M. Traub, and D. H. Fremont. Accessory protein recruitment motifs in clathrin-mediated endocytosis. *Structure*, 10(6):797–809, 2002. 0969-2126.

[23] F. Brochard and J. F. Lennon. Frequency spectrum of flicker phenomenon in erythrocytes. *J. Phys.*, 36(11):1035–1047, 1975.

[24] W. Cai and T. C. Lubensky. Hydrodynamics and dynamic fluctuations of fluid membranes. *Phys. Rev. E*, 52(4):4251, 1995.

[25] M. D. Carmo. *Differential geometry of curves and surfaces*. Englewood Cliffs, 1976.

[26] P.M. Chaikin and T.C. Lubensky. *Principles of condensed matter physics*. Cambridge university press, 2000.

[27] J. A. Champion, Y. K. Katare, and S. Mitragotri. Particle shape: A new design parameter for micro- and nanoscale drug delivery carriers. *J. Controlled Release*, 121(1-2):3–9, 2007.

[28] B. Chen and B. M. M. Fu. An electrodiffusion-filtration model for effects of endothelial surface glycocalyx on microvessel permeability to macromolecules. *J. Biomech. Eng.-Trans. ASME*, 126(5):614–624, 2004.

[29] M. Chinkers, J.A. McKanna, and S. Cohen. Rapid induction of morphological changes in human carcinoma cells a-431 by epidermal growth factor. *J. Cell. Biol.*, 83:260–265, 1979.

[30] T. Chou, K. S. Kim, and G. Oster. Statistical thermodynamics of membrane bending-mediated protein-protein attractions. *Biophys. J.*, 80(3):1075–1087, 2001.

[31] T. E. Cloutier and J. Widom. Spontaneous sharp bending of double-stranded dna. *Mol. Cell*, 14(3):355–362, 2004.

[32] L. Czapla, D. Swigon, and W. K. Olson. Sequence-dependent effects in the cyclization of short dna. *J. Chem. Theory Comput.*, 2(3):685–695, 2006.

[33] N. Dan, A. Derman, P. Pincus, and S. SAfran. Membrane-induced interactions between inclusions. *J. Phys. II*, 4(10):1713–1725, 1994.

[34] W. K. den Otter and S. A. Shkulipa. Intermonolayer friction and surface shear viscosity of lipid bilayer membranes. *Biophys. J.*, 93(2):423–433, 2007.

[35] M. Deserno. Elastic deformation of a fluid membrane upon colloid binding. *Phys. Rev. E*, 69(3):031903, 2004.

[36] I. Dikic. Mechanisms controlling egf receptor endocytosis and degradation. *Biochem. Soc. Trans.*, 31(6):1178, 2003.

[37] F. Divet, G. Danker, and C. Misbah. Fluctuations and instability of a biological membrane induced by interaction with macromolecules. *Phys. Rev. E*, 72(4):041901, 2005.

[38] M. Doi and S. F. Edwards. *The theory of polymer dynamics*. Clarendon Press, Oxford, 1988.

[39] N. Douarche and S. Cocco. Protein-mediated dna loops: Effects of protein bridge size and kinks. *Phys. Rev. E*, 72:061902, 2005.

[40] Q. Du, C. Smith, N. Shiffeldrim, M. Vologodskaia, and Vologodskii. A. Cyclization of short dna fragments and bending fluctuations of the double helix. *Proc. Natl. Acad. Sci. USA*, 102(15):5397–5402, 2005.

[41] D. H. Eberly and K. Shoemake. *Game Physics*. Morgan Kaufmann, San Francisco, 2003.

[42] M. A. Edeling, C. Smith, and D. Owen. Life of a clathrin coat: insights from clathrin and ap structures. *Nat Rev Mol Cell Biol*, 7(1):32–44, 2006.

[43] M. Ehrlich, W. Boll, A. van Oijen, R. Hariharan, K. Chandran, M. L. Nibert, and T. Kirchhausen. Endocytosis by random initiation and stabilization of clathrin-coated pits. *Cell*, 118(5):591–605, 2004.

[44] A.O. Eniola, E.F. Krasik, L.A. Smith, G. Song, and D.A. Hammer. I-domain of lymphocyte function-associated antigen-1 mediates rolling of polystyrene particles on icam-1 under flow. *Biophys. J.*, 89(5):3577–3588, 2005.

[45] R.J. Epstein. *Human Molecular Biology: An Introduction to the Molecular Basis of Health and Disease.* Cambridge University Press, Cambridge, 2003.

[46] E. Evans and K. Ritchie. Dynamic strength of molecular adhesion bonds. *Biophys. J.*, 72(4):1541–55, 1997.

[47] B. Fain, J. Rudnick, and S. Ostlund. Conformations of linear dna. *Phys. Rev. E*, 55(6):7364–7368, 1997.

[48] K. Farsad and P. De Camilli. Mechanisms of membrane deformation. *Curr. Opin. Cell Biol.*, 15(4):372–381, 2003.

[49] L. Finzi and J. Gelles. Measurement of lactose repressor-mediated loop formation and breakdown in single dna-molecules. *Science*, 267(5196):378–380, 1995.

[50] A. Fiser, R. K. Do, and A. Sali. Modeling of loops in protein structures. *Protein Sci.*, 9(9):1753–1773, 2000.

[51] M. G. J. Ford, I. G. Mills, Y. Vallis, G. J. K. Praefcke, P. R. Evans, and H. T. McMahon. Curvature of clathrin coated pits driven by epsin. *Nature*, 419:361–366, 2002.

[52] M. G. J. Ford, B. M. F. Pearse, M. K. Higgins, Y. Vallis, D. J. Owen, A. Gibson, C. R. Hopkins, P. R. Evans, and H. T. McMahon. Simultaneous binding of ptdins(4,5)p2 and clathrin by ap180 in the nucleation of clathrin lattices on membranes. *Science*, 291(5506):1051–1055, 2001.

[53] K. K. Frederick, M. S. Marlow, K. G. Valentine, and A. J. Wand. Conformational entropy in molecular recognition by proteins. *Nature*, 448(7151):325–330, 2007.

[54] D. Frenkel and B. Smit. *Understanding molecular simulation: from algorithms to applications*. Academic Press, San Diego, 2002.

[55] A. M. Friedman, T. O. Fischmann, and T. A. Steitz. Crystal-structure of lac repressor core tetramer and its implications for dna looping. *Science*, 268(5218):1721–1727, 1995.

[56] H. Gao, W. Shi, and L. B. Freund. Mechanics of receptor-mediated endocytosis. *Proc. Natl. Acad. Sci. U.S.A.*, 102(27):9469–9474, 2005.

[57] H. G. Garcia, P. Grayson, L. Han, M. Inamdar, J. Kondev, P. C. Nelson, R. Phillips, J. Widom, and P. A. Wiggins. Biological consequences of tightly bent dna: The other life of a macromolecular celebrity. *Biopolymers*, 85:115–130, 2007.

[58] G. J. Gemmen, R. Millin, and D. E. Smith. Dna looping by two-site restriction endonucleases: heterogeneous probability distributions for loop size and unbinding force. *Nucleic Acids Res.*, 34(10).

[59] Y. Geng, P. Dalhaimer, S. Cai, R. Tsai, M. Tewari, T. Minko, and D. E. Discher. Shape effects of filaments versus spherical particles in flow and drug delivery. *Nat. Nanotechnol.*, 2(4):249–255, 2007.

[60] D. T. Gillespie. A general method for numerically simulating the stochastic time evolution of coupled chemical reactions. *J. Comput. Phys.*, 22:403–434, 1976.

[61] N. Gov. Membrane undulations driven by force fluctuations of active proteins. *Phys. Rev. Lett.*, 93(26):268104, 2004.

[62] N. Gov. Diffusion in curved fluid membranes. *Phys. Rev. E*, 73(4):041918, 2006.

[63] W. T. Gozdz and G. Gompper. Shape transformations of two-component membranes under weak tension. *Europhys. Lett.*, 55(4):587–593, 2001.

[64] A. Grafmuller, J. Shillcock, and R. Lipowsky. Pathway of membrane fusion with two tension dependent energy barriers. *Phys. Rev. Lett.*, 98:218107, 2007.

[65] J. T. Groves. Bending mechanics and molecular organization in biological membranes. *Ann. Rev. Phys. Chem.*, 58(1):697–717, 2007.

[66] N. Guex and M. C. Peitsch. Swiss-model and the swiss-pdbviewer: An environment for comparative protein modeling. *Electrophoresis*, 18:2714–2723, 1997.

[67] J.D. Haley and W.J. Gullick. *EGFR signaling networks in cancer therapy.* Humana Press, New York, 2008.

[68] S.E. Halford, A. J. Welsh, and M.D. Szczelkun. Enzyme-mediated dna looping. *Annu. Rev. Biophys. Biomolec. Struct.*, 33:1–24, 2004.

[69] D. A. Hammer and S. A. Apte. Simulation of cell rolling and adhesion on surfaces in shear flow: General results and analysis of selectin-mediated neutrophil adhesion. *Biophys. J.*, 63:35, 1992.

[70] W. Hanley, O. McCarty, S. Jadhav, Y. Tseng, D. Wirtz, and K. Konstantopoulos. Single molecule characterization of p-selectin/ligand binding. *J. Biol. Chem.*, 278(12):10556–10561, 2003.

[71] T. Harmer, M. Wu, and R. Schleif. The role of rigidity in dna looping-unlooping by arac. *Proc. Natl. Acad. Sci. USA*, 98(2):427–431, 2001.

[72] W. Helfrich. Elastic properties of lipid bilayers - theory and possible experiments. *Z. Naturforsch. C*, 28(11-1):693–703, 1973.

[73] L. Hinrichsen, J. Harborth, L. Andrees, K. Weber, and E. J. Ungewickell. Effect of clathrin heavy chain- and alpha-adaptin-specific small inhibitory rnas on endocytic accessory proteins and receptor trafficking in hela cells. *J. Biol. Chem.*, 278(46):45160–45170, 2003.

[74] L. Hinrichsen, A. Meyerhoiz, S. Groos, and E. J. Ungewickell. Bending a membrane: How clathrin affects budding. *Proc. Natl. Acad. Sci. U.S.A.*, 103(23):8715–8720, 2006.

[75] J. D. Hoffman. *Numerical methods for engineers and scientists.* McGraw-Hill, New York, 1992.

[76] S. Honing, D. Ricotta, M. Krauss, K. Spate, B. Spolaore, A. Motley, M. Robinson, C. Robinson, V. Haucke, and D. J. Owen. Phosphatidylinositol-(4,5)-bisphosphate regulates sorting signal recognition by the clathrin-associated adaptor complex ap2. *Mol. Cell*, 18(5):519–531, 2005.

[77] H. Jacobson and W. H. Stockmayer. Intramolecular reaction in polycondensations .1. the theory of linear systems. *J. of Chem. Phys.*, 18:1600–1606, 1950.

[78] K. Jacobson, A. Ishihara, and R. Inman. Lateral diffusion of proteins in membranes. *Annu. Rev. Physiol.*, 49:163–175, 1987.

[79] J. Jakobsson, H. Gad, F. Andersson, P. Low, O. Shupliakov, and L. Brodin. Role of epsin 1 in synaptic vesicle endocytosis. *Proc. Natl. Acad. Sci. U.S.A.*, 105(17):6445–6450, 2008.

[80] D. H. Jones, A. C. Rigby, K. R. Barber, and C. W. Grant. Protein secondary structure prediction based on position-specific scoring matrices. *J. Mol. Biol.*, 292:195–202, 1999.

[81] M. Kaksonen, C. P. Toret, and D. G. Drubin. Harnessing actin dynamics for clathrin-mediated endocytosis. *Nat Rev Mol Cell Biol*, 7(6):404–414, 2006.

[82] R. S. Kane. Polyvalency: Recent developments and new opportunities for chemical engineers. *AIChE J.*, 52(11):3638–3644, 2006.

[83] J. H. Keen. Clathrin assembly proteins: affinity purification and a model for coat assembly. *J. Cell Biol.*, 105(5):1989–1998, 1987.

[84] A. Khademhosseini and R. Langer. Nanobiotechnology drug deliery and tissue engineering drug delivery and tissue engineering. *Chem. Eng. Prog.*, 102:38, 2006.

[85] K. S. Kim, J. Neu, and G. Oster. Curvature-mediated interactions between membrane proteins. *Biophys J*, 75(5):2274–2291, 1998.

[86] J. T. Kindt. Pivot-coupled grand canonical monte carlo method for ring simulations. *J. Chem. Phys.*, 116:6817–6825, 2002.

[87] T. Kirchhausen. Three ways to make a vesicle. *Nat Rev Mol Cell Biol*, 1(3):187–198, 2000.

[88] T. Kirchhausen, D. E. Staunton, and T. A. Springer. Location of the domains of icam-1 by immunolabeling and single-molecule electron-microscopy. *J. Leukocyte Biol.*, 53(3):342–346, 1993.

[89] K. Klenin, H. Merlitz, and J. Langowski. A brownian dynamics program for the simulation of linear and circular dna and other wormlike chain polyelectrolytes. *Biophys. J.*, 74(2):780–788, 1998.

[90] M. M. Kozlov. Biophysics: Bending over to attract. *Nature*, 447(7143):387–389, 2007.

[91] I. M. Kulic, H. Mohrbach, V. Lobaskin, R. Thaokar, and H. Schiessel. Apparent persistence length renormalization of bent dna. *Phys. Rev. E*, 72(4):041905, 2005.

[92] S.V. Kuznetsov, Y.Q. Shen, A.S. Benight, and A. Ansari. A semiflexible polymer model applied to loop formation in dna hairpins. *Biophys. J.*, 81(5):2864–2875, 2001.

[93] F. Lankas, R. Lavery, and J. H. Maddocks. Kinking occurs during molecular dynamics simulations of small dna minicircles. *Structure*, 14:1527–1534, 2006.

[94] C. L. Lin Lawrence and L. H. Brown Frank. Brownian dynamics in fourier space: Membrane simulations over long length and time scales. *Phys. Rev. Lett.*, 93(25):256001, 2004.

[95] M. Lawrenz, R. Baron, and A. J. McCammon. Independent-trajectories thermodynamic-integration free-energy changes for biomolecular systems: Determinants of h5n1 avian influenza virus neuraminidase inhibition by peramivir. *J. Chem. Theory Comput.*, 5(4):1106–1116, 2009.

[96] S.-J. E. Lee, Y. Hori, J. T. Groves, M. L. Dustin, and A. K. Chakraborty. The synapse assembly model. *Trends Immunol.*, 23(10):500–502, 2002.

[97] M. A. Lemmon, Z. Bu, J. E. Ladbury, M. Zhou, D. Pinchasi, I. Lax, D. M. Engelman, and J. Schlessinger. Two egf molecules contribute additively to stabilization of the egfr dimer. *Embo J*, 16(2):281–94, 1997.

[98] E. M. Lennon, K. Katsov, and G. H. Fredrickson. Free energy evaluation in field-theoretic polymer simulations. *Phys Rev Lett*, 101(13):138302, 2008.

[99] G. Lia, D. Bensimon, V. Croquette, J.-F. Allemand, D. Dunlap, D.E.A. Lewis, S. Adhya, and Finzi. L. Supercoiling and denaturation in gal repressor/heat unstable nucleoid protein (hu)-mediated dna looping. *Proc. Natl. Acad. Sci. USA*, 100(20):11373–11377, 2003.

[100] L. C. L. Lin and F. L. H. Brown. Dynamic simulations of membranes with cytoskeletal interactions. *Phys. Rev. E*, 72(1):011910–15, 2005.

[101] L. C. L. Lin and F. L. H. Brown. Simulating membrane dynamics in nonhomogeneous hydrodynamic environments. *J. Chem. Theory Comput.*, 2(3):472–483, 2006.

[102] J. Liu, M. Kaksonen, D. G. Drubin, and G. Oster. Kinetic monte carlo simulation of deposition of energetic copper atoms on a cu(001) substrate. *J. Phys. D: Appl Phys.*, 38:4202–4209, 2005.

[103] Z.-L. Liu, K.-L. Yao, X.-B. Jing, X.-A. Li, and X.-Z. Sun. Endocytic vesicle scission by lipid phase boundary forces. *Proc. Natl. Acad. Sci. U.S.A.*, 103(27):10277–10282, 2006.

[104] E. B. Lomakina and R. E. Waugh. Micromechanical tests of adhesion dynamics between neutrophils and immobilized icam-1. *Biophys. J.*, 86(2):1223–1233, 2004.

[105] D. Marguet, P. F. Lenne, H. Rigneault, and H. T. He. Dynamics in the plasma membrane: how to combine fluidity and order. *Embo J.*, 25(15):3446–3457, 2006.

[106] F. Marinelli, F. Pietrucci, A. Laio, and S. Piana. A kinetic model of trp-cage folding from multiple biased molecular dynamics simulations. *PLoS Comput. Biol.*, 5(8):1, 2009.

[107] J. F. Marko and E. D. Siggia. Stretching dna. *Macromolecules*, 28:8759–8770, 1995.

[108] S. J. Marrink, A. H. deVries, and A. E. Mark. Coarse grained model for semiquantitative lipid simulations. *J. Phys. Chem. B*, 108(2):750–760, 2004.

[109] S. J. Marrink and A. E. Mark. Effect of undulations on surface tension in simulated bilayers. *J. Phys. Chem. B*, 105(26):6122–6127, 2001.

[110] S. Mayor and Richard E. Pagano. Pathways of clathrin-independent endocytosis. *Nat Rev Mol Cell Biol*, 8(8):603–612, 2007.

[111] H. T. McMahon and J. L. Gallop. Membrane curvature and mechanisms of dynamic cell membrane remodelling. *Nature*, 438(7068):590–596, 2005.

[112] R. A. Mehta and J. D. Kahn. Designed hyperstable lac repressor center dot dna loop topologies suggest alternative loop geometries. *J. Mol. Biol.*, 294(1):67–77, 1999.

[113] H. Merlitz, K. Rippe, K. V. Klenin, and J. Langowski. Looping dynamics of linear dna molecules and the effect of dna curvature: A study by brownian dynamics simulation. *Biophys. J.*, 74(2).

[114] C. J. Merrifield, D. Perrais, and D. Zenisek. Coupling between clathrin-coated-pit invagination, cortactin recruitment, and membrane scission observed in live cells. *Cell*, 121(4):593–606, 2005.

[115] A. Motley, N. A. Bright, M. N. J. Seaman, and M. S. Robinson. Clathrin-mediated endocytosis in ap-2-depleted cells. *J Cell Biol*, 162:909–918, 2003.

[116] A. W. Mulivor and H. H. Lipowsky. Role of glycocalyx in leukocyte-endothelial cell adhesion. *Am. J. Physiol. Heart Circ. Physiol.*, 283(4):H1282–1291, 2002.

[117] S. Muro, T. Dziubla, W. Qiu, J. Leferovich, X. Cui, E. Berk, and V. R. Muzykantov. Endothelial targeting of high-affinity multivalent polymer nanocarriers directed to intercellular adhesion molecule 1. *J. Pharmacol. Exp. Ther.*, 317(3):1161–1169, 2006.

[118] S. Muro and V. R. Muzykantov. Targeting of antioxidant and anti-thrombotic drugs to endothelial cell adhesion molecules. *Curr. Pharm. Des.*, 11(18):2383–401, 2005.

[119] S. Muro, R. Wiewrodt, A. Thomas, L. Koniaris, S. M. Albelda, V. R. Muzykantov, and M. Koval. A novel endocytic pathway induced by clustering endothelial icam-1 or pecam-1. *J. Cell Sci.*, 116(8):1599–1609, 2003.

[120] M.C. Murphy, I Rasnik, W. Cheng, T.M. Lohman, and T.J. Ha. Probing single-stranded dna conformational flexibility using fluorescence spectroscopy. *Biophys. J.*, 86(4):2530–2537, 2004.

[121] A. Naji and F.L.H. Brown. Diffusion on ruffled membrane surfaces. *J. Chem. Phys.*, 126(23):235103–16, 2007.

[122] N. Naumowicz and Z. Figaszewski. Impedence analysis of phosphatidylcholine/alpha-tocopherol system in bilayer lipid membranes. *J. Membr. Biol.*, 205(1):29–36, 2005.

[123] N. Naumowicz, J. Kotynska, A. Petelska, and Z. Figaszewski. Impedence analysis of phosphatidylcholine membrane modified with valinomycin. *Euro. Biophys. J.*, 35(3):239–246, 2006.

[124] D. R. Nelson and B. I. Halperin. Dislocation-mediated melting in two dimensions. *Phys Rev B*, 19(5):2457, 1979.

[125] D. R. Nelson, T. Piran, and S. Weinberg. *Statistical mechanics of membranes and surfaces.* World Scientific Pub., River Edge, N.J., 2nd edition, 2004.

[126] J. C. Neto, U. Agero, R. T. Gazzinelli, and O. N. Mesquita. Measuring optical and mechanical properties of a living cell with defocusing microscopy. *Biophys. J.*, 91(3):1108–1115, 2006.

[127] R. Nossal. Energetics of clathrin basket assembly. *Traffic*, 2(2):138–147, 2001.

[128] V. Ortiz, S. O. Nielsen, M. L. Klein, and D. E. Discher. Computer simulation of aqueous block copolymer assemblier: Length scales and methods. *J. Poly. Sci. B: Poly. Phys.*, 44(14):1907–1918, 2006.

[129] S. Oved and Y. Yarden. Molecular ticket to enter cells. *Nature*, 416:133–136, 2002.

[130] D. J. Owen, Y. Vallis, B. M. Pearse, H. T. McMahon, and P. R. Evans. The structure and function of the beta 2-adaptin appendage domain. *Embo J*, 19(16):4216–27, 2000.

[131] R. K. Pathria. *Statistical Mechanics.* Butterworth Heinemann, Oxford, 1996.

[132] T. T. Perkins, S. R. Quake, D. E. Smith, and S. Chu. Relaxation of a single dna molecule observed by optical microscopy. *Science*, 264:822–826, 1994.

[133] A. Pierres, A. Benoliel, and P. Bongrand. *Cell-cell interaction*. Physical chemistry of biological interfaces. Marcel Dekker, New York, 2000.

[134] H. A. Pinnow and W. Helfrich. Effect of thermal undulations on the bending elasticity and spontaneous curvature of fluid membranes. *Eur. Phys. J. E*, 3(2):149–157, 2000.

[135] S. Polo, S. Pece, and P.P. Di Fiore. Endocytosis and cancer. *Curr. Opin. Cell Biol.*, 16(2):156–161, 2004.

[136] G. J. Praefcke, M. G. Ford, E. M. Schmid, L. E. Olesen, J. L. Gallop, S. Y. Peak-Chew, Y. Vallis, M. M. Babu, I. G. Mills, and H. T. McMahon. Evolving nature of the ap2 alpha-appendage hub during clathrin-coated vesicle endocytosis. *Embo J*, 23(22):4371–83, 2004.

[137] P. K. Purohit and P. C. Nelson. Effect of supercoiling on formation of protein-mediated dna loops. *Phys. Rev.*, 74(6):061906, 2006.

[138] S. Y. Qi, Jay T. Groves, and Arup K. Chakraborty. Synaptic pattern formation during cellular recognition. *Proc. Natl. Acad. Sci. U.S.A.*, 98(12):6548–6553, 2001.

[139] R. Radhakrishnan, K. E. Gubbins, and M. Sliwinska-Bartkowiak. Existence of a hexatic phase in porous media. *Phys. Rev. Lett.*, 89(7):076101, 2002.

[140] F. Reif. *Fundamentals of statistical and thermal physics.* McGraw-Hill, Singapore, 1965.

[141] E. Reister-Gottfried, S. M. Leitenberger, and Udo Seifert. Hybrid simulations of lateral diffusion in fluctuating membranes. *Phys. Rev. E*, 75(1):011908–11, 2007.

[142] M. Reuter, D. Kupper, A. Meisel, C. Schroeder, and D. H. Kruger. Cooperative binding properties of restriction endonuclease ecorii with dna recognition sites. *J. Biol. Chem.*, 273:8294–8300, 1998.

[143] B. J. Reynwar, G. Illya, V. A. Harmandaris, M. M. Muller, K. Kremer, and M. Deserno. Aggregation and vesiculation of membrane proteins by curvature-mediated interactions. *Nature*, 447(7143):461–464, 2007.

[144] W. F. Riley, L. D. Sturges, and D. H. Morris. *Statics and mechanics of materials : an integrated approach*. John Wiley and Sons, New York, 1995.

[145] K. Rippe. Making contacts on a nucleic acid polymer. *Trends Biochem. Sci*, 26(12):733–740, 2001.

[146] P. Robert, L. Limozine, A. M. Benoliel, A. Pierres, and P. Bongrand, editors. *Glycocalyx regulation of cell adhesion*. Principles of cellular engineering: understanding the biomolecular interface. Elsevier Academic Press, Amsterdam, 2006.

[147] S. A Safran. *Statistical thermodynamics of surfaces, interfaces, and membranes*. Addison-Wesley Publishing, Reading, 1994.

[148] S. A. Safran. Curvature elasticity of thin films. *Adv. Phys.*, 48:395–448, 1999.

[149] H. S. Sakhalkar, M. K. Dalal, A. K. Salem, R. Ansari, A. Fu, M. F. Kiani, D. T. Kurjiaka, J. Hanes, K. M. Shakesheff, and D. J. Goetz. Leukocyte-inspired biodegradable particles that selectively and avidly adhere to inflamed endothelium in vitro and in vivo. *Proc. Natl. Acad. Sci. U.S.A.*, 100(26):15895–15900, 2003.

[150] S. Sankararaman and J. F. Marko. Formation of loops in dna under tension. *Phys. Rev. E*, 71(2):021911, 2005.

[151] R. Schleif. Dna looping. *Annu. Rev. Biochem.*, 61:199–223, 1992.

[152] M. Schlierf and M. Rief. Temperature softening of a protein in single-molecule experiments. *J. Mol. Biol.*, 354(2):497–503, 2005.

[153] E.M. Schmid and H.T. McMahon. Integrating molecular and network biology to decode endocytosis. *Nature*, 448(7156):883–888, 2007.

[154] S. L. Schmid. Clathrin-coated vesicle formation and protein sorting. *Ann. Rev. Biochem.*, 66:511–548, 1997.

[155] A. A. Schmidt. The making of a vesicle. *Nature*, 419:347–348, 2002.

[156] T. Schwede, J. Kopp, N. Guex, and M. C. Peitsch. Swiss-model: an automated protein homology-modeling server. *Nucleic Acids Res.*, 31:3381–3385, 2003.

[157] U. Seifert, K. Berndl, and R. Lipowsky. Shape transformations of vesicles: Phase diagram for spontaneous- curvature and bilayer-coupling models. *Phys Rev A*, 44(2):1182, 1991.

[158] U. Seifert and S. A. Langer. Viscous modes of fluid bilayer-membranes. *Europhys. Lett.*, 23(1):71–76, 1993.

[159] J. Shimada and H. Yamakawa. Ring-closure probabilities for twisted wormlike chains - application to dna. *Macromolecules*, 17(4):689–698, 1984.

[160] S. A. Shkulipa, W. K. den Otter, and W. J. Briels. Surface viscosity, diffusion, and intermonolayer friction: Simulating sheared amphiphilic bilayers. *Biophys. J.*, 89(2):823–829, 2005.

[161] S. A. Shkulipa, W. K. den Otter, and W. J. Briels. Simulations of the dynamics of thermal undulations in lipid bilayers in the tensionless state and under stress. *J. Chem. Phys.*, 125(23):234905–11, 2006.

[162] S. Sigismund, T. Woelk, C. Puri, E. Maspero, C. Tacchetti, P. Transidico, P.P. Di Fiore, and S. Polo. Clathrin-independent endocytosis of ubiquitinated cargos. *Proc. Natl. Acad. Sci. U.S.A.*, 102(8):2760–2765, 2005.

[163] C. J. Smith, N. Grigorieff, and B. M. F. Pearse. Clathrin coats at 21 angstrom resolution: a cellular assembly designed to recycle multiple membrane receptors. *Embo J*, 17(17):4943–4953, 1998.

[164] A. Sorkin and M. Von Zastrow. Signal transduction and endocytosis: close encounters of many kinds. *Nat Rev Mol Cell Biol*, 3(8):600–14, 2002.

[165] J. M. Squire, M. Chew, G. Nneji, C. Neal, J. Barry, and C. Michel. Quasi-periodic substructure in the microvessel endothelial glycocalyx: a possible explanation for molecular filtering? *J. Struct. Biol.*, 136(3):239–55, 2001.

[166] P. B. Sunil Kumar, G. Gompper, and R. Lipowsky. Budding dynamics of multicomponent membranes. *Phys. Rev. Lett.*, 86(17):3911–3914, Apr 2001.

[167] B. Sutherland. Some exact results for one-dimensional models of solids. *Phys. Rev. A*, 8(5):2514–2516, 1973.

[168] V. P. Torchilin, A. N. Lukyanov, Z. Gao, and B. Papahadjopoulos-Sternberg. Immunomicelles: Targeted pharmaceutical carriers for poorly soluble drugs. *Proc. Natl. Acad. Sci. U.S.A.*, 100(10):6039–6044, 2003.

[169] B. van den Broek, F. Vanzi, D. Normanno, and G. J. L. Pavone, F. S. Wuite. Real-time observation of dna looping dynamics of type iie restriction enzymes naei and nari. *Nucleic Acids Res.*, 34(1):167–174, 2006.

[170] N.G. van Kampen. *Stochastic processes in physics and chemistry*. North-Holland, Amsterdam, 1992.

[171] A. Veksler and N. S. Gov. Phase transitions of the coupled membrane-cytoskeleton modify cellular shape. *Biophys J*, 93(11):3798–3810, 2007.

[172] A. V. Vologodskii, S. D. Levene, K. V. Klenin, M. Frank-Kamenetskii, and N. R. Cozzarelli. Conformational and thermodynamic properties of supercoiled dna. *J. Mol. Biol.*, 227(4):1224–1243, 1992.

[173] B.D. Vujanovic and T. M. Atanackovic. *An introduction to modern variational techniques in mechanics and engineering*. Springer, 2004.

[174] E. J. Wallace, N. M. Hooper, and P. D. Olmsted. The kinetics of phase separation in asymmetric membranes. *Biophys. J.*, 88(6):4072–4083, 2005.

[175] F. G. Wang and D. P. Landau. Efficient, multiple-range random walk algorithm to calculate the density of states. *Phys. Rev. Lett.*, 86(10):2050–2053, 2001.

[176] L. Wang and Clancy P. Kinetic monte carlo simulation of the growth of polycrystalline cu films. *Surf. Sci.*, 473:25–38, 2001.

[177] T. R. Weikl. Fluctuation-induced aggregation of rigid membrane inclusions. *Europhys. Lett.*, 54.

[178] S. Weinbaum, X. Zhang, Y. Han, H. Vink, and S. C. Cowin. Mechanotransduction and flow across the endothelial glycocalyx. *Proc. Natl. Acad. Sci. U.S.A.*, 100(13):7988–7995, 2003.

[179] J. Weinstein and R. Radhakrishnan. A coarse-grained methodology for simulating interfacial dynamics in complex fluids: application to protein mediated membrane processes. *Mol. Phys.*, 104(22-24):3653–3666, 2006.

[180] P. A. Wiggins, R. Phillips, and P. C. Nelson. Exact theory of kinkable elastic polymers. *Phys. Rev. E*, 71(2):021909, 2005.

[181] H. Yamakawa. *Modern theory of polymer solutions*. Harper and Row, New York, 1971.

[182] T. Yamazaki, K. Zaal, D. Hailey, J. Presley, J. Lippincott-Schwartz, and L.E. Samelson. Role of grb2 in egf-stimulated egfr internalization. *J Cell Sci*, 115(9):1791–1802, 2002.

[183] G. Zeder-Lutz, E. Zuber, J. Witz, and M. H. V. Van Regenmortel. Thermodynamic analysis of antigen-antibody binding using biosensor measurements at different temperatures. *Anal. Biochem.*, 246:123–132, 1997.

[184] C.-Z. Zhang and Z.-G. Wang. Nucleation of membrane adhesions. *Phys Rev E*, 77(2):021906, 2008.

[185] X. Zhang, E. Wojcikiewicz, and V. T. Moy. Force spectroscopy of the leukocyte function-associated antigen-1/intercellular adhesion molecule-1 interaction. *Biophys. J.*, 83(4):2270–2279, 2002.

[186] J. Zimmerberg and M. M. Kozlov. How proteins produce cellular membrane curvature. *Nat Rev Mol Cell Biol*, 7(1):9–19, 2006.

[187] C. Zurla, A. Franzini, G. Galli, D. D. Dunlap, D. E. A. Lewis, S. Adhya, and L. Finzi. Novel tethered particle motion analysis of ci protein-mediated dna looping in the regulation of bacteriophage lambda. *J. Phys.-Condens. Matter*, 18(14):S225–S234, 2006.